

UNIVERSITY OF BELGRADE

SCHOOL OF ELECTRICAL ENGINEERING



TUSHAR SINGH

ACCURACY-CONTROLLED 3D ELECTROMAGNETIC MODELING OF MEDICAL MICROWAVE IMAGING SCENARIOS

-DOCTORAL DISSERTATION-

BELGRADE 2026

УНИВЕРЗИТЕТ У БЕОГРАДУ

ЕЛЕКТРОТЕХНИЧКИ ФАКУЛТЕТ

Тушар Синг

КОНТРОЛИСАНО ТРОДИМЕНЗИОНАЛНО ЕЛЕКТРОМАГНЕТСКО МОДЕЛОВАЊЕ СИСТЕМА ЗА ДОБИЈАЊЕ МИКРОТАЛАСНИХ СЛИКА У МЕДИЦИНИ

ДОКТОРСКА ДИСЕРТАЦИЈА

Београд, 2026

SUPERVISORS

Dr. Marija Stevanović
University of Belgrade – School of Electrical Engineering

Jury Members

Dr. Branko Kolundžija, Full Professor
University of Belgrade – School of Electrical Engineering
(Chair of the Committee)

Dr. Miodrag Tasić, Associate Professor
University of Belgrade – School of Electrical Engineering

Dr. Nebojša Dončov, Full Professor
University of Niš – Faculty of Electronic Engineering
(Committee Member from Outside the School of Electrical Engineering)

Defense date _____

Acknowledgement

I would like to express my sincere gratitude to my supervisor, Prof. Dr. Marija Nikolić Stevanović, for her continuous guidance, encouragement, and dedication throughout my doctoral studies. Her deep understanding of the theoretical foundations of Medical Microwave Imaging and electromagnetic modeling greatly influenced this research. From the initial stages of coursework to the completion of this dissertation, she provided invaluable advice, direction, and support, helping me overcome numerous academic and research challenges.

I am especially thankful to Dr. Branko Kolundžija, who played a pivotal role in my professional and research development during my time at WIPL-D d.o.o. Through his mentorship, he nurtured my understanding of electromagnetic simulations and provided extensive hands-on experience with advanced modeling techniques.

I would also like to thank Mlađen Stevanetić, Jasmin Musić, Ana Djurdjević and Branislav M. Ninković for their support, constructive discussions, and assistance with various technical aspects of this research. Their willingness to share ideas and provide valuable feedback contributed significantly to the successful completion of this dissertation.

I am deeply grateful to my family for their constant love, patience, and encouragement throughout this journey. A special thank you goes to my wife for her unwavering support and understanding during the many years of doctoral study. I would also like to thank my son, whose presence brought joy, motivation, and a renewed sense of purpose, inspiring me to stay focused and successfully complete this important milestone in my life.

Tushar Singh

Title of doctoral dissertation: Accuracy-Controlled 3D Electromagnetic Modeling of Medical Microwave Imaging Scenarios

Abstract: The research presented in this dissertation aimed to develop a methodology for the electromagnetic modeling of microwave systems for medical diagnosis, with particular emphasis on systems for stroke detection. Given the complexity of these systems, their direct modeling would require enormous computational resources and would be practically infeasible. Therefore, the research focused on the systematic simplification of these models while maintaining controlled accuracy of the results.

Microwave measurement systems have significant potential in medical diagnostics because they are non-invasive, portable, cost-effective, and do not use ionizing radiation. However, the reliability of detection depends to a large extent on the quality of the measurement system, as well as on the accuracy of the electromagnetic simulations used to generate the data required for image reconstruction. Therefore, the first step in this dissertation was the design of a helmet-shaped antenna system comprising 21 antenna elements, intended to operate within a narrow frequency range around 1 GHz. The procedure involved the design of individual antenna elements implemented as microstrip antennas and optimized for operation in the presence of the head, followed by the determination of their optimal arrangement, with the aim of accommodating the largest possible number of antennas within the available helmet space. Subsequently, a numerical head model was developed in the form of an anthropomorphic multilayer phantom with a dielectric inclusion representing a brain stroke. The numerical phantom was constructed based on a highly detailed model of the human head obtained from magnetic resonance imaging.

The proposed methodology integrates controlled surface decimation, which minimizes geometric deviation, the generation of a quadrilateral mesh suitable for analysis based on the Method of Moments and higher-order basis functions, and a systematic assessment of result convergence. Self-convergence studies based on *h*-, *p*-, and *hp*-refinement demonstrated that the deviations of the electric field and scattering parameters from the reference values can be reduced to very low levels, confirming the numerical stability and reliability of the forward model. Furthermore, it was shown that the differential quantities used for microwave image reconstruction are significantly less sensitive to geometric simplifications than absolute quantities. Validation based on the residuals of the inverse scattering equation further confirmed the accuracy of the simulation model, while the microwave images remained stable throughout the entire refinement process.

Additionally, a methodology was developed for obtaining an equivalent homogeneous head model using dielectric mixture formulas and optimization techniques. The resulting homogeneous model showed very good agreement with the scattering parameters of the original heterogeneous model, while significantly reducing the simulation time.

Keywords: Antenna array, anthropomorphic head phantom, microwave imaging, method of moments, self-convergence analysis, stroke detection

Scientific Field: Electrical and Computer Engineering

Scientific Sub-Field: Electromagnetics, antennas, and microwaves.

Наслов докторске дисертације: Контролисано тродимензионално електромагнетско моделовање система који се користе за добијање микроталасних слика у медицини

Сажетак: Истраживање представљено у овој дисертацији имало је за циљ развој методологије за електромагнетско моделовање микроталасних система за медицинску дијагностику, са посебним акцентом на системе за детекцију можданог удара. С обзиром на сложеност ових система, њихово директно моделовање захтевало би енормне рачунарске ресурсе и било би практично неизводљиво. Стога је истраживање било усмерено на систематично поједностављење ових модела, уз истовремено очување контролисане тачности резултата.

Микроталасни мерни системи имају велики потенцијал у медицинској дијагностици, јер су неинвазивни, преносиви, ценовно приступачни и не користе јонизујуће зрачење. Међутим, поузданост детекције у великој мери зависи од квалитета мерног система, као и од тачности електромагнетских симулација на основу којих се генеришу подаци потребни за добијање слике. Стога је у овој дисертацији најпре пројектован антенски систем у облику кациге са 21 антенским елементом, намењен за рад у уском фреквенцијском опсегу око 1 GHz. Поступак је обухватио пројектовање појединачних антенских елемената реализованих у техници микрострип антена, оптимизованих за рад у присуству главе, а затим и одређивање њиховог оптималног распореда, са циљем да се у расположивом простору кациге постави што је могуће већи број антена. Потом је развијен нумерички модел главе у облику антропоморфног вишеслојног фантома са диелектричном инклузијом која симулира мождани удар. Нумерички фантом је конструисан полазећи од јако детаљног модела људске главе који је добијен магнетском резонанцом.

Предложена методологија интегрише контролисану децимацију површи, којом се минимизује геометријско одступање, генерисање четвороугаоне мреже погодне за анализу засновану на методи момената и базисним функцијама вишег реда, као и систематично испитивање конвергенције резултата. Студије самоконвергенције, засноване на *h*-, *p*- и *hp*-рафинацији, показале су да се одступања електричног поља и параметара расејања у односу на референтне вредности могу смањити на веома ниске нивое, што потврђује нумеричку стабилност и поузданост директног модела. Даље је показано да су диференцијалне величине које се користе за добијање микроталасних слика знатно мање осетљиве на геометријска поједностављења од апсолутних величина. Валидација заснована на резидуалима једначине инверзног расејања додатно је потврдила тачност симулационог модела, док су микроталасне слике остале стабилне током целокупног процеса рафинације.

Додатно, развијена је методологија за добијање еквивалентног хомогеног модела главе, применом формула за анализу диелектричних смеша и оптимизационих техника. Добијен је хомогени модел који показује веома добро слагање параметара расејања са оригиналним хетерогеним моделом, уз истовремено значајно смањење времена потребног за симулацију.

Кључне речи: антенски низ, антропоморфни фантом главе, микроталасно добијање слике, метода момената, анализа самоконвергенције, детекција можданог удара.

Научна област: Електротехника и рачунарство

Ужа научна област: Електромагнетика, антене и микроталаси

Table of Contents

Chapter 1: Introduction 1

Chapter 2: Characterization of a typical MMWI scenario 7

2.1. Anthropomorphic Head Phantom 9

2.2. Stroke 15

2.3. Antenna System 16

2.3.1. Basic Antenna Models 16

2.3.2. Novel Antenna Design 22

2.3.3. Semi-Automatic Design Procedure for the MMWI Antenna Helmet 24

2.4. Reference Head with average tissue properties 28

Chapter 3: Full-Wave Analysis Method for MMWI Simulations 32

Chapter 4: Controlled-Deviation Decimation and High-Fidelity Mesh Construction from STL Models 37

4.1. Avoiding Irregularities in Quad Mesh 38

4.2. Controlling Deviation from Initial STL Model 39

4.3. Quality Factors for Quadrilateral Elements 40

4.4. Initial Triangular Mesh Decimation 42

4.5. Triangle-to-Quad Mesh Conversion 45

4.6. Quadrilateral Mesh Refinement for Better Approximation of the STL Model 48

Chapter 5: Numerical Results and Validation of Accuracy-Controlled 3D EM Modeling 52

5.1. Self-convergence strategy for Electric Field 55

5.1.1. Relative Mean Absolute (RMA) Errors 55

5.1.2. h, p, and hp Refinements 56

5.1.3. Practical Scales and Computational Considerations 56

5.2. Representative Convergence Behavior ..... **Error! Bookmark not defined.**

5.2.1. Self-Convergence Testing for Electric Field 57
5.2.2. Self-Convergence Testing for Scattering Parameters 58
5.3. Influence of Surface Decimation on 3D EM Simulation Accuracy 60
5.4. Validation of 3D EM Simulation Outputs for MMWI Applications 62
Chapter 6: Conclusion 67
References 70
Biography 77
List of Publications 78

List of Figures

Figure 1. MMWI scenario for stroke diagnostics/monitoring: a) cross-section of head phantom with stroke, b) antenna system, and c) full scenario. 8
Figure 2. NEVA Electromagnetics anatomical human model used for 3D EM simulation studies. 9
Figure 3. Head phantoms with all domain parameters mapped to their respective tissue classes. (a) Head phantom obtained via a single crop-and-fill operation applied to original anatomical model. (b) Head phantom produced by a methodical pipeline with multiple crop-and-fill operations. 11
Figure 4. Head-region phantoms reconstructed under multiple maximum deviation constraints. (a) STL models of skull and brain, (b) WIPL-D model of skull and brain tissues with no decimation applied, and (c) WIPL-D model of skull and brain tissues with a maximum mesh decimation of 1 mm applied. 14
Figure 5. Stroke in the head. 15
Figure 6. Antenna Library for medical applications. (a) Microstrip trapezoidal patch antenna, (b) Refined microstrip trapezoidal patch antenna. (c) Pentagonal arm dipole antenna. (d) Open waveguide antenna. 18
Figure 7 $S11$-parameters of regular MTPR antenna. 19
Figure 8. $S11$-parameters of optimized MTPR antenna. 20
Figure 9. Optimized MTPR antenna placed near the head, (a) Position of antenna in respect to the head model, (b) $S11$-parameters. 21
Figure 10. Microstrip Hammer Patch antenna geometry. The Teflon filling of the coaxial feed is shown in gray, the FR4 substrate in green, and the matching medium in blue. 23
Figure 11. S_{11} versus frequency for antenna above the head is shown in the graph. 24
Figure 12. Upper portion of the head approximated by a half-ellipsoidal geometry 25
Figure 13. Octagonal footprint derived from the MTPR antenna geometry. 25
Figure 14. Semi-automatic way to create Helmet around the head. 26
Figure 15. MTPR Antenna Helmet, placed around NEVA head in honey-comb manner. 27
Figure 16. (a) Outer layer of the head, (b) interior layer with tissues of the NEVA model. 29
Figure 17. MMWI scenario with MTPR antennas. 31
Figure 18. (a) Head phantom with seven tissue layers, (b) Homogeneous head phantom. 31
Figure 19. Sketch of a bilinear quadrilateral surface and decomposition of surface current in the local psparametric system. 34
Figure 20. (a) Inflexed quadrilateral with both diagonals highlighted; (b) corresponding tetrahedral representation. 39
Figure 21. Decimation of a minimal polygon using the vertex-collapse method: (a) before and (b) after vertex collapse. 43
Figure 22. Skull and brain phantoms generated at different decimation levels: (a) no decimation, (b) σ_{max} = 1 mm, (c) σ_{max} = 2 mm, and (d) σ_{max} = 3 mm. 44
Figure 23. Triangle-to-quadrilateral mesh conversion procedure: (a) merging of adjacent triangles, (b) subdivision of a triangular element into three quadrilaterals, (c) subdivision of a quadrilateral into four quadrilaterals, and (d) illustration of the complete two-step conversion process. 47
Figure 24 . Quadrilateral mesh refinement for improved agreement with the original STL geometry: (a) displacement of newly generated nodes toward the nearest locations on the STL surface (red arrows), and (b) refined quadrilateral mesh after node adjustment 49
Figure 25. Quadrilateral meshes of the skull and brain obtained for different maximum allowed deviations: (a) no decimation, (b) σ_{max} = 1 mm, (c) σ_{max} = 2 mm, and (d) σ_{max} = 3 mm. 50
Figure 26. Number of mesh elements and RMS deviation for triangular and quadrilateral meshes. 51

Figure 27. Scattering parameters (Sij) of the seven-tissue reference head and the equivalent homogeneous head obtained using the optimized average dielectric properties. 53
Figure 28. Electric Field inside (a) head with seven tissues, (b) homogeneous head. 54
Figure 29. RMA error (%) vs. number of unknowns for electric field (blue) and differential electric field (orange). ..... **Error! Bookmark not defined.**
Figure 30. RMA error (%) vs. number of unknowns for S-parameters (blue) and differential S-parameters (orange). ..... **Error! Bookmark not defined.**
Figure 31. (a) Magnitude of electric field and (b) differential electric field in the symmetrical plane of the head excited broadside by plane wave. 60
Figure 32. RMA Error of S-parameters as a function of the Number of Unknowns needed for head for different values of the Maximum Allowed Deviation, σ_{max} 61
Figure 33. Minimal RMA error of S-parameters versus maximum allowed deviation. 62
Figure 34. RMA residual as a function of the total number of unknowns 65
Figure 35. MW images reconstructed using (a) the TSVD method and (b) the LSM method applied to 3D EM full-wave data. 66

List of Tables

Table I: ELECTRIC PROPERTIES OF MATERIALS USED IN –REAL-LIFE MWI SCENARIO, AT 1 GHZ 13
Table II. TISSUE ELECTRICAL PROPERTIES 28
Table III. RELATIVE VOLUMES OCCUPIED BY DIFFERENT TISSUES INSIDE THE HEAD 29
Table IV. RMS DEVIATION AND NUMBER OF TRIANGLES OBTAINED WITH DIFFERENT LEVELS OF MAXIMUM ALLOWED DEVIATION σmax. 45
Table V. NUMBER OF QUADS AND RELATIVE RMS DEVIATION 49
Table VI. AVERAGE DIELECTRIC VALUES WITH RELATIVE MEAN ABSOLUTE DEVIATION 53
Table VII. NUMBER OF UNKNOWNS AND EXECUTION TIME 54

Chapter 1:
Introduction

Conventional medical imaging, principally Magnetic Resonance Imaging (MRI) and Computed Tomography (CT), provides detailed and clinically trusted information. However, these systems are time-consuming, non-portable, and require specialized facilities. CT also uses ionizing radiation, while MRI is expensive and typically available only in large centers. These constraints limit rapid, repeated, or bedside use, especially in ambulances and emergency bays where timely decisions are essential. As a result, there is a potential requirement for complementary approaches that can extend access and shorten time-to-diagnosis without reducing clinical value [1], [2].

Medical Microwave Imaging (MMWI) has emerged as a strong candidate to fill this gap [3] – [6]. MMWI employs non-ionizing electromagnetic fields and compact antenna arrays to sense dielectric-property contrasts in tissue. The approach is noninvasive, potentially low-cost, and can be built as a portable system for close proximity real-time screening or monitoring. The present work investigates MMWI from a simulation-based perspective, with particular emphasis on the accuracy of the electromagnetic (EM) forward model. Since microwave imaging relies on the interaction of electromagnetic fields with complex biological tissues, the quality of the reconstruction depends directly on the accuracy of the computed fields and S-parameters.

Several brain-focused MMWI systems have been proposed over the past decade, demonstrating different approaches in terms of antenna configuration, operating frequency, coupling strategy, and imaging methodology. One of the earliest systems, the StrokeFinder [7], [8], employed a helmet-based arrangement of 12 transmit/receive triangular patch antennas operating in the 0.8–1.5 GHz frequency range. A water-based coupling layer was introduced to improve electromagnetic interaction with the head, while the acquired multistatic scattering data were processed using machine-learning-based classification techniques to distinguish between ischemic and hemorrhagic stroke rather than producing dielectric images.

Another notable system was developed at the University of Queensland for intracranial hematoma detection [9], [10]. This device utilized 16 corrugated or tapered slot antennas arranged in a circular configuration and operating over 1–4 GHz. Unlike many other designs, no coupling medium was employed. Instead, the antenna spacing was optimized to maintain mutual coupling below −20 dB. The imaging approach relied primarily on monostatic measurements, where each antenna recorded its own reflected signals to detect abnormalities within the head.

To improve imaging capability, the BRIM G2 system [11] adopted a significantly higher-density sensing architecture consisting of 177 ceramic-loaded rectangular waveguide antennas distributed on a semi-spherical chamber and operating near 1 GHz. A glycerin–water matching medium was used to enhance electromagnetic penetration into the head. Combined with microwave tomography algorithms, the system demonstrated the ability to detect, differentiate, and monitor ischemic and hemorrhagic stroke. However, the large number of antennas resulted in increased system complexity, cost, and reduced portability.

Subsequent research focused on reducing hardware complexity while maintaining imaging performance. A helmet-based microwave imaging device employing a 24-element antenna array was proposed, where the antenna layout was optimized using singular value decomposition (SVD) analysis of the scattering

operator [12]. Operating around 1 GHz, the system provided a practical balance between information content, imaging performance, and hardware complexity. Validation was performed using realistic three-dimensional head phantoms and full-wave electromagnetic simulations.

Further improvements investigated antenna and coupling-medium optimization. A system based on printed monopole antennas immersed in a 90% glycerol–water coupling medium was proposed for operation in the 0.6–2.5 GHz range [13]. Additionally, a split-ring resonator (SRR) metamaterial matching layer was introduced to improve transmission through the head by reducing impedance mismatch at the coupling-medium interface. Simulations performed on realistic head models demonstrated improved signal penetration and measurable scattering variations due to blood-mimicking inclusions.

Research has also explored advanced image reconstruction techniques. A microwave tomography system [14] based on 16 cavity-backed bowtie antennas arranged around the head combined differential measurements with a hybrid qualitative–quantitative imaging algorithm. The reconstruction procedure employed a synthetic aperture focusing technique (SAFT) for initial localization followed by a nonlinear dielectric property reconstruction stage. Numerical and experimental validations demonstrated successful localization and characterization of stroke-like abnormalities using realistic phantom models.

A significant development toward practical stroke monitoring was the introduction of a 3-D microwave imaging prototype based on a 24-antenna helmet-type architecture [15]. The system operated around 1 GHz and employed a differential imaging approach together with a TSVD based reconstruction algorithm. The antennas were integrated within dielectric coupling blocks and connected through a 24 × 24 switching network, enabling complete multistatic data acquisition. Experimental validation using anthropomorphic head phantoms demonstrated successful localization of stroke-like targets with dimensions relevant to clinical monitoring scenarios.

Later, a brick-antenna module was introduced to improve portability and ease of deployment [16]. The antenna consisted of a printed monopole embedded in a semi-flexible dielectric brick with relative permittivity close to 20, eliminating the need for liquid coupling media. The design provided stable operation over 0.8–1.2 GHz, improved robustness against head-position variations, and simplified conformal placement around the patient's head. Experimental studies demonstrated adequate wave penetration and successful detection of stroke-mimicking targets inside anthropomorphic head phantoms.

Regardless of the measurement system employed in MMWI, e.g., [7]–[19], its antennas must be designed and optimized for the specific body part being investigated to ensure adequate penetration of electromagnetic waves into the tissue and reliable measurement of the self and mutual S-parameters [20]. In numerical studies, the body part of interest is represented by a numerical phantom, i.e., an electromagnetic model that describes the geometry and dielectric properties of the constituent tissues. The phantom serves as a numerical representation of the measurement target, enabling the interaction between the antenna system and the biological tissue to be modeled and the corresponding electromagnetic response to be computed. It is therefore essential for evaluating the antenna system, generating synthetic measurement data, and testing MMWI reconstruction algorithms.

On the other hand, MMWI algorithms face the challenging task of reconstructing tissue abnormalities from weakly scattered signals, which can be several orders of magnitude smaller than the total measured signals. Their input typically consists of scattering parameters and, in many approaches, the electromagnetic field inside the body part of interest. However, the latter is often only approximately known due to the limited knowledge of the patient-specific healthy anatomy. The resulting electromagnetic data can be used either to reconstruct the spatial distribution of dielectric properties within the region of interest (quantitative imaging) or to identify the presence, location, and extent of tissue abnormalities relative to a reference or healthy condition (qualitative imaging) [21]–[23].

Thus, MMWI requires four key components: 1) realistic human phantoms, 2) a reliable measurement system 3) a robust reconstruction algorithm, and 4) an accurate and efficient 3D EM solver. This thesis addresses all four components by developing a complete MMWI measurement scenario, including an antenna system and realistic head phantoms with and without a stroke, evaluating the system response (e.g., scattering parameters and electromagnetic fields inside the head) using an established electromagnetic solver, and using the resulting data for stroke image reconstruction. However, the primary focus of the thesis is the development of realistic human head phantoms suitable for efficient electromagnetic analysis.

The objective of 3D EM modeling in MMWI is to accurately represent the complete measurement scenario, which may comprise a realistic multi-tissue phantom, an antenna array, and the surrounding matching medium [24], [25]. While antenna structures can be readily generated using conventional computer-aided design (CAD) tools and standard geometric formats, the development of anatomically realistic human phantoms remains considerably more demanding. Consequently, only a limited number of such models are available, primarily in Standard Tessellation Language (STL) [26] and voxel-based formats [27]. In this study, STL models are used to represent multiple layers of biological structures, with each tissue assigned its corresponding electromagnetic properties. These models provide the foundation for realistic electromagnetic simulations; however, their anatomical and geometrical complexity, particularly when combined with the antenna system, makes efficient 3D EM modeling challenging.

The 3D EM modeling approach must therefore provide the required level of engineering accuracy within a reasonable simulation time. This requirement becomes particularly important when simulations are repeatedly performed for antenna design optimization, system performance evaluation, parametric studies, and validation of microwave imaging algorithms. Depending on the specific application, the modeling process may require either higher accuracy or shorter simulation times, resulting in an inherent tradeoff between computational cost and solution accuracy. Efficient processing and appropriate simplification of complex phantom models are therefore essential for enabling large-scale MMWI simulations.

The most common numerical techniques used for electromagnetic modeling are [28]–[32]:

a) Surface-integral-equation-based techniques, primarily the Method of Moments applied to Surface Integral Equations (MoM/SIE), solve equivalent electric and magnetic currents on material boundaries discretized by surface elements such as triangles and quadrilaterals. Owing to their

reduced number of unknowns, these methods are computationally efficient for the analysis of piecewise homogeneous electromagnetic structures and surface-based anatomical models.

b) Volume-based techniques, including the Finite Element Method (FEM), Finite-Difference Time-Domain (FDTD) method, Finite Integration Technique (FIT), and the Method of Moments applied to Volume Integral Equations (MoM/VIE), solve for the electromagnetic fields throughout the computational domain. The geometry is represented by using volumetric elements, such as tetrahedra, hexahedra, or voxels, enabling accurate modeling of complex heterogeneous tissue distributions and anatomically detailed biological structures.

These methods require specific formats of numerical models of the phantoms. Surface-based techniques such as MoM/SIE using triangles are suited for STL models, whereas volume-based methods, including FEM, FDTD, FIT, and MoM/VIE using tetrahedrons and hexahedrons, are commonly applied to voxel models without further processing. In realistic anatomical phantoms, the initial number of surface or volume elements are extremely large, making full-wave 3D EM simulations computationally expensive and time-consuming. Therefore, it becomes necessary to reduce the complexity of the model through controlled simplification procedures. Such procedures should decrease the number of geometric elements and, when required, transform the geometry into a mesh suited with quadrilaterals/tetrahedrons, while maintaining a controlled deviation from the original model. The objective is to achieve a significant reduction in computational cost without compromising the acceptable accuracy of the electromagnetic data required for reliable MMWI analysis.

Further, with the reduction of the complexity of the scenarios it is difficult to estimate the accuracy of the 3D EM simulations of MMWI scenarios. Researchers adopt in general following strategies in general to assess the accuracy of the numerical models:

1) Validation against measured results: In this approach, simulation data such as S-parameters or computed electric field are compared against simplified fabricated models. While this provides an initial indication of solver consistency, its effectiveness is limited by the reduced anatomical and dielectric complexity of such configurations, which may not fully represent realistic head geometries and heterogeneous tissue properties [33]–[37].

2) Cross-validation using independent numerical solvers: Here, results obtained from a given numerical scenario are compared with those from established commercially available alternate solvers. Consistent results obtained from different solvers increase confidence in the adopted numerical model. However, this approach confirms agreement between implementations rather than absolute accuracy, as similar assumptions and discretization errors may be present in multiple solvers [35].

3) Self-convergence analysis: This approach evaluates the accuracy of a simulation using a single solver. Numerical parameters, such as mesh quality, solver accuracy, or basis-function order, are gradually refined until the calculated electromagnetic fields and S-parameters no longer show significant variation. Some authors recommend choosing these parameters to obtain satisfactory

results [32], [38], however, convergence studies specifically focused on MMWI applications are still limited. Therefore, defining suitable convergence criteria, error metrics, and accuracy thresholds for imaging-related quantities remains an important challenge in MMWI simulations [28], [39].

Because of the complexity of realistic MMWI scenarios, thorough validation of EM simulations is often difficult to perform. As a result, many researchers rely on established commercial simulation tools and assume that the generated electromagnetic data are sufficiently accurate for imaging purposes. In many cases, successful image reconstruction is regarded as indirect confirmation of the validity of the EM model [40]. However, when imaging performance is unsatisfactory, identifying the source of the failure becomes challenging. The problem may originate from limitations of the imaging algorithm, inaccuracies in the antenna system, hard simplification in the phantom model, or numerical errors introduced during EM analysis. Therefore, reliable procedures are required to assess the accuracy and stability of the forward EM solution independently of the imaging algorithm itself.

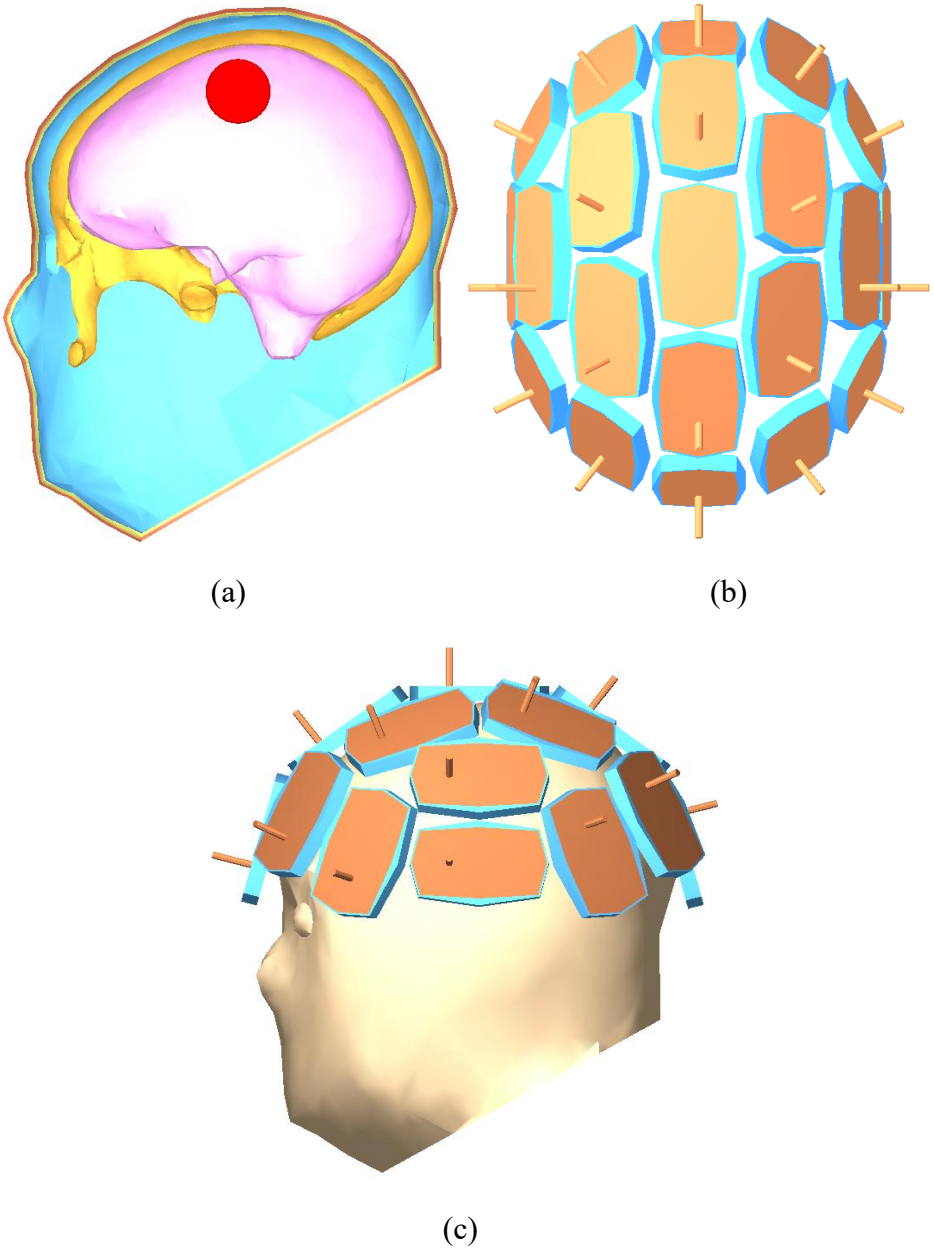
In this thesis, a novel decimation technique is developed to reduce the complexity of the original triangular STL-based anatomical models while preserving their relevant anatomical features and controlling the resulting geometric deviation. The decimated triangular meshes are subsequently transformed into quadrilateral meshes using a novel procedure, producing high-quality, simulation-ready models with explicitly controlled geometric deviation from the original anatomical models.

In addition to geometric deviation, a self-convergence methodology is introduced to quantify the stability of the electromagnetic response and establish practical accuracy criteria for MMWI applications under different levels of geometric simplification. The resulting EM data are further assessed using validation procedures based on the residual of the Inverse Scattering Equation (ISE). The proposed methodology is applied to realistic brain-imaging scenarios involving anatomically detailed head phantoms, stroke models, and multistatic antenna arrays. These investigations establish practical relationships between phantom complexity, electromagnetic accuracy, and computational cost, providing guidelines for the development of reliable and efficient MMWI simulation models.

The remainder of this thesis is organized as follows. Chapter 2 presents the representative MMWI scenario employed throughout this work, including the anatomical head phantom, stroke model, antenna system, and reference head formulation. Chapter 3 describes the full-wave 3D EM analysis method used in this study, including the MoM/SIE formulation, quadrilateral surface modeling, and higher-order basis functions. Chapter 4 introduces the proposed controlled-deviation decimation and high-fidelity quadrilateral meshing framework for transforming anatomical STL models into simulation-ready EM models. Chapter 5 presents the numerical results and validation of the proposed accuracy-controlled 3-D EM modeling framework. This chapter includes the development and assessment of the reference head model, the proposed self-convergence strategy, the impact of mesh decimation on simulation accuracy, and the validation of EM simulation outputs for MMWI applications. Finally, Chapter 6 summarizes the main contributions of the thesis and outlines directions for future research.

Chapter 2: Characterization of a typical MMWI scenario

This chapter presents an MMWI scenario, shown in Figure 1, for the evaluation of the proposed 3D EM modeling framework with controllable accuracy. The scenario is composed of several key elements identified in previous MMWI studies as essential for realistic electromagnetic modeling and imaging analysis [1]. The anatomical head phantom and the corresponding tissue representation are based on investigations reported in [24], [31]. The antenna and the system design follow the methodologies developed in [16], and the stroke model, coupling medium, and overall simulation framework are motivated by the studies presented in [12] and [29]. Based on these studies, the MMWI simulation framework consists of three main components: a realistic head phantom, a surrounding antenna array, and an EM solver.



(a) (b)

(c)

Figure 1. MMWI scenario for stroke diagnostics/monitoring: a) cross-section of head phantom with stroke, b) antenna system, and c) full scenario.

2.1. Anthropomorphic Head Phantom

In this study, EM simulations are performed using a full-wave Method of Moments/Surface Integral Equation (MoM/SIE) framework implemented in WIPL-D Pro [41]. The formulation computes equivalent electric and magnetic surface currents on discretized boundary interfaces represented by quadrilateral elements, enabling accurate geometric representation with manageable computational cost. Anatomically realistic human phantom models obtained from the NEVA (Bio) Electromagnetics database [42] are defined in STL format for both male and female anatomies. These models represent complete human bodies and are organized as multiple STL surfaces, each corresponding to a specific tissue boundary, such as organs, muscles, bones, nerves, blood vessels, skin, and fat. An example of such a multilayer anatomical model is shown in Figure 2 ("Static VHP – Female model v2.2," NEVA Electromagnetics).

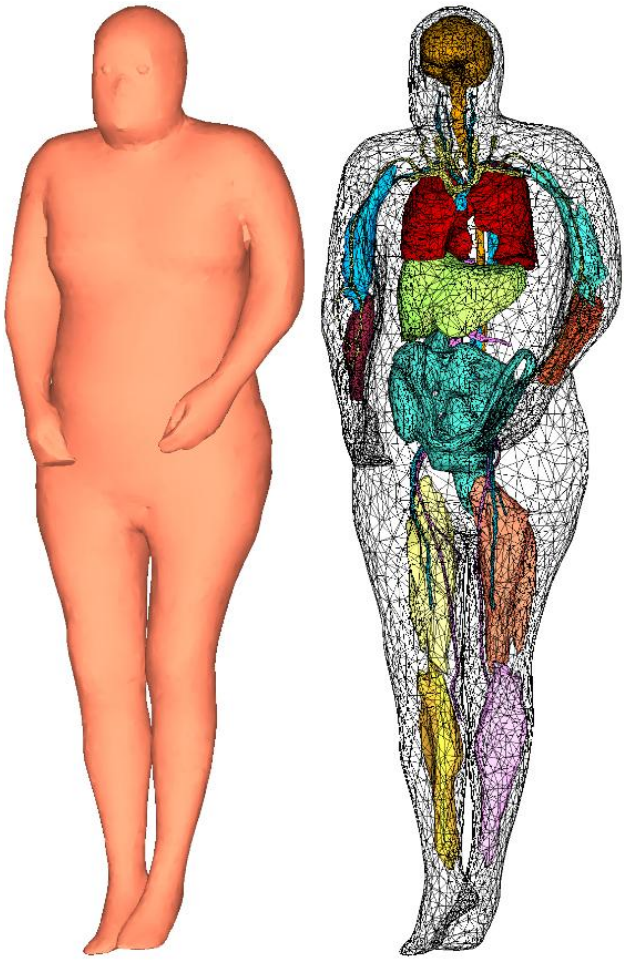


Figure 2. NEVA Electromagnetics anatomical human model used for 3D EM simulation studies.

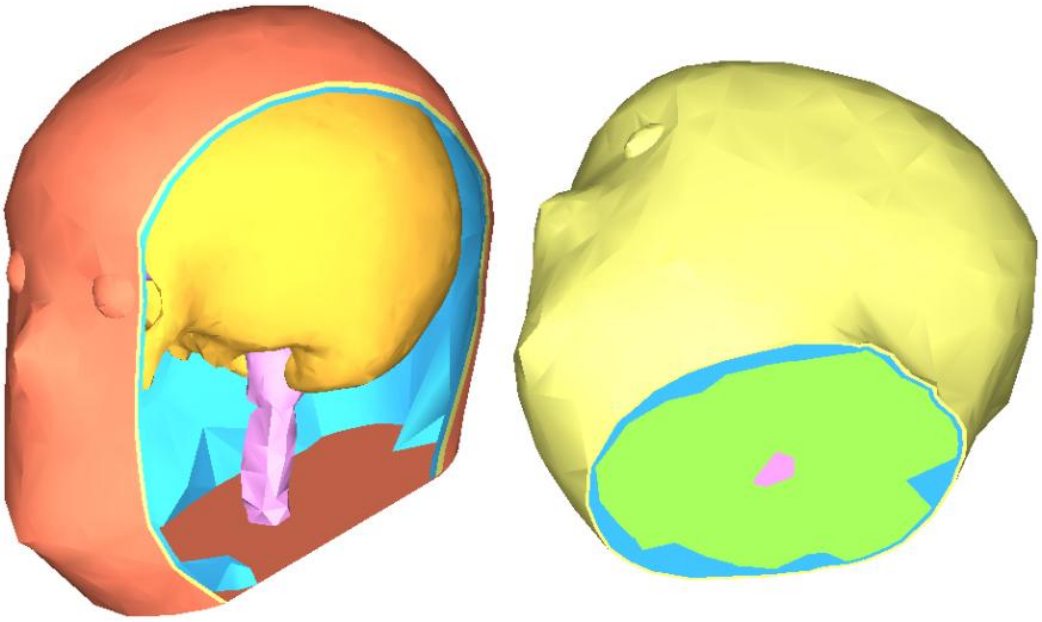
The NEVA phantom library provides a flexible foundation for a wide range of electromagnetic simulations involving medical devices and imaging systems. However, for MMWI applications such as stroke detection, the entire human model is not required. Instead, only the tissues that significantly influence microwave propagation within the head are retained. This targeted selection reduces the

complexity of the model and the number of unknowns in the numerical formulation, thereby improving computational efficiency while preserving the electromagnetic behavior relevant to the imaging problem.

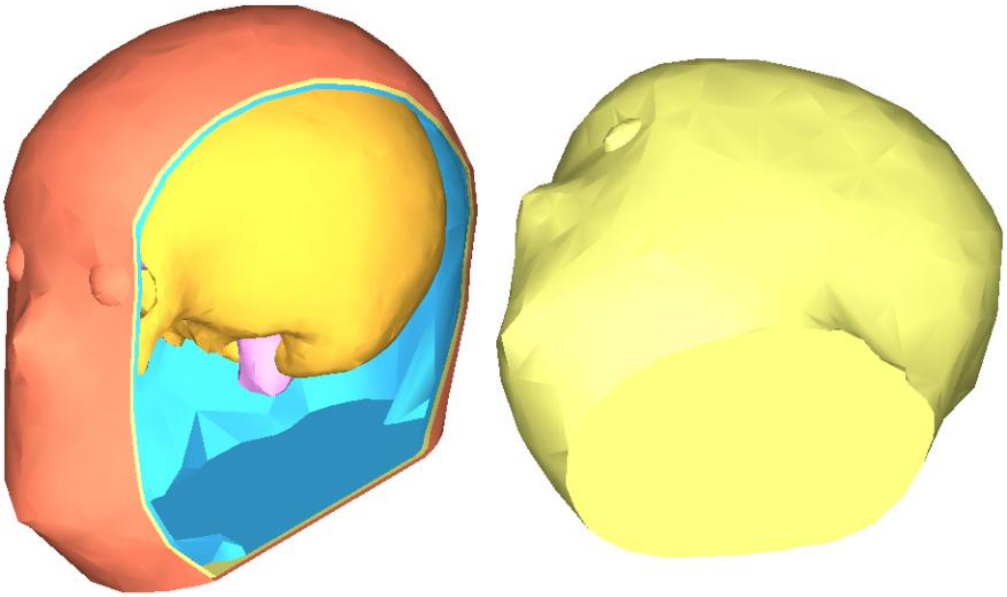
When defining a numerical MMWI scenario, the first step is to select an appropriate head phantom and identify the tissue classes required for accurate electromagnetic modeling. Previous studies have shown that stroke-related abnormalities are primarily located within the upper region of the head and in that region the most relevant tissues for microwave propagation include skin, fat, muscle, skull, white matter, gray matter, and cerebellum [43] – [47]. However, incorporating all anatomical details can significantly increase model complexity and computational cost. Furthermore, the literature indicates that several brain tissue layers may be combined without substantially affecting the accuracy of the simulated electromagnetic response [44] – [47]. Therefore, to achieve a balance between anatomical realism and computational efficiency, the present study considers five primary tissue layers: skin, fat, muscle, skull, and brain.

At the same time, model complexity must be controlled to ensure computationally efficient simulations and to support systematic self-convergence analysis. Therefore, the selected tissue representation focuses on the anatomically and electromagnetically dominant structures that have the greatest influence on the computed fields and S-parameters. Accordingly, two practical model-reduction strategies are adopted in this work.

(1) One practical approach to reducing model complexity is to process all relevant tissues simultaneously. In this method, the selected tissues, provided in individual STL files, are imported together into the simulation environment. As noted earlier, some tissue layers such as skin, fat, or muscle extend across the entire body, even though only the head region is needed for the stroke-detection scenario. To isolate the head, a single cropping operation is performed near the neck, which inevitably creates open boundaries at the cut surfaces. These newly formed openings must be closed to ensure that every tissue forms a completely enclosed structure suitable for electromagnetic simulation. This is achieved by closing the open regions with a single layer of surface patches. By precise use of the subtract/intersect Boolean operations, closure of the outermost skin layer is sufficient to ensure that all open anatomical structures are transformed into a fully closed computational model. The resulting geometry is a fully closed, well-connected head model with appropriate anatomical relationships and no open surfaces. Figure 3(a) shows the final head structure generated using this approach.



(a)



(b)

Figure 3. Head phantoms with all domain parameters mapped to their respective tissue classes. (a) Head phantom obtained via a single crop-and-fill operation applied to original anatomical model. (b) Head phantom produced by a methodical pipeline with multiple crop-and-fill operations.

(2) A second approach is to isolate and process each extended tissue individually. In this method, a single tissue layer (e.g., skin) is first imported from the tissue library, cropped at the neck, and its open boundary closed using an appropriate meshed patch. The same procedure is then applied to other extended tissues (e.g., fat, muscle) using different cropping planes to ensure that the tissues remain separate and non-intersecting during preprocessing. As a result, each extended tissue has its own opening near the neck that is independently closed with a dedicated mesh. After closing all open boundaries, the individually prepared tissue surfaces are assembled into a single head model. This produces a well-organized numerical representation in which each layer remains distinct, facilitating material assignment, mesh quality control, and solver stability. The final integrated model created by this sequential approach is illustrated in Figure 3(b).

The second, more systematic approach offers additional benefits in terms of model efficiency and electromagnetic accuracy. This approach reduces the overall computational burden while maintaining a clear separation between the tissue layers and the surrounding vacuum region. Proper isolation of high-permittivity tissues minimizes unwanted multiple scattering at tissue interfaces, which improves numerical stability and supports more efficient simulations. Owing to these advantages, the systematic approach is adopted throughout this work for both simulation and imaging studies. The quantitative impact of this approach on mesh complexity and computational efficiency is discussed in later sections following the introduction of the decimation and meshing procedures.

In the imported STL models, each tissue is represented only by its geometric boundary; the files do not contain electromagnetic properties. Consequently, the next step is to assign frequency-dependent dielectric parameters to each boundary surface corresponding to the selected tissues. In this work, we use the material library available in the 3D EM solver, which provides a comprehensive set of human tissue properties parameterized over frequency. These data are modeled using the Cole–Cole dispersion formulation [48], ensuring that both real and imaginary parts of the permittivity (and, implicitly, effective conductivity) are captured consistently across the operating band.

Formally, the complex relative permittivity $\varepsilon_r^*(\omega)$ for each tissue is expressed by the Cole–Cole model as

$$\varepsilon^*(\omega) = \varepsilon'(\omega) - j\varepsilon''(\omega) = \varepsilon_\infty + \frac{\Delta\varepsilon}{1+(j\omega\tau)^{1-\alpha}} + \frac{\sigma_s}{j\omega\varepsilon_0} \quad (1)$$

where ω is the angular frequency, $\varepsilon'$and ε'' are the frequency-dependent real and imaginary components of the complex permittivity, and ε_∞, σ_s, τ and α are Cole-Cole parameters derived from experimental measurements.

The choice of operating frequency is critical for the proper functioning of MMWI systems. Prior investigations [48] indicate that the 0.5–2.5 GHz band offers a favorable balance between penetration depth, spatial resolution, and signal-to-noise ratio for MWI applications. Within this range, 1 GHz has been recommended for single-frequency operation, as it provides sufficient sensitivity to intracranial dielectric variations while maintaining practical simulation accuracy conditions and manageable computational demands. This study adopts 1 GHz. The electrical properties of the head tissues at 1 GHz, including the stroke inclusion (modeled as blood), are summarized in Table 1.

Table I: ELECTRIC PROPERTIES OF MATERIALS USED IN –REAL-LIFE MWI SCENARIO, AT 1 GHZ

Material	ε_r	σ
Skin	45.711	0.8814
Fat	11.294	0.1164
Muscle	45.662	0.8871
Skull	20.584	0.3639
Brain	52.282	0.9854
Blood	61.065	1.5829

Defining the set of relevant tissues and assigning their electrical properties at the chosen operating frequency establishes the baseline simulation environment. From a numerical efficiency standpoint, it is advantageous to employ quadrilateral surface meshes rather than the default triangular STL meshes, and to use higher-order basis functions in preference to lower-order ones [49]. The conversion of STL models into simulation-ready quadrilateral meshes can be performed using different levels of complexity. The simplest approach is a brute-force triangle-to-quadrilateral conversion, in which each triangular element is subdivided into three quadrilateral elements. While this procedure preserves the original geometry, it substantially increases the number of mesh elements and consequently the computational cost of the simulation.

To improve computational efficiency, we proposed [24] a more advanced approach with controlled accuracy, which is detailed in Chapter 4. The process begins by merging all neighboring triangles when they share identical material properties and the angle between their unit surface normals is less than 5°. Owing to this restriction, approximately 20–30% of the original triangles typically remain unmerged, producing a mixed triangle–quadrilateral mesh. To obtain a pure quadrilateral representation, the merged quadrilaterals and remaining triangles are subsequently subdivided into four and three quadrilateral elements, respectively. As a result, the final number of quadrilateral elements becomes slightly more than twice the number of triangles in the original STL model.

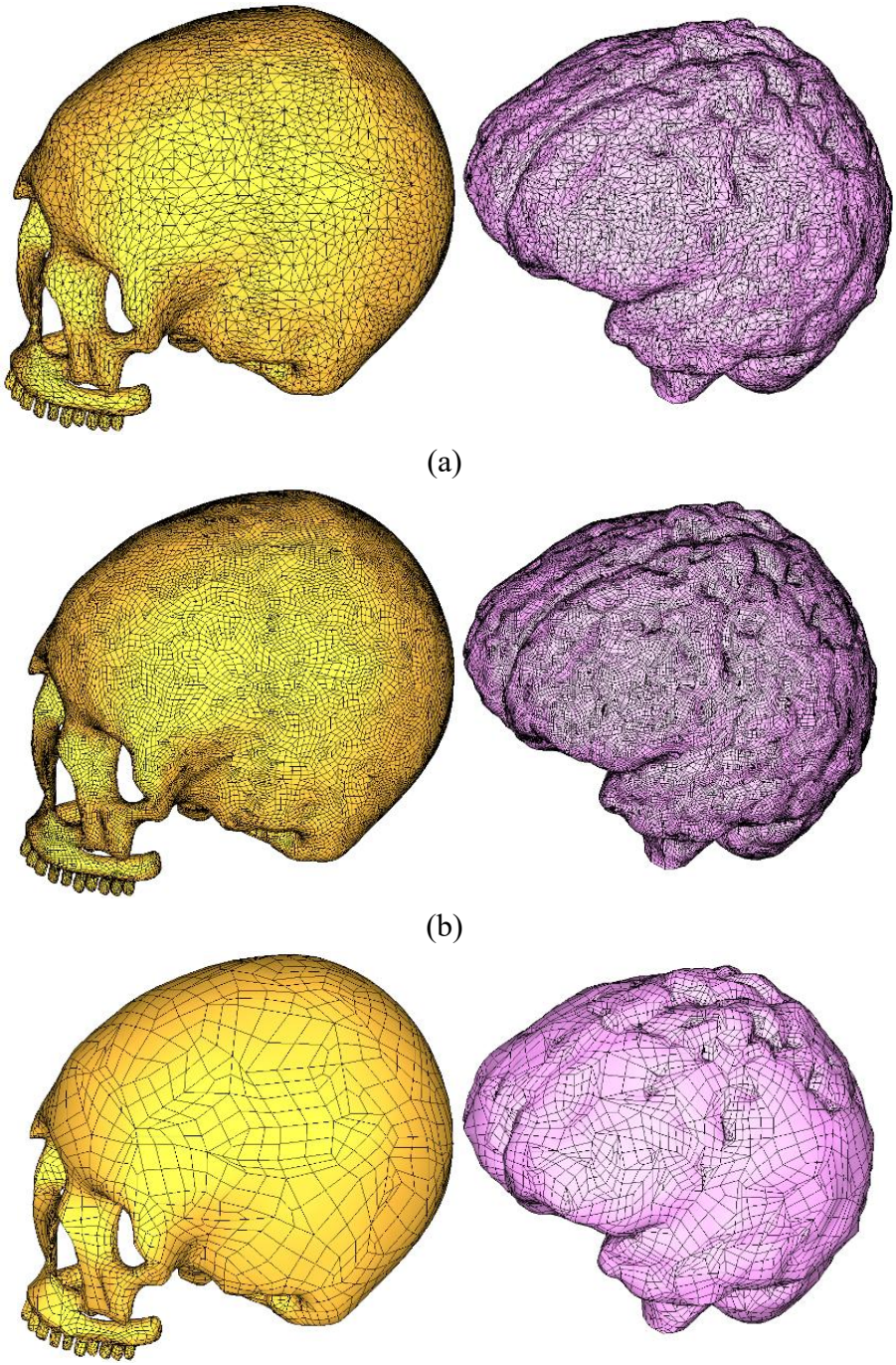


Figure 4. Head-region phantoms reconstructed under multiple maximum deviation constraints. (a) STL models of skull and brain, (b) WIPL-D model of skull and brain tissues with no decimation applied, and (c) WIPL-D model of skull and brain tissues with a maximum mesh decimation of 1 mm applied.

Further reduction in computational complexity is achieved through surface decimation, where the mesh density is controlled by a predefined maximum allowed geometric deviation $\sigma_{\max}$[29]. The decimation process is particularly useful for anatomically realistic phantoms containing a large number of surface elements. In this work, decimation is performed only if the resulting geometric deviation remains below

the specified tolerance. This procedure reduces the total number of triangles while preserving the overall anatomical shape and dimensions of the phantom.

During the quadrilateral meshing stage, all newly generated nodes are projected back onto the original STL surface. This refinement process reduces the average geometric deviation between the final quadrilateral mesh and the source STL model. Furthermore, both the decimation and meshing procedures can be applied to multilayer anatomical structures, as the algorithms are specifically designed to prevent intersections between adjacent tissue boundaries.

For the head phantoms considered in this study, the original STL representation contains 8362 triangular elements. Direct quadrilateral meshing without decimation produces a model consisting of 18,664 quadrilateral plates. In contrast, applying the meshing procedure after decimation with $\sigma_{\max} = 3\text{mm}$ reduces the model to approximately 6850 quadrilateral plates, corresponding to a reduction of nearly 63% in the number of mesh elements. Despite allowing a maximum geometric deviation of 3 mm, the resulting mesh exhibits an RMS deviation of only 0.506 mm from the original STL geometry. These results demonstrate that substantial reductions in model complexity can be achieved while maintaining high geometric fidelity. A visual comparison of the phantom complexity at different decimation levels is presented in Figure 4.

To further improve mesh quality and provide explicit control over geometric accuracy, the present work adopts a more advanced mesh-generation framework, described in detail in Chapter 4.

2.2. Stroke

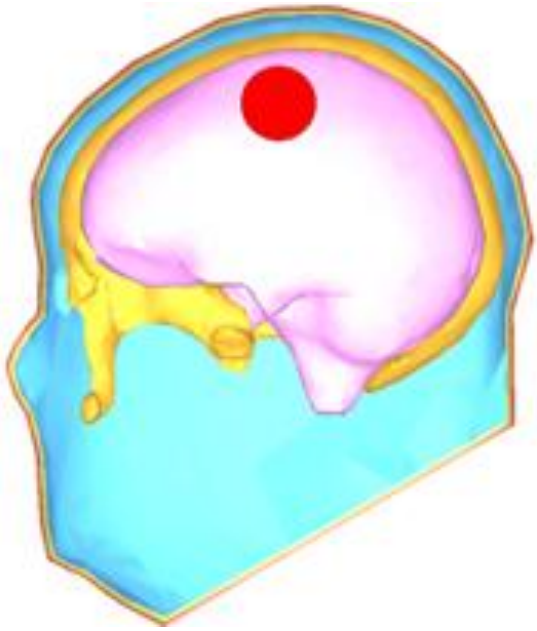


Figure 5. Stroke in the head.

In this study, the stroke lesion is represented by a spherical inclusion of radius $R_{\text{stroke}} = 15$ mm, composed of blood, and positioned within the brain, as illustrated in Figure 5. From a physiological perspective, stroke can be ischemic (reduced perfusion due to arterial occlusion) or hemorrhagic (intra- or extra-parenchymal bleeding).

To support forward modeling and subsequent inversion, the stroke inclusion is treated as a homogeneous, frequency-dispersive region (material parameters provided in Table I at 1 GHz and over the operating band).

2.3. Antenna System

In recent years, a wide range of antennas have been developed for medical microwave imaging applications, several of which were reviewed in our earlier work [20]. The antenna element and array configuration adopted in this thesis are inspired by the designs presented in [15], [16]. Building upon these studies, a library of well-matched and optimized antenna elements has been developed to provide stable multistatic responses for MMWI simulations. This section first introduces the fundamental antenna design concept, followed by the selected antenna configuration and its geometrical details. The semi-automatic procedure used to generate the 21-element antenna array for MMWI applications is also described.

2.3.1. Basic Antenna Models

The antennas are defined using a parametric representation, which enables direct control of key geometric dimensions and operating frequency. Although the designs are optimized for operation near 1 GHz, the center frequency can be adjusted by scaling the antenna dimensions through a set of symbolic parameters. This parameterized approach facilitates rapid design modifications and array optimization while preserving the overall antenna characteristics and eliminating the need for a complete redesign.

For MMWI applications, efficient electromagnetic coupling between the antenna and the head phantom is essential. Therefore, each antenna is excited through a coaxial feed and incorporates a matching layer between the radiating element and the phantom surface. This layer reduces impedance mismatch at the air–tissue interface, improves field penetration into the head, and helps maintain stable coupling among array elements. The parametric models also enable optimization of antenna position, orientation, and spacing, which directly influence the quality of the computed self- and mutual S-parameters used for imaging.

The antenna library includes several antenna types specifically developed for biomedical microwave imaging applications [16]. The antenna variants considered in this work are summarized below:

- Microstrip Trapezoidal Patch (MTP) antenna: The MTP is a compact, planar radiator offering a favorable balance among footprint, impedance bandwidth, and manufacturability. The trapezoidal geometry provides additional degrees of freedom compared with a rectangular patch (e.g., base widths, trapezoid height), enabling fine tuning of the input match near 1 GHz and

shaping of the near-field distribution for improved coupling through the matching spacer. Its low-profile structure is compatible with dense, helmet-like arrays and supports repeatable element placement.

- Refined Microstrip Trapezoidal Patch (MTPR) antenna: The MTPR extends the MTP by introducing geometric refinements (e.g., notches, tapered edges, slotting, or feed repositioning) to further broaden the operational bandwidth, stabilize input matching across the target band, and moderate surface currents that drive mutual coupling. These refinements yield more uniform element behavior over frequency, which benefits calibration and reduces sensitivity to small placement tolerances within the array.
- Pentagonal Arm Dipole (PAD) antenna: The PAD employs shaped dipole arms with pentagonal contours to realize a smoother input-impedance profile and to influence the near-field penetration characteristics in the presence of the spacer. Compared to straight-arm dipoles, the shaped geometry provides extra tunable parameters (edge lengths, vertex angles) to balance return loss, radiation pattern stability, and inter-element isolation.
- Open Waveguide (OWG) antenna: The OWG is a compact aperture radiator that excites a controlled near field at the open end of a short waveguide section backed by a coaxial feed and integrated with the matching spacer. Its aperture-type coupling can provide good penetration into lossy biological media while maintaining manageable edge diffraction and sidelobe content for close-proximity operation.

Across all four types, parametric definitions allow the central frequency to be adjusted around 1 GHz, with automatic scaling of critical dimensions to maintain a reasonable starting match. This library thus provides a flexible and robust foundation for constructing dense arrays with controlled coupling, reliable S-parameter measurements, and improved MWI reconstruction performance. The antennas are shown in Figure 6.

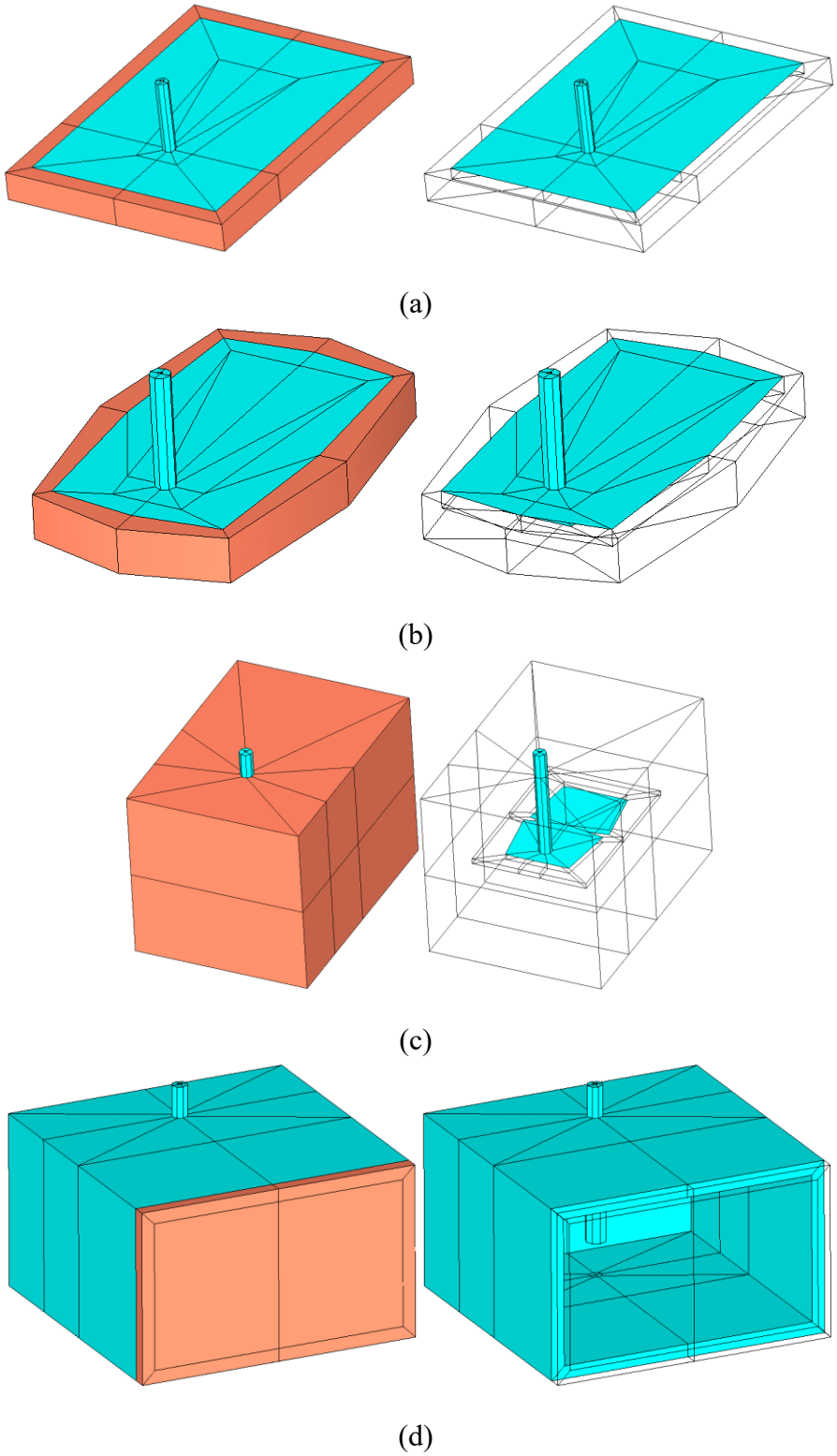


Figure 6. Antenna Library for medical applications**. (a)** Microstrip trapezoidal patch antenna, (b) Refined microstrip trapezoidal patch antenna. (c) Pentagonal arm dipole antenna. (d) Open waveguide antenna.

For reliable performance of MWI reconstruction algorithms, the antenna array must be well matched. In practice, impedance matching should be validated for two conditions: (i) antennas suspended in air (vacuum) and (ii) antennas operating in the presence of the head model. For the pre-liminary study we selected MTPR antenna, provides a suitable starting point because it is already parameterized for operation around a central frequency of 1 GHz. As an initial verification, the reflection coefficient of the standalone MTPR in vacuum was computed over 0.8–1.2 GHz; the result is shown in Figure 7, confirming an adequate match near the design frequency and establishing a baseline before loading effects from the head phantom and matching medium are introduced.

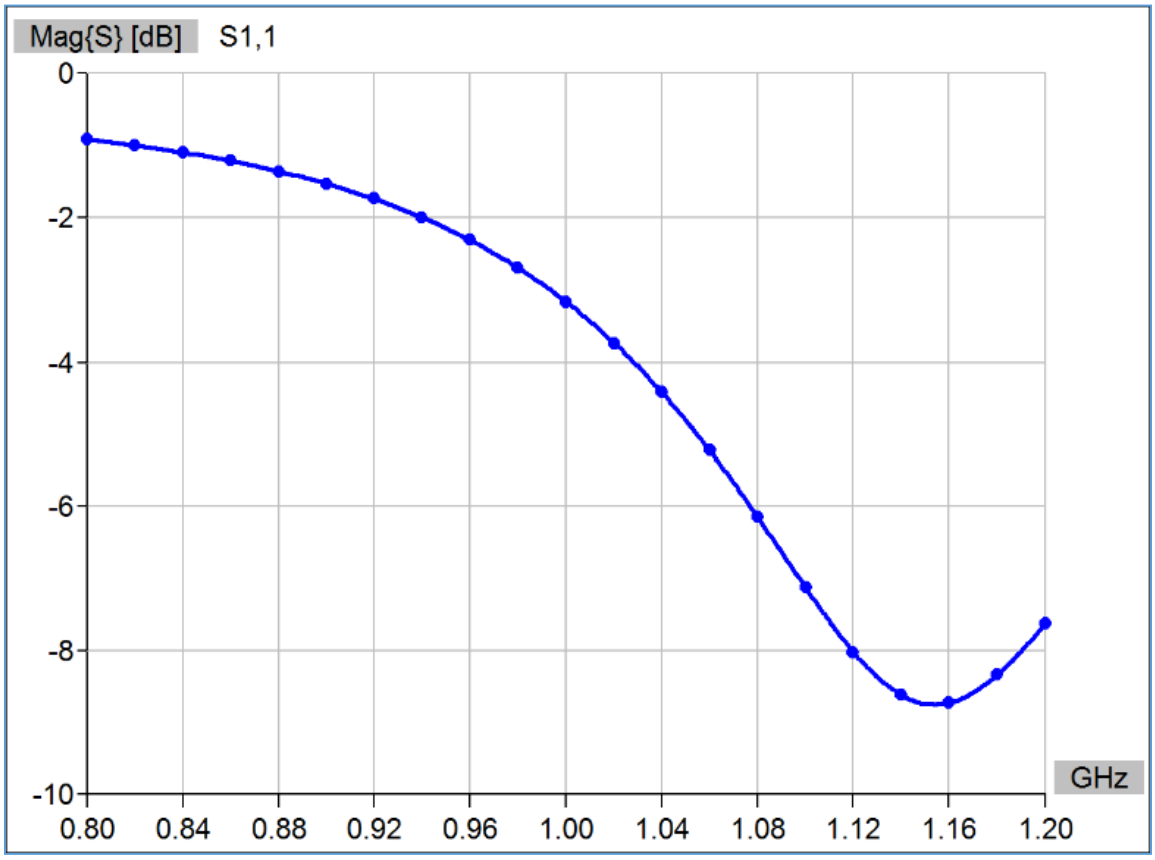


Figure 7 S_{11}-parameters of regular MTPR antenna.

To improve impedance matching around 1 GHz, we employed the WIPL-D optimization tools to tune several geometric parameters of the MTPR antenna simultaneously. The optimization was carried out at five frequency points: 0.90, 0.95, 1.00, 1.05, and 1.10 GHz with target reflection-coefficient levels of $|S_{11}| < -15$ dB, < -15 dB, < -20 dB, < -15 dB, and < -15 dB, respectively. These targets ensure a stronger match at the center frequency (1 GHz) while maintaining acceptable matching across the immediate band of interest, which supports both single-frequency operation and narrowband sweeps commonly used in MMWI.

The optimization workflow combined global and local search strategies to balance exploration and fine tuning. First, 75 iterations of Particle Swarm Optimization (PSO) were used to broadly explore the design

space and identify promising regions for the antenna dimensions under specified constraints. This was followed by 275 iterations of a simplex (Nelder–Mead) optimization to refine the solution, improving the local fit to the $|S_{11}|$ targets at the selected frequency points.

This procedure provides an antenna configuration with consistent matching performance near 1 GHz, creating a reliable basis for array-level calibration, if needed, the same optimization framework can be re-centered to nearby frequencies (e.g., 0.9–1.1 GHz) simply by adjusting the symbolic central-frequency parameter and re-running the optimization.

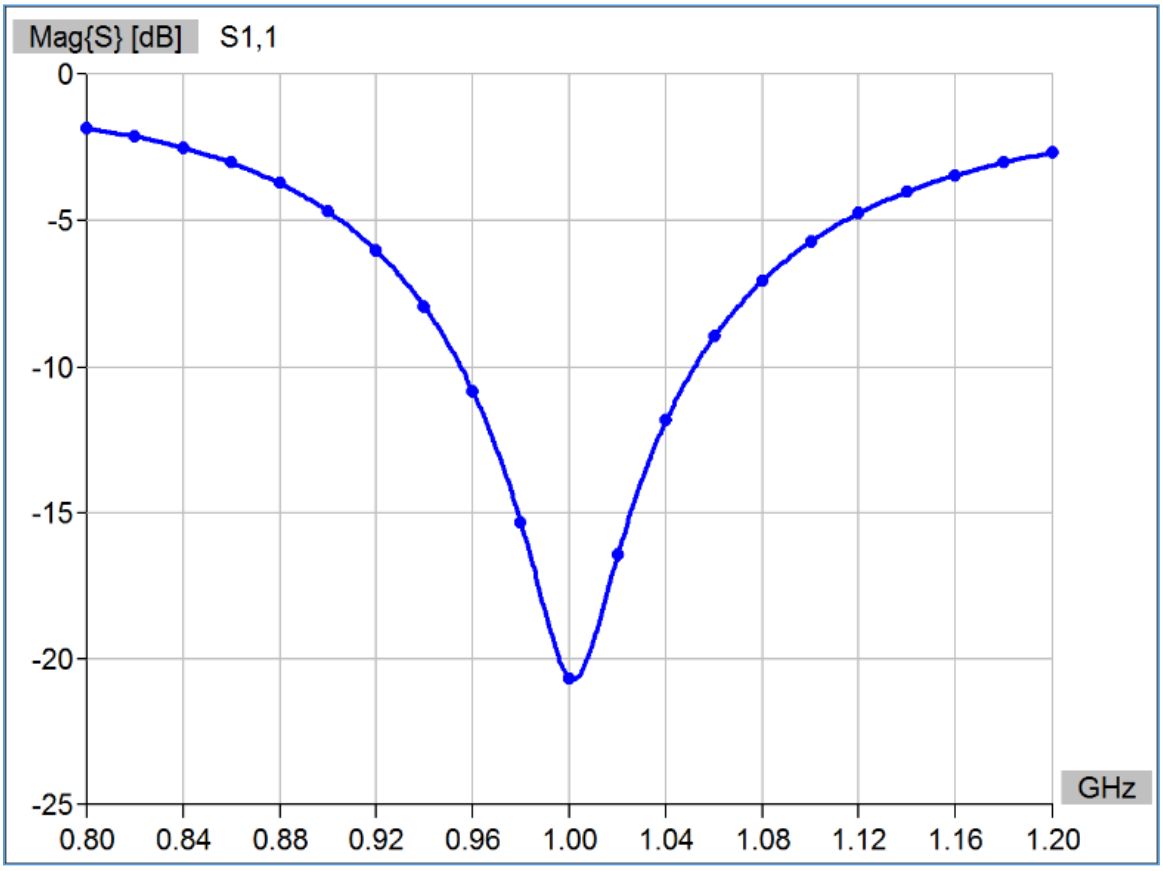
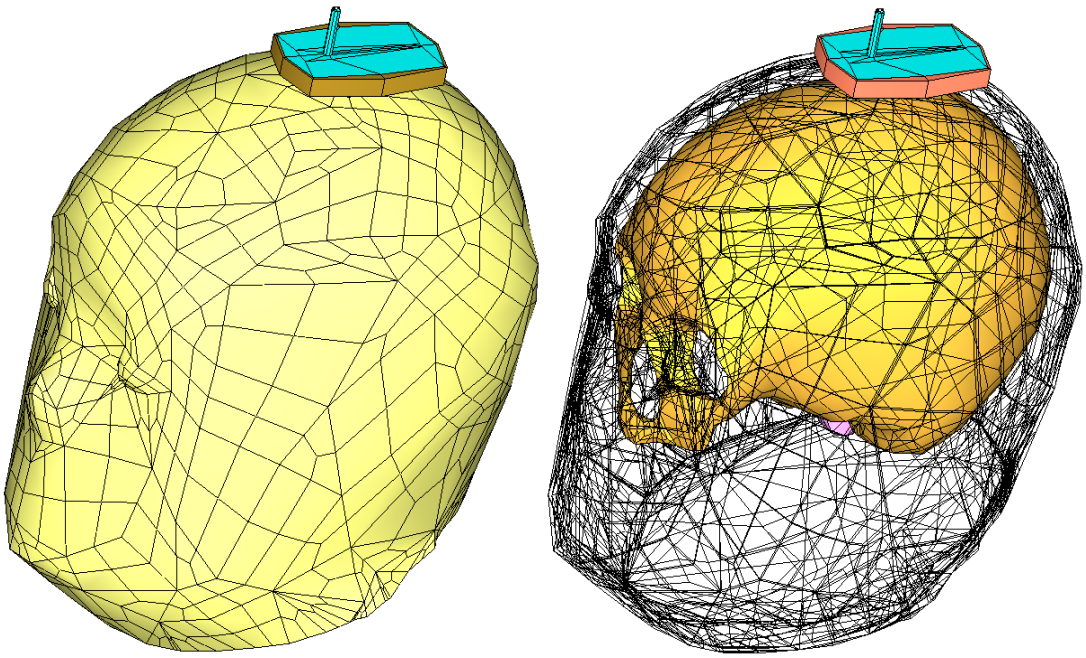
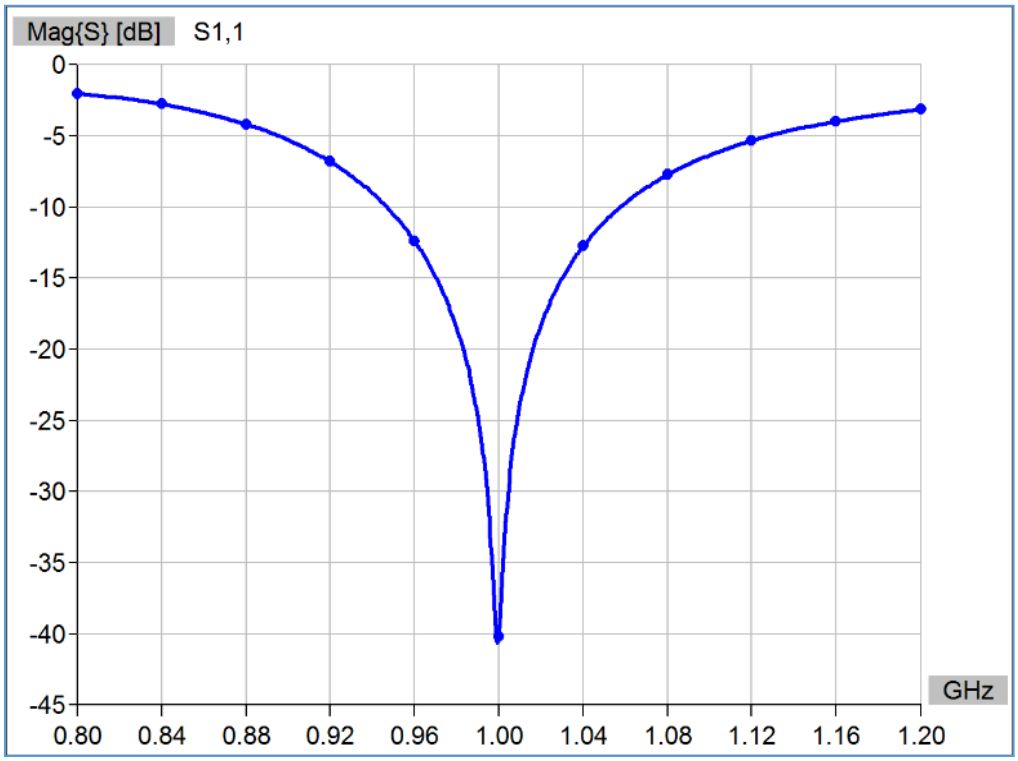


Figure 8. S_{11}-parameters of optimized MTPR antenna.



(a)



(b)

Figure 9. Optimized MTPR antenna placed near the head, (a) Position of antenna in respect to the head model, (b) $\boldsymbol{S_{11}}$-parameters.

For the antenna optimization, computations were carried out on a desktop workstation equipped with an Intel® Core™ i7-920 CPU (2.67 GHz) and 32 GB RAM. The complete optimization required

approximately two hours (7,224 s). The resulting reflection coefficient $|S_{11}|$ of the optimized MTPR antenna in vacuum, evaluated over the 0.8–1.2 GHz band, is presented in Figure 8, confirming improved impedance matching around the 1 GHz design frequency. Although target values were specified at multiple frequency points during the optimization process, the primary objective was to maximize antenna matching around the operating frequency of 1 GHz. Consequently, the optimization successfully reduced S_{11} below −20 dB at 1 GHz, while maintaining acceptable matching levels at the neighboring frequencies. Small deviations from the prescribed targets at some frequencies are a consequence of the trade-off between broadband matching and optimal performance at the center frequency, which is the most critical frequency for the considered MMWI scenario.

Before integrating the optimized antennas into the full measurement setup, it is essential to evaluate the reflection coefficient $|S_{11}|$ of a single element positioned in proximity to the head phantom. This step quantifies the loading effects introduced by the matching medium and the dielectric properties of the tissues. As a practical criterion for array development, if the simulated $|S_{11}|$ remains below −10 dB across the frequencies of interest, the antenna match is considered adequate to proceed with construction of the helmet-shaped array. If this condition is not met, additional local optimization is required with the antenna model.

Figure 9(a) shows the optimized MTPR antenna positioned near the head phantom with the matching medium. The reflection coefficient shown in Figure 9(b) remains below −10 dB around the operating frequency of 1 GHz, indicating good impedance matching. This ensures efficient coupling with the phantom and reliable computation of self- and mutual S-parameters for microwave imaging. Based on these results, the antenna is further optimized within the presence of matching media to fit better in the helmet shape in honey-comb manner

2.3.2. Novel Antenna Design

The antenna developed for MMWI studies in the literature is a microstrip patch antenna printed on an FR4 substrate. To increase the operating bandwidth, the antenna is implemented using two overlapping FR4 layers and embedded within a thin matching-medium spacer, as shown in Figure 10. The matching medium has a relative permittivity of 18.425 and conductivity of 0.204 S/m, while Teflon and FR4 have relative permittivity of 1.975 and 4.4, and loss tangents of 0.0002 and 0.03, respectively.

The antenna is excited through a Teflon-filled coaxial feed line of length L_{coax} = 20 mm. The inner and outer conductor radii A_{coax} = 0.47 mm and B_{coax} = 1.51 mm, respectively, resulting in a characteristic impedance of Z = 50 Ω. All metallic parts of the antenna are modeled using copper, and conductor losses due to skin effect and surface roughness are considered through an effective conductivity of σ = 19 MS/m. This configuration provides good impedance matching, sufficient bandwidth, and efficient electromagnetic coupling with the head phantom for MMWI applications.

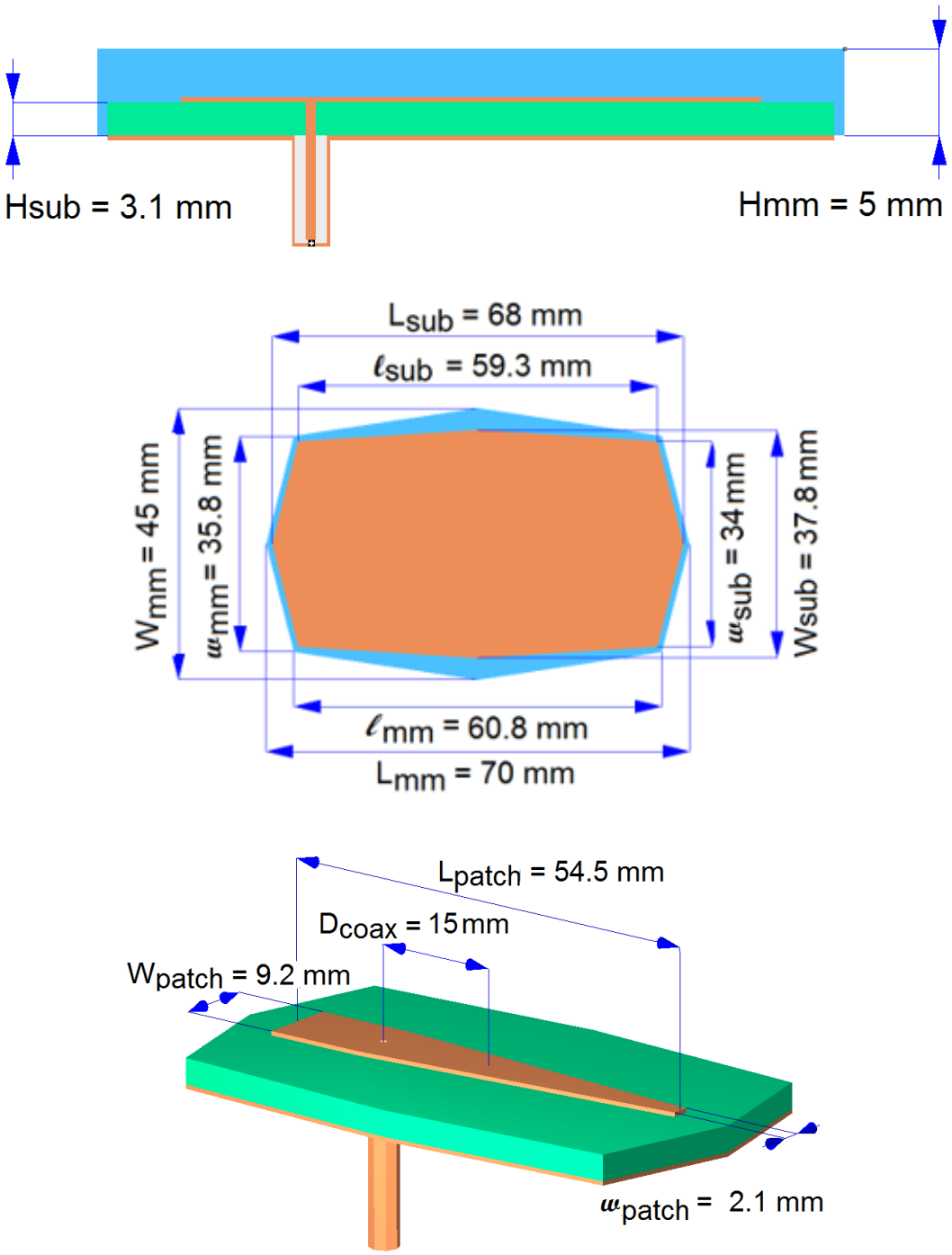


Figure 10. Microstrip Hammer Patch antenna geometry. The Teflon filling of the coaxial feed is shown in gray, the FR4 substrate in green, and the matching medium in blue.

As mentioned in the previous section, a single antenna is first placed in the vicinity of the head phantom to optimize its operating parameters. The optimization process is carried out in two stages. First, the stand-alone antenna is optimized to maximize the impedance bandwidth around the target operating frequency of $f_0 = 1$GHz. Subsequently, the antenna is optimized in the presence of the head phantom, as illustrated in the inset of Figure 10, to account for the influence of the surrounding biological tissues on its electromagnetic performance. The final dimensions of the optimized antenna are shown in Figure

10. Owing to its characteristic hammer-shaped patch geometry, the antenna is referred to as the Microstrip Hammer Patch (MHP) antenna. The calculated S-parameter responses for both optimization stages are presented in Figure 11.

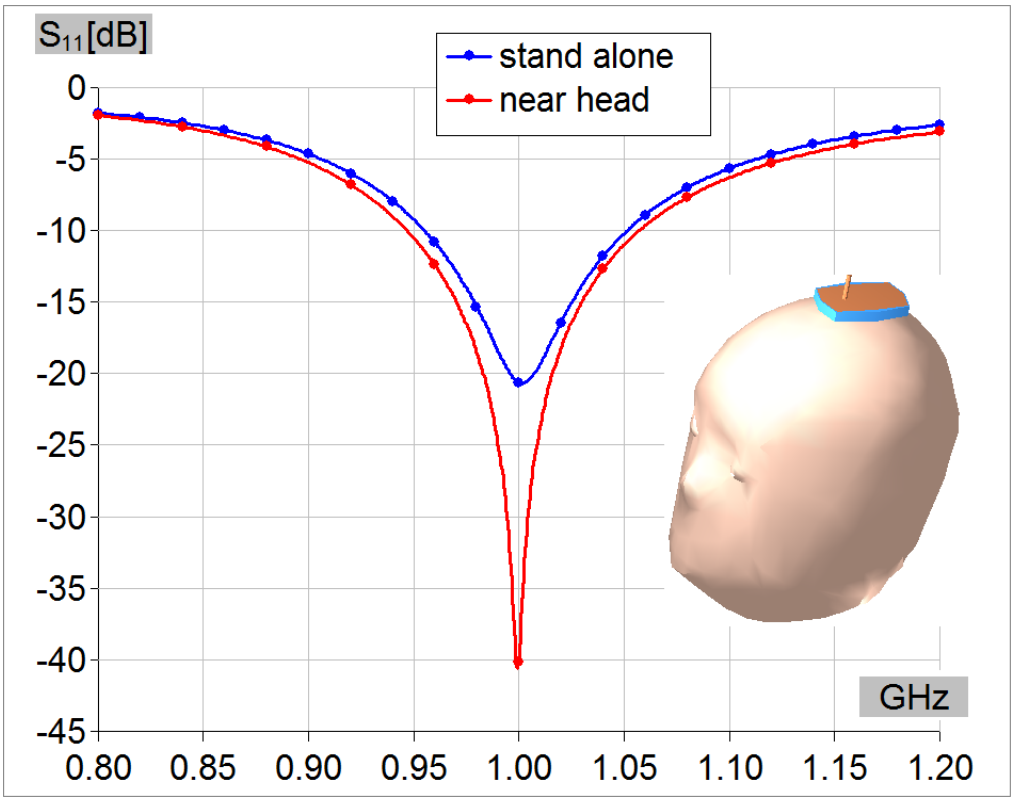


Figure 11. S_{11} versus frequency for antenna above the head is shown in the graph.

2.3.3. Semi-Automatic Design Procedure for the MMWI Antenna Helmet

The antenna array is a key component of an MMWI system, as it directly influences the quality and reliability of the simulated electromagnetic data. To maximize imaging performance, the antenna elements should be positioned as close as possible to the body surface while providing broad coverage of the region of interest within a compact array configuration. To achieve this objective for the NEVA head phantom, a semi-automatic antenna-helmet design procedure is employed. In the first step, a half-ellipsoid is fitted to the portion of the head that is intended to be covered by the antenna array, as shown in Figure 12. The position and dimensions of this half-ellipsoid are determined to best approximate the head geometry. Additional input to the design procedure is the footprint of the selected antenna element, represented by either a rectangular or octagonal shape, as illustrated in Figure 13. These inputs are then used to generate the antenna array geometry around the head phantom in a systematic and repeatable manner.

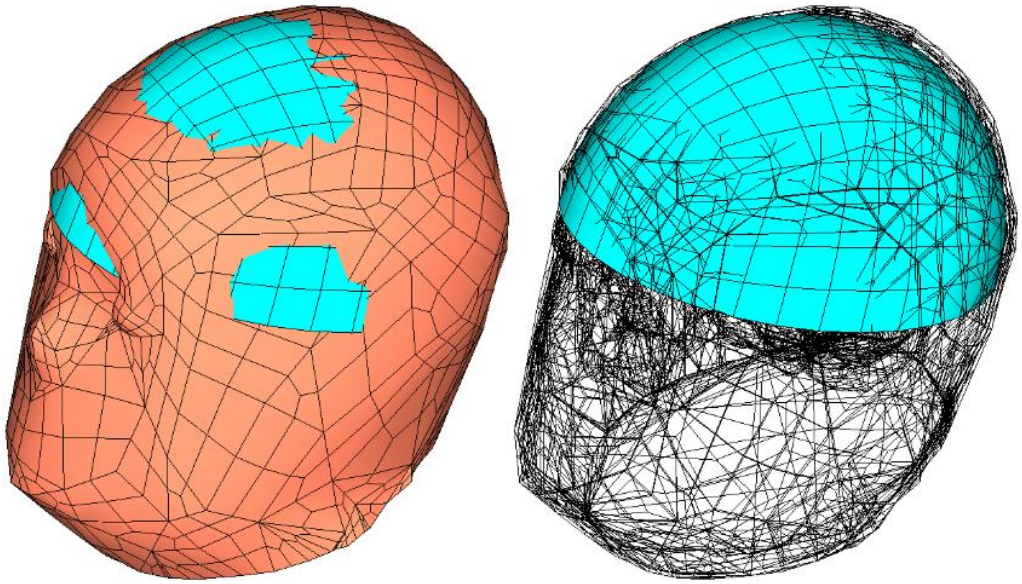


Figure 12. Upper portion of the head approximated by a half-ellipsoidal geometry.

In the next step, 21 octagonal footprints are distributed symmetrically over the half-ellipsoidal surface using a semi-automatic design algorithm. The algorithm determines the antenna locations and optimizes their placement to achieve dense coverage of the head while preventing overlap between adjacent elements. The number of antennas is selected as 21, corresponding to the maximum number that can be accommodated on the ellipsoidal surface. The resulting arrangement places the antenna footprints close to the head surface, as shown in Figure 14, providing a compact and conformal array configuration.

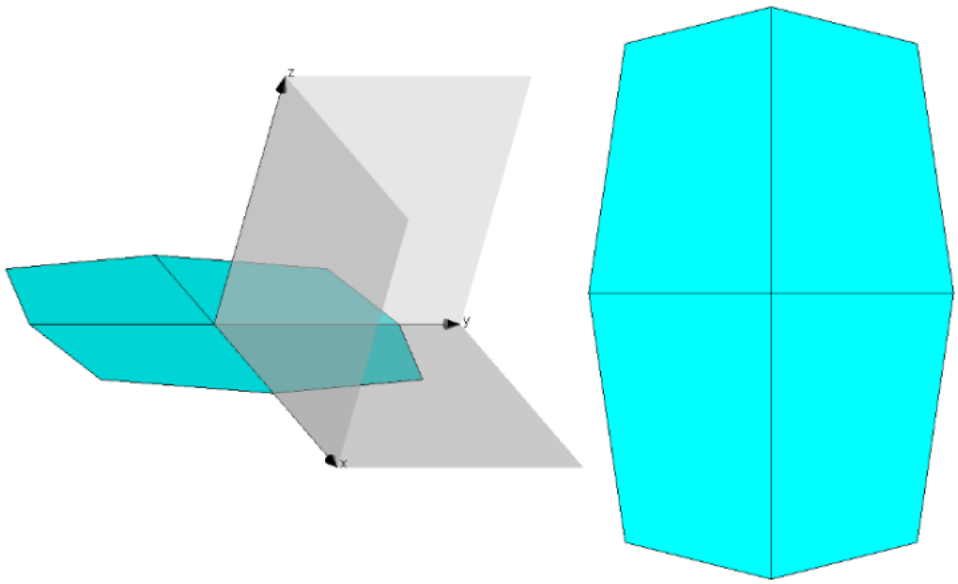


Figure 13. Octagonal footprint derived from the MTPR antenna geometry.

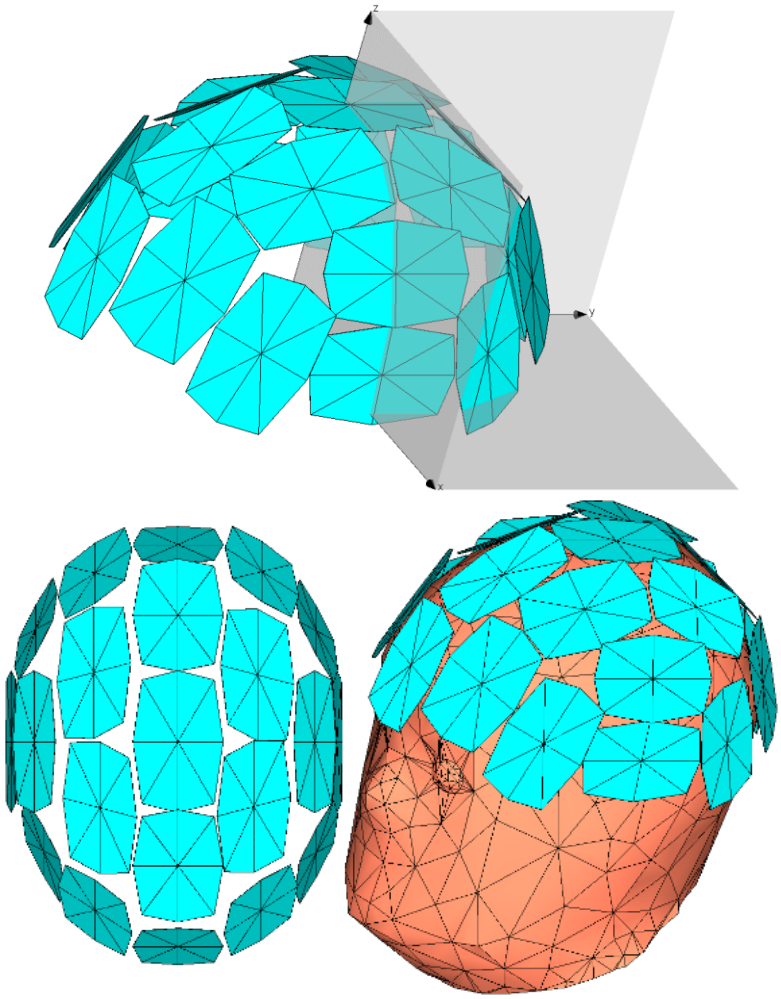


Figure 14. Semi-automatic way to create Helmet around the head.

Once the antenna positions are determined, each octagonal footprint is replaced by an MTPR antenna element. To improve electromagnetic coupling between the antenna array and the head, and to reduce the overall antenna dimensions, each antenna is embedded within a solid matching-medium brick [48]. The matching bricks follow the predefined footprint locations and preserve the compact arrangement established by the placement algorithm.

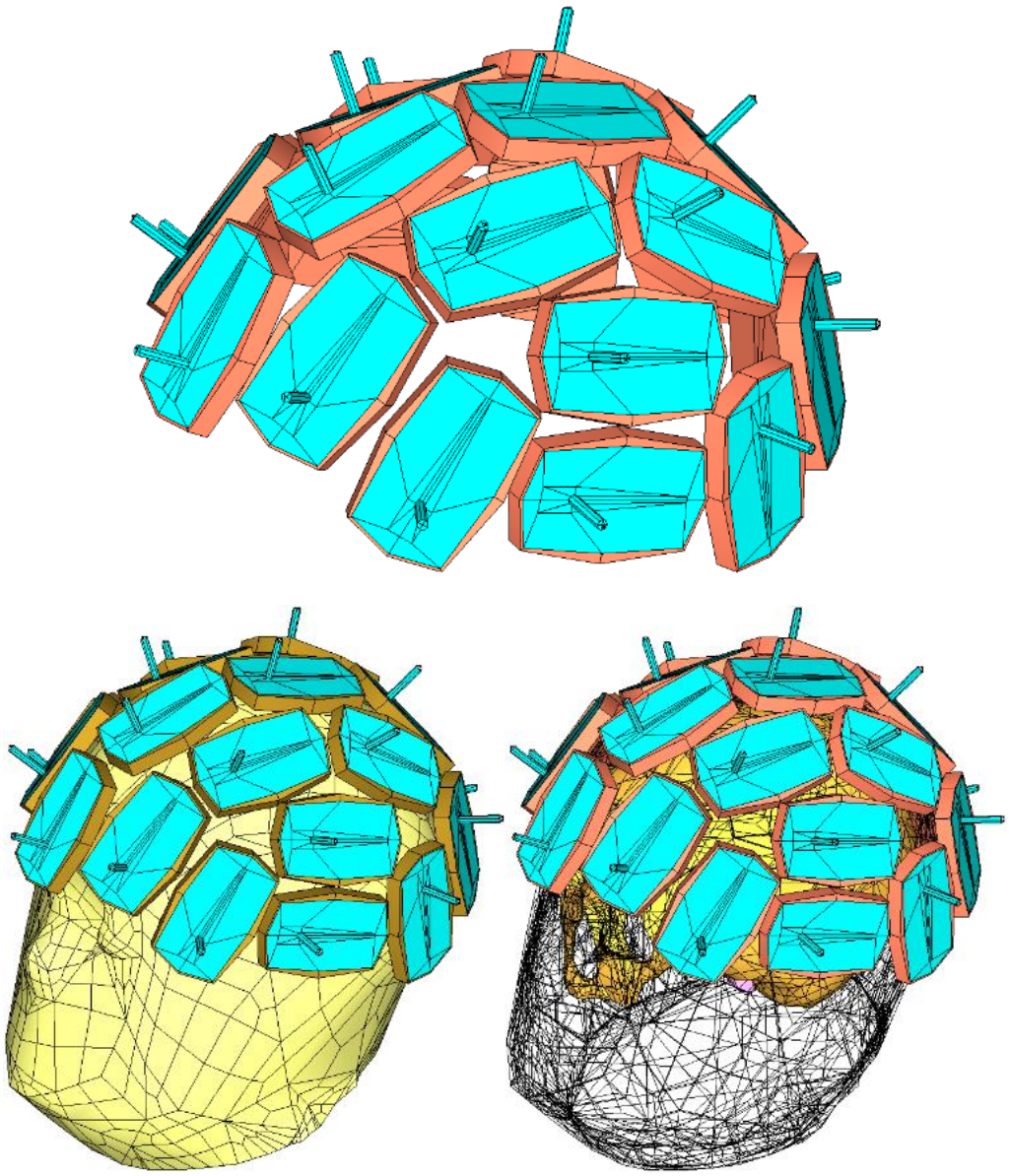


Figure 15. MTPR Antenna Helmet, placed around NEVA head in honey-comb manner.

The antennas are positioned close to the head surface, with the octagonal bases placed tangentially to the phantom boundary at a distance of $d = 3\,\text{mm}$, and their principal axes are oriented to maintain a consistent array configuration. The resulting layout forms a compact, honeycomb-like arrangement that densely covers the upper region of the head, where stroke-related abnormalities are most likely to occur. The semi-automatic procedure is initially developed using the MTPR antenna geometry to define the helmet structure as shown in Figure 15. Once the antenna locations are generated, the MTPR elements are replaced with the optimized MHP antennas while preserving the same footprint and array arrangement. The resulting 21-element helmet configuration is then used throughout this work for the computation of self- and mutual S-parameters in the MMWI scenario. The generated antenna locations are imported into the WIPL-D model to create the final antenna system.

2.4. Reference Head with average tissue properties

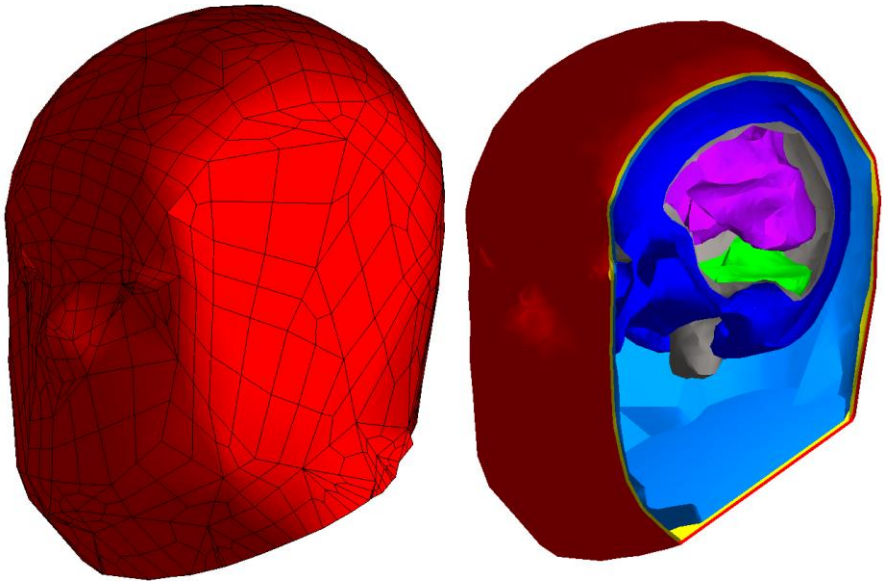
In this section, an approach based on the averaging of the dielectric properties of the tissues within the head is considered, and such model is named as Reference head. By replacing the heterogeneous tissue distribution with equivalent average properties, the complexity of the numerical model can be significantly reduced while preserving its dominant electromagnetic characteristics. This is particularly important for repeated simulations and reconstruction procedures, where detailed anatomical models can become computationally expensive.

The reference head is constructed using the tissue classes most relevant to brain imaging applications, namely skin, fat, muscle, skull, white matter, gray matter, and cerebellum. These tissues are included in the averaging procedure to obtain a reference head that accurately represents the pre-stroke condition. Although the controlled-accuracy studies presented in Chapter 5 employ a simplified tissue model, where white matter, gray matter, and cerebellum are combined into a single brain, a more detailed tissue composition is retained here to improve the accuracy of the equivalent dielectric properties. The equivalent complex permittivity of the reference phantom is determined using appropriate mixing formulations [27] and selected to reproduce the scattering behavior of the original heterogeneous model as closely as possible. Such a reference head serves as an effective initial model for iterative quantitative reconstruction algorithms, such as the distorted Born iterative method [52].

The selected tissue properties are given in Table II. Figure 16. Illustrates the outer boundary of the head and the internal tissue structure.

Table II. TISSUE ELECTRICAL PROPERTIES

Tissue Name	$\boldsymbol{\varepsilon'}$	$\boldsymbol{\varepsilon''}$
Skin	45.7110	15.8437
Fat	11.2943	2.09200
Muscle	45.662	15.9454
Skull Bone	20.5839	6.5422
White Matter	38.5839	11.1790
Grey Matter	52.2823	17.7132
Cerebellum	48.8582	23.5123



(a) (b)

Figure 16. (a) Outer layer of the head, (b) interior layer with tissues of the NEVA model.

Table III. RELATIVE VOLUMES OCCUPIED BY DIFFERENT TISSUES INSIDE THE HEAD

No.	Tissue Name	Volume fraction $v_i / V[\%]$
1	Skin	5.1228
2	Fat	7.3746
3	Muscle	50.8728
4	Skull Bone	10.3113
5	White Matter	5.5376
6	Grey Matter	19.1656
7	Cerebellum	1.6162

Further, to determine the average complex permittivity of the reference head, the volume occupied by each tissue must first be calculated. This is achieved by discretizing the interior of the head into a uniform voxel grid and assigning each voxel to its corresponding tissue region. The volume of each tissue is then obtained by summing up the voxels belonging to that region, as given in TABLE III. Using these volume fractions, the equivalent dielectric properties of the head are evaluated using three averaging approaches: standard averaging, the Lichtenecker mixing formula, and the Looyenga mixing formula [27]. The corresponding formulas are given below.

1. Standard averaging: The average complex permittivity is calculated as a volume-weighted average of the individual tissue permittivities,

$$\varepsilon_{\text{avg}} = \frac{1}{V}\sum_{i=1}^{N} v_i \varepsilon_i \tag{2}$$

where v_i is the volume of the ith tissue, $N$is the total number of tissue types, and $V$is the total head volume.

2. Lichtenecker mixing formula: This method computes the average permittivity using the logarithm of the complex tissue permittivities,

$$\log(\varepsilon_{\text{avg}}) = \sum_{i=1}^{N} \frac{V_i}{V} \log(\varepsilon_i), \tag{3}$$

and is commonly used for mixtures of biological materials such as human blood [52].

3. Looyenga mixing formula: This approach evaluates the average permittivity using fractional powers of the complex tissue permittivities,

$$\varepsilon_{\text{avg}}^{1/\text{M}} = \sum_{i=1}^{N} \frac{V_i}{V} \varepsilon_i^{1/\text{M}}, \tag{4}$$

where M = 1, 2…, and is widely used in the development of liquid tissue-mimicking phantoms [53], [54].

With the use of these averaging techniques, the approximation of the tissue properties is performed to homogenize the dielectric values inside the head. To estimate the approximation, we define a relative mean absolute (RMA) deviation δ, to quantify the difference between the S-parameters of the original heterogeneous head model and those of the corresponding homogeneous reference model.

$$\delta = \frac{\sum_{i=1}^{21\Sigma}\sum_{j=1}^{21\Sigma}\left|S_{ij}^{\text{exact}} - S_{ij}^{hom}\right|}{\sum_{i=1}^{21}\sum_{j=1}^{21}\left|S_{ij}^{\text{exact}}\right|} \tag{5}$$

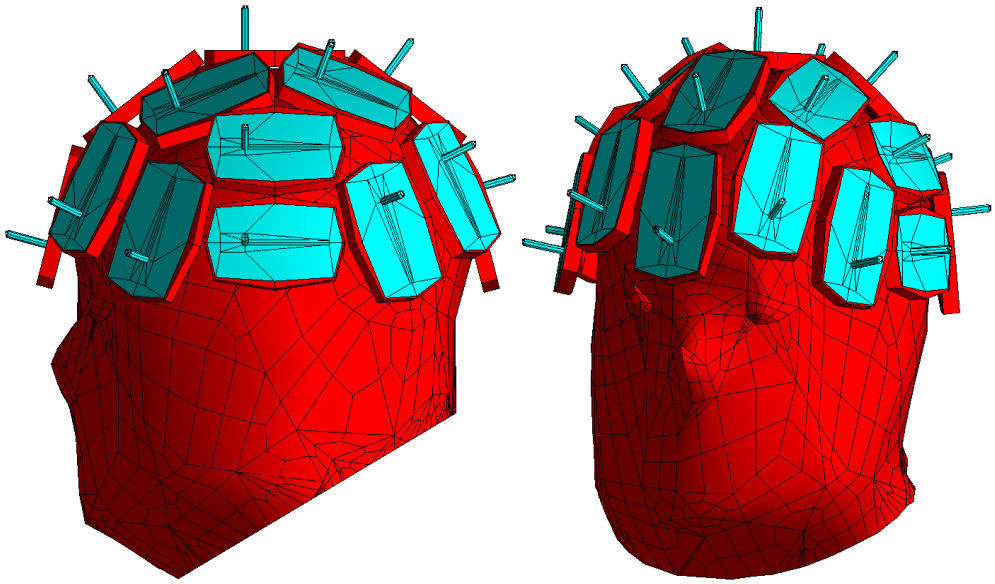
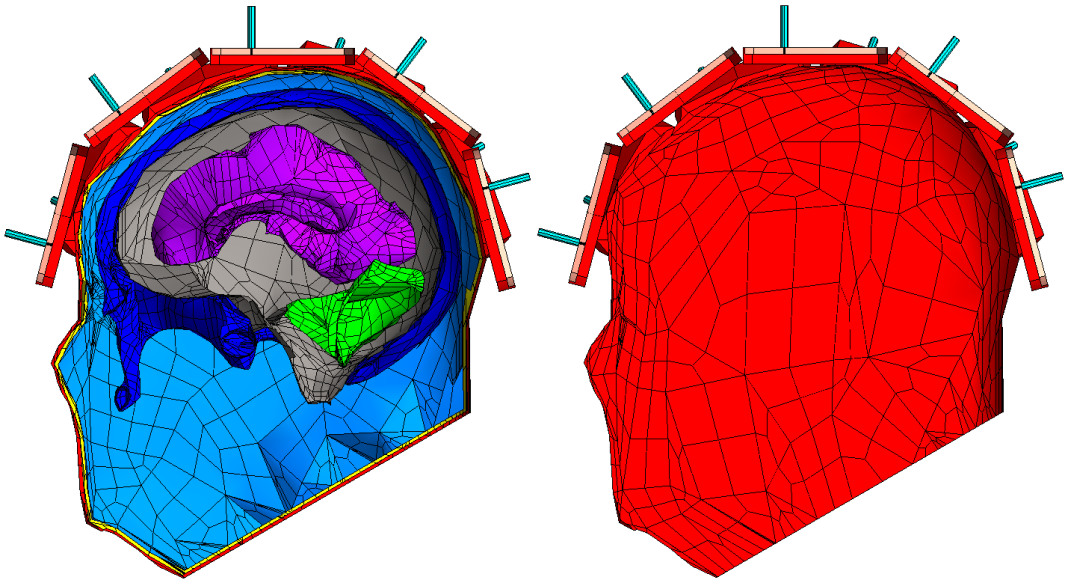


Figure 17. MMWI scenario with MTPR antennas.



(a) (b)

Figure 18. (a) Head phantom with seven tissue layers, (b) Homogeneous head phantom.

The S-parameters are calculated using the MMWI scenario constructed with 21 MTPR antenna helmet with multiple tissue layers and homogenous head, as shown in Figure 17. The cross section of such scenario is shown in Figure 18. The related numerical results are given in Chapter 5.

Chapter 3:
Full-Wave Analysis Method for MMWI Simulations

In this chapter, the full-wave analysis method adopted for MMWI simulations is presented. Since the head tissues are represented as boundary surfaces (STL) initially modeled with triangles, a natural choice for full-wave analysis is the Method of Moments with Surface Integral Equations (MoM/SIE). Although MoM/SIE is often implemented on triangular meshes, quadrilateral patches can improve both accuracy and efficiency especially when higher-order basis functions are employed and mesh quality is controlled [48]. Therefore, we convert the triangular mesh to a quadrilateral one and using a quad-mesh-based MoM/SIE solver, for the electromagnetic analysis [40], [49]. The main solver features relevant to this work are summarized below.

(a) Field Equations and Boundary Integral Formulation

- The unknown surface currents (equivalent electric and magnetic currents) on tissue interfaces are computed by solving the Electric Field Integral Equation (EFIE) and the PMCHWT (Poggio–Miller–Chang–Harrington–Wu–Tsai) combined boundary integral equations.
- EFIE ensures the correct tangential electric field continuity on conducting and dielectric surfaces; PMCHWT enforces tangential field continuity across dielectric–dielectric interfaces, which is essential for multilayer biological structures.
- This surface-only formulation avoids volumetric meshing and is well suited for anatomically segmented phantoms composed of many tissue boundaries.

(b) Geometry Modeling with Quadrilateral (Bilinear) Patches

The boundary surfaces are represented by quadrilateral bilinear patches, each uniquely defined by four vertices (arbitrarily positioned). In a local parametric coordinate system (p, s), the surface position vector $\mathrm{r}(p, s)$can be written in two equivalent forms:

$$\mathbf{r}(p,s) = \frac{1}{4}\sum_{i=1}^{2}\sum_{j=1}^{2}\mathbf{r}_{ij}\ [1+(-1)^{i}p]\,[1+(-1)^{j}s], -1 \le p,s < 1, \tag{6a}$$

$$\mathbf{r}(p,s) = \mathbf{r}_c + \mathbf{r}_p\, p + \mathbf{r}_s\, s + \mathbf{r}_{ps}\, ps, -1 \le p,s < 1, \tag{6b}$$

where $\mathrm{r}_{ij},\ i,j = 1,2$, are the vertex position vectors. By expanding (6a) into (6b), we obtain $\mathrm{r}_c, \mathrm{r}_p, \mathrm{r}_s, \mathrm{r}_{ps}$, which correspond to the patch center, the semi-axes along $p$and s, and the deviation from a rhombus (the bilinear coupling term), respectively. This parametrization captures curvature and mild inflexion, which benefits accuracy with fewer elements compared to lower-order triangles.

(c) Higher-Order Current Expansion on Bilinear Surfaces

The current density is expanded in the local (p, s)coordinate system into components along p and s as shown in Figure 19. For the s-component, a higher-order approximation reads:

$$\mathbf{J}_{s,s}(p,s) = \frac{\mathbf{a}_s}{|\,\mathbf{a}_p \times \mathbf{a}_s\,|} \sum_{j=0}^{n_p-1} \sum_{k=0}^{n_s} a_{jk}\; P_j(p)\, S_k(s), \tag{7a}$$

$$\mathbf{a}_s = \frac{\partial \mathbf{r}}{\partial s}, \mathbf{a}_p = \frac{\partial \mathbf{r}}{\partial p}, \tag{7b, c}$$

where n_p and n_s denote the expansion orders along $p$and s, $a_{jk}$are the unknown coefficients, and $P_j(p)$, $S_k(s)$are the expansion functions orthogonal to and along the current flow, respectively. (An analogous expression holds for the p-component by swapping indices p and s.)

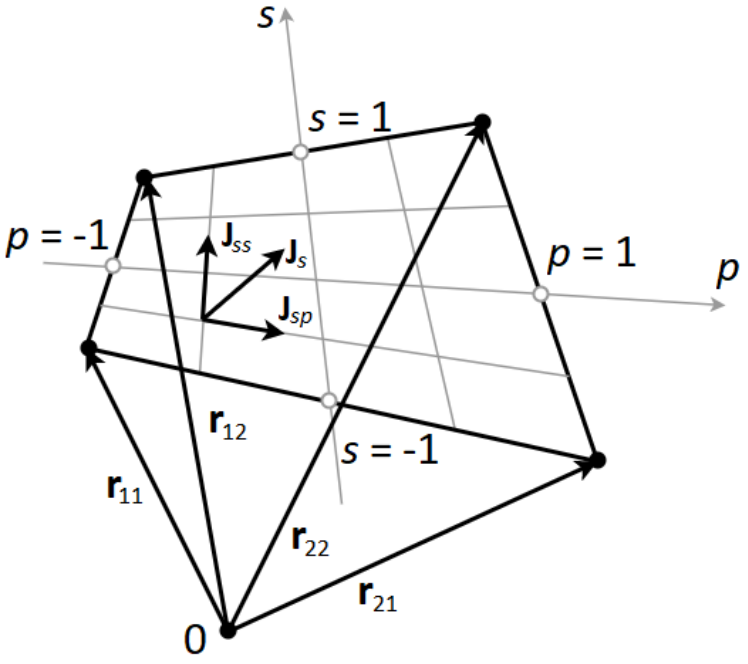


Figure 19. Sketch of a bilinear quadrilateral surface and decomposition of surface current in the local $(\boldsymbol{p}, \boldsymbol{s})$parametric system.

A classic choice of $P$and S functions that preserves normal-current continuity across neighboring patches is:

$$P_j(p) = p^{\,j}, S_k(s) = \begin{cases} 1-s, & k=0, \\ 1+s, & k=1, \\ s^{\,k-1}, & k=2,4,6,\ldots, \\ s^{\,k}-s, & k=3,5,7,\ldots \end{cases} \qquad \text{(8a, b)}$$

- The lowest orders $n_p = 1, n_s = 1$ reduce to rooftop basis functions.
- With classic higher-order bases, the maximum stable order is typically $n_{\max} = 8$.
- By applying maximal orthogonalization to $P$and S, the max-ortho basis significantly extends the usable order (tested up to $n_{\max} = 64$), improving accuracy without sacrificing conditioning [55].

(d) Discretization, Matrix Conditioning, and Solution Strategy

- Galerkin testing procedure turns the boundary integral equations into a linear system.
- Singularity extraction and singularity cancellation are applied to evaluate the MoM system matrix with near machine-precision accuracy [56].
- Matrix equilibration improves conditioning so that, with max-ortho bases, the condition number is nearly independent of expansion order [57].
- The linear system is solved via a direct method (LU decomposition), ensuring that the solution accuracy is governed primarily by the expressive power of the basis functions in modeling the true current distribution.

Accuracy Control via Expansion Orders and Patch Size

Patch electrical sizes guide the selection of expansion orders. For each patch, the maximum physical spans along the local p- and s-axes are:

$$\ell_{p\max} = \max(|\,\mathbf{r}_{21} - \mathbf{r}_{11}\,|\,,\ |\,\mathbf{r}_{22} - \mathbf{r}_{12}\,|), \qquad \text{(9a)}$$

$$\ell_{s\max} = \max(|\,\mathbf{r}_{12} - \mathbf{r}_{11}\,|\,,\ |\,\mathbf{r}_{22} - \mathbf{r}_{21}\,|). \qquad \text{(9b)}$$

$$n_p = 1 + \left\lfloor \frac{3\,\ell_{p\max}}{\lambda_{\mathrm{ref}}/6} \right\rfloor, n_s = 1 + \left\lfloor \frac{3\,\ell_{s\max}}{\lambda_{\mathrm{ref}}/6} \right\rfloor, \qquad \text{(9c, d)}$$

To decouple operating frequency f_0 from current-expansion density, EM-solver uses a reference frequency f_{ref} with wavelength λ_{ref}. The expansion orders are set as

where $\lfloor \bullet \rfloor$ denotes the floor. It follows that if $\ell_{p\max}, \ell_{s\max} < \lambda_{\mathrm{ref}}/6$, then $n_p = n_s = 1$ (i.e., rooftop). Each further increase of $\ell_{p\max}$ or $\ell_{s\max}$ by $\lambda_{\mathrm{ref}}/3$ increments the corresponding order by one. By default, $f_{\mathrm{ref}} = f_0$.

The maximum patch size (MPS) For classic higher-order bases (limited to $n_{\max} = 8$), the maximum recommended electrical size per patch is MPS = 2.5 λ_{ref}. If a patch exceeds this size, it is automatically subdivided. By default, MPS = 2 λ_{ref} to fully exploit classic higher-order bases. To restrict the model to rooftop functions only, set MPS = $\lambda_{\mathrm{ref}}/6$.

- Increasing unknowns generally improves accuracy.
    - With higher-order bases, raise f_{ref} to increase expansion orders.
    - With rooftop bases, decrease MPS to refine the mesh.

This strategy offers clear and controllable accuracy, cost trade-off, aligning basis richness and patch sizing with the fidelity requirements of MMWI simulations.

(Chapter 4: Controlled-Deviation Decimation and High-Fidelity Mesh Construction from STL Models

The anatomical head phantom introduced in Chapter 2 is represented by a high-resolution STL model composed of triangular surface elements. Although such models provide accurate anatomical representation of tissues and organs, they often contain a very large number of mesh elements, leading to increased memory requirements and long simulation times. This becomes particularly important in MMWI applications, where multiple forward simulations are required for antenna design, algorithm validation, parameter studies, and self-convergence analysis.

To make the simulations computationally efficient while preserving the anatomical features relevant to electromagnetic propagation, the initial STL model must be processed before it can be used for full-wave analysis. The processing workflow should reduce mesh complexity, control geometric deviation from the original anatomy, and generate high-quality quadrilateral elements suitable for reliable EM modeling. At the same time, mesh-processing operations must preserve tissue boundaries, maintain topological consistency, and avoid introducing geometric artifacts that could affect the computed electromagnetic response.

Obtaining a decimated quadrilateral mesh from an STL human phantom while preserving the essential anatomical and electromagnetic features is a challenging task. The problem is commonly addressed using a combination of techniques originating from computational geometry, CAD/CAE meshing, and computer graphics [58]-[65]. In MMWI applications, these techniques must be adapted to satisfy strict requirements regarding geometric accuracy, mesh quality, and numerical stability.

To address these requirements, the proposed mesh-generation framework consists of the following three steps:

- Controlled decimation of the initial triangular mesh, where the number of triangles is reduced while keeping the geometric deviation from the original STL model within a prescribed tolerance.
- Triangle-to-quadrilateral mesh conversion, in which the decimated triangular mesh is transformed into a quadrilateral representation suitable for efficient higher-order EM modeling.
- Quadrilateral mesh refinement, where the generated quadrilateral elements are adjusted to improve mesh quality and maximize conformity with the original STL geometry.

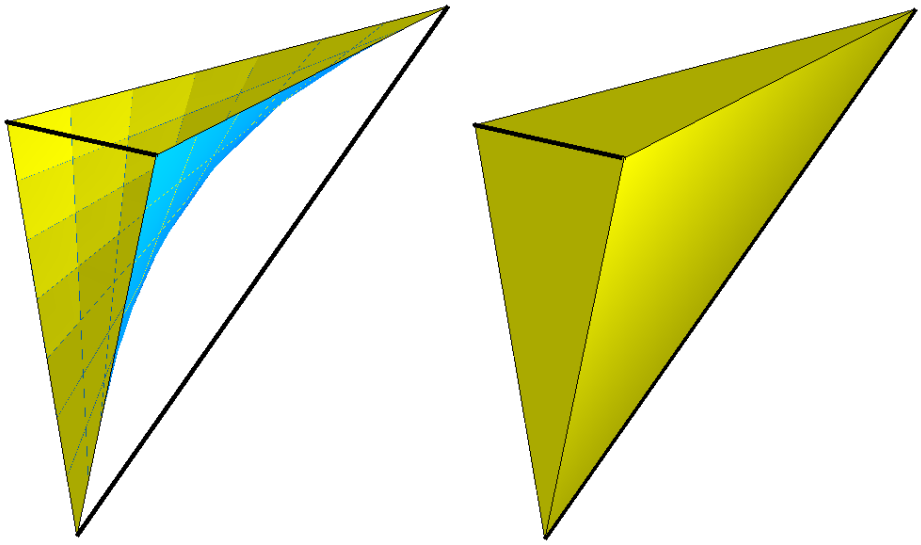
The resulting workflow provides a computationally efficient quadrilateral mesh while preserving the geometric fidelity required for reliable MMWI simulations. The individual stages of the procedure are described in the following sections.

4.1. Avoiding Irregularities in Quad Mesh

Various irregularities can arise both in the original STL model and during the three-step mesh-generation procedure. Therefore, the validity of the mesh must be verified at every stage before any modification is accepted. For triangular meshes, verification for geometric defects such as surface intersections, overlapping triangles, and edge crossings can be performed efficiently using analytical relationships between nodes, lines, and planes. Since realistic anatomical models may contain thousands of elements,

the validation process is restricted to the modified region and its immediate neighborhood, significantly reducing the computational cost while still ensuring mesh integrity.

Validation becomes more challenging after the conversion to quadrilateral meshes. Unlike triangular elements, quadrilateral surfaces are represented as bilinear patches, making intersection detection more complex and computationally expensive. To simplify this process, the quadrilaterals in the modified region are temporarily converted into triangles and then validated using the same procedures developed for triangular meshes. For planar quadrilaterals, the element is divided into two triangles along the shorter diagonal. In the case of an inflexed (non-planar) quadrilateral, shown in Figure 20(a), a tetrahedron is constructed using the same four corner vertices. The four triangular faces of this tetrahedron, illustrated in Figure 20(b), are then used for validation, with the original inflexed quadrilateral considered to be inscribed within the tetrahedron. This approach provides an efficient and reliable way to detect geometric irregularities while preserving accuracy.



(a) (b)

Figure 20. (a) Inflexed quadrilateral with both diagonals highlighted; (b) corresponding tetrahedral representation.

4.2. Controlling Deviation from Initial STL Model

The primary objective of mesh decimation is to reduce the number of surface elements while preserving the geometric characteristics of the original anatomical model. For MMWI applications, maintaining geometric accuracy is particularly important because small changes at tissue interfaces can influence the computed electromagnetic fields and S-parameters. Therefore, the amount of geometric modification introduced during mesh processing must be carefully controlled [58] - [64].

To evaluate the accuracy of a modified mesh, two deviation metrics are used:

$$\delta_{\max} = \max\{\delta_i \mid i = 1, \ldots, N\}, \delta_{\mathrm{RMS}} = \sqrt{\frac{1}{N}\sum_{i=1}^{N} \delta_i^2}, \qquad (10a, b)$$

where δ_i represents the minimum Euclidean distance between the i-th node of the original STL mesh and the nearest element of the modified mesh, and $N$is the total number of nodes in the original model. The maximum deviation, δ_{max}, indicates the largest local change introduced during mesh processing, while the RMS deviation, δ_{RMS}, represents the average geometric deviation over the entire surface. Together, these parameters provide a quantitative measure of how closely the modified mesh matches the original STL geometry [58] - [64].

To ensure that mesh simplification does not compromise the anatomical and electromagnetic characteristics of the phantom, a maximum allowable deviation is imposed: $\delta_{\max} < \sigma_{\max}$, where $\sigma_{max}$is a user-defined tolerance. The selected value of σ_{max} depends on the resolution of the original CT/MRI data, the operating frequency of the MMWI system, and the required modeling accuracy [58] - [64]. In practice, σ_{max} must be sufficiently small to preserve important dielectric boundaries, while still allowing a meaningful reduction in the number of mesh elements. The RMS deviation is also monitored to ensure that the overall shape of the model remains close to the original geometry.

Throughout the proposed workflow, all decimation and triangle-to-quadrilateral conversion operations are performed under these deviation constraints. A final mesh-refinement stage is then applied to improve geometric conformity while maintaining acceptable element quality. This approach provides a clear and quantitative way to control geometric accuracy while achieving the computational efficiency required for MMWI simulations.

4.3. Quality Factors for Quadrilateral Elements

To ensure both accuracy and efficiency in 3D EM simulations, we evaluate the geometric quality of quadrilateral surface elements using two complementary measures and a combined score.

Accuracy-oriented quality factor: The shape quality factor related to modeling accuracy is defined as

$$Q_{\mathrm{acc}} = \frac{1 - |\alpha| - |\beta|}{\sqrt{\left(1 + |\alpha| + |\beta|\right)^2 + \dfrac{|\mathbf{r}_p|^2 + 2|\mathbf{r}_p \cdot \mathbf{r}_s| + |\mathbf{r}_s|^2}{|\mathbf{r}_p \times \mathbf{r}_s|}\gamma^2}}, \qquad (11a)$$

with the decomposition

$$\mathbf{r}_{ps} = \alpha\,\mathbf{r}_p + \beta\,\mathbf{r}_s + \gamma\,\frac{\mathbf{r}_p \times \mathbf{r}_s}{\sqrt{|\ \mathbf{r}_p \times \mathbf{r}_s\ |}}, \tag{11b}$$

where the coefficients α, β, and $\gamma$are obtained by expressing the vector r_{ps}along the directions r_p, r_s, and $\mathrm{r}_p \times \mathrm{r}_s$, respectively. Equation (11) generalizes the flat-element quality factor proposed in [48], [65] to the inflexed (non-planar) case; it reduces to the flat-quad form by setting $\gamma = 0$. Empirically, increased inflexion (larger γ) lowers Q_{acc}. When a quadrilateral becomes concave, i.e., $|\ \alpha\ | + |\ \beta\ | > 1$, the factor turns negative, signaling an undesirable element for accurate field representation. The maximum value $Q_{\mathrm{acc}} = 1$occurs at $\alpha = \beta = \gamma = 0$, which corresponds to squares, rectangles, and rhombuses (planar and well-shaped).

Efficiency-oriented quality factor: The shape quality factor related to computational efficiency is defined as the ratio of the quadrilateral's effective area (evaluated with $\gamma = 0$) to a reference rectangular area associated with the maximum spans along the local p- and s-coordinates (eq (9[])):

$$Q_{\mathrm{eff}} = \frac{4\ |\ \mathbf{r}_p \times \mathbf{r}_s\ |}{\ell_{s\max}\,\ell_{p\max}}. \tag{12}$$

Here, the value of one is attained for squares and rectangles. For rhombuses, Q_{eff} decreases as the shape thins (area diminishes relative to the bounding spans). Notably, even elongated rectangles retain the maximum value, which is appropriate because lower-order expansion can be placed along the short edge, while higher-order basis functions can be applied along the long edge, maintaining numerical efficiency without sacrificing representational power.

Combined quality factor: To balance accuracy and efficiency in a single indicator, we define the total shape quality as

$$Q = \begin{cases} \sqrt{Q_{\mathrm{eff}}\,Q_{\mathrm{acc}}}, & Q_{\mathrm{acc}} > 0, \\ Q_{\mathrm{acc}}, & \text{otherwise.} \end{cases} \tag{13}$$

this factor incorporates both $Q_{acc}$and Q_{eff}, allowing geometric accuracy and computational efficiency to be assessed simultaneously. Elements exhibiting excessive inflexion or concavity are penalized through a reduced accuracy factor, while elements that are both geometrically regular and

computationally efficient receive higher scores. Consequently, monitoring the combined quality factor during quadrilateral mesh generation and refinement helps maintain numerical stability, improve accuracy of the EM solution, and control the number of unknowns. This balance between mesh quality and computational cost is essential for reliable MMWI forward simulations [48], [65].

4.4. Initial Triangular Mesh Decimation

The decimation of the initial triangular mesh is carried out using the vertex-collapse technique [58], [59]. This approach is preferred for its relative simplicity and its ability to satisfy mesh-quality constraints more reliably than alternatives such as edge collapse [60], [61], triangle collapse [62], vertex clustering, or grid-map methods [49], [63]. In our workflow, vertex collapse is tailored to preserve anatomical fidelity under a maximum allowed deviation constraint while preparing the surface for quality-controlled quad remeshing.

The vertex-collapse operation is validated and (when acceptable) executed through the following five steps, adapted to the specific requirements of accuracy and topological correctness:

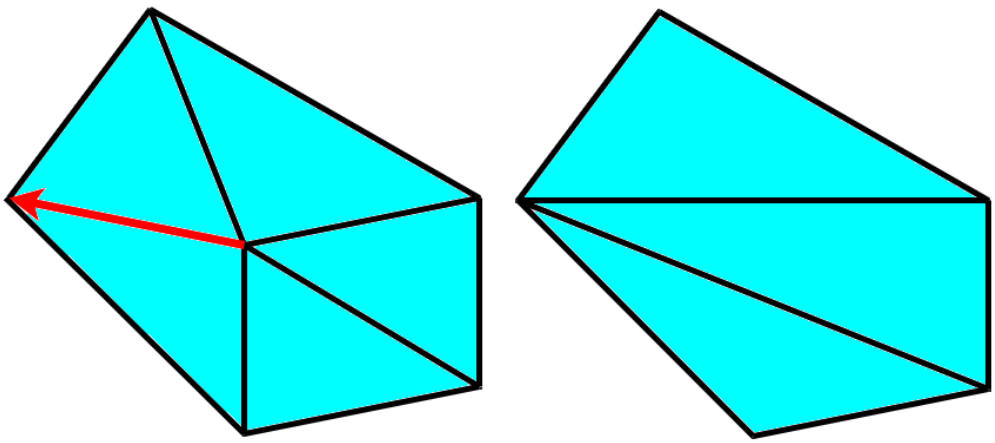
1. Polygon formation around the candidate vertex: Construct the (minimum) 1-ring polygon comprising all triangles incident to the vertex under test (Figure 21(a)). This defines the local neighborhood subject to modification.

2. Merging to a polygon vertex: Translate the vertex toward a selected polygon vertex until the two vertices coincide (Figure 21(b)). This removes the tested node and eliminates two triangles from the mesh, locally simplifying the surface.

3. Local validity check: Apply geometric validation to the modified neighborhood to ensure that the operation does not introduce self-intersections, overlaps, or other irregularities with respect to adjacent triangles in the vicinity.

4. Deviation measurement: If the local validity test is passed, compute the maximum deviation of the modified configuration with respect to the original local surface (i.e., the max of point-to-surface minimum distances for the affected nodes/triangles).

5. Deviation thresholding and approval: If the measured maximum deviation is below the specified tolerance $\sigma_{\max}$, approve and commit the vertex collapse. Otherwise, reject the operation.



(a) (b)

Figure 21. Decimation of a minimal polygon using the vertex-collapse method: (a) before and (b) after vertex collapse.

If either Step 3 (validity) or Step 5 (deviation threshold) fails, the vertex collapse for that node is skipped and the algorithm proceeds to the next candidate.

Figure 22 illustrates the skull and brain phantoms after applying different decimation levels: (a) no decimation, (b) $\sigma_{\max} = 1$ mm, (c) $\sigma_{\max} = 2$ mm, and (d) $\sigma_{\max} = 3$ mm, at $\sigma_{\max} = 3$ mm, the global shape remains visually consistent with the initial model, indicating that the bounded-deviation criterion preserves anatomical fidelity while reducing element count.

The choice of the merge target (the polygon vertex with which the candidate vertex is fused) has a pronounced effect on the quality of the subsequent quad mesh. To increase Q_{eff} for quads formed from collapsed triangle neighborhoods, we prefer shorter triangle edges in the local configuration. Accordingly, among all polygon vertices, we select the one that minimizes the sum of distances to the non-neighboring polygon nodes. This heuristic promotes compact local edge lengths, which later supports efficient higher-order basis placement and improves element shape factors.

Vertices are tested in the listed order of the initial STL file. After a full pass, if at least one collapse has been approved, the procedure repeats (typically 3 - 5 iterations for complex models) until no further collapses satisfy the constraints. This iterative process yields a decimated STL mesh that does not exceed the prescribed maximum deviation $\sigma_{\max}$ from the original triangulation.

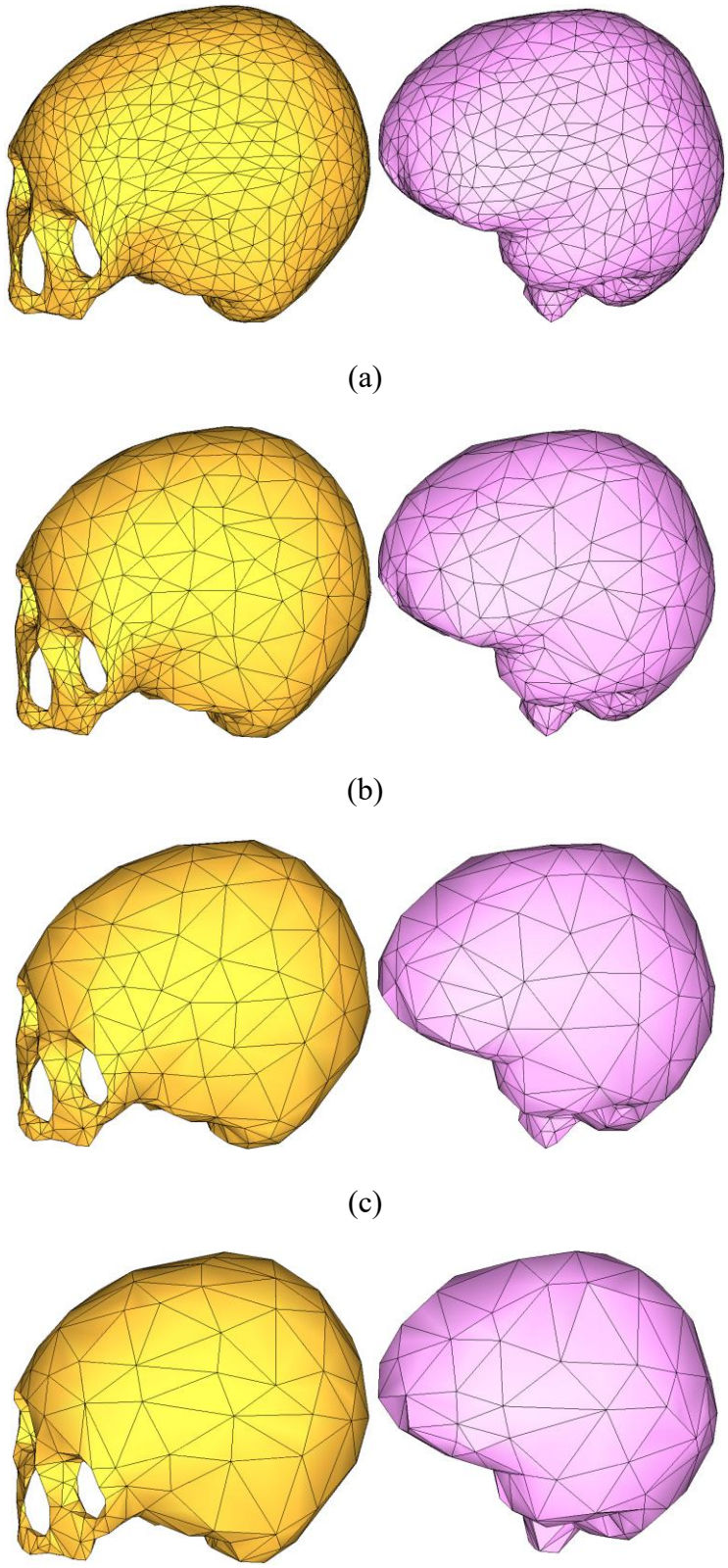


Figure 22. Skull and brain phantoms generated at different decimation levels: (a) no decimation, (b) σ_{max} = 1 mm, (c) σ_{max} = 2 mm, and (d) σ_{max} = 3 mm.

Table IV. RMS DEVIATION AND NUMBER OF TRIANGLES OBTAINED WITH DIFFERENT LEVELS OF MAXIMUM ALLOWED DEVIATION $\boldsymbol{\sigma_{max}}$.

Maximum allowed deviation [mm]	RMS deviation [mm]	Number of triangles
0.0	0.000	8362
0.5	0.092	7250
1.0	0.279	5592
1.5	0.492	4436
2.0	0.693	3652
2.5	0.892	3160
3.0	1.058	2800
3.5	1.271	2514
4.0	1.396	2322
4.5	1.616	2172
5.0	1.699	2080

We demonstrate the effectiveness of the proposed decimation method using two examples. In the first example, we decimate the skull and brain surfaces. As shown in Figure 22, the decimated geometries corresponding to $\sigma_{\max} = 1$ mm, 2 mm, and 3 mm closely retain the overall shape relative to the initial surface (no decimation). In the second example, we decimate the five-tissue head phantom described in Section 2.1. Table IV reports the RMS deviation and the number of triangles obtained for a range of $\sigma_{\max}$ values. Two trends are evident:

- The RMS deviation is approximately one-third of the maximum allowed deviation, i.e., $\delta_{\mathrm{RMS}} \approx \sigma_{\max}/3$.
- The triangle count can be reduced by 3 - 4 times while maintaining acceptable geometric fidelity.

This bounded-deviation, validation-driven vertex-collapse strategy thus achieves substantial element reduction with controlled shape error, laying a solid foundation for triangle-to-quad conversion and quality-factor-guided refinement [58]– [64].

4.5. Triangle-to-Quad Mesh Conversion

To obtain a pure quadrilateral mesh from the decimated STL surface, we employ a two-step procedure designed to preserve geometric fidelity while producing elements with good shape quality factors.

Step 1- Merging pairs of triangles (tri→quad): Triangles in the decimated STL mesh are examined in their listed order and tested for merging with a neighboring triangle (i.e., one sharing a common edge). To improve the efficiency-oriented quality factor Q_{eff} based on (12), merging is attempted along the longest edge that is eligible (Figure 21(a)). A merger is approved only if all the following conditions are satisfied:

- Edge connectivity: The candidate edge is neither free nor multiply connected, ensuring topological consistency.
- Material consistency: The neighboring triangle has the same material assignment and has not been used in a previous merger, so that tissue boundaries are preserved.
- Element shape quality: The resulting quadrilateral is at least convex (i.e., total quality $Q > 0$), which avoids concave or severely distorted quads that degrade EM accuracy.
- Quasi-planarity: The two triangles are nearly coplanar, with the angle between their unit normals less than 5°. This constraint protects sharp edges and regions of rapid curvature change, where aggressive merging could blur critical anatomical features.

Because these constraints are conservative and feature-preserving, approximately 20–30% of triangles typically remain unmerged; we refer to these as orphan triangles. This behavior is expected and acceptable, as it prevents topological errors and maintains local geometric detail [58].

Step 2- Creation of a pure quad mesh (subdivision): To remove all remaining triangles and achieve a full quadrilateral mesh, we apply a local subdivision scheme (Figures. 23(a) – (d)):

- Orphan triangles are each subdivided into three quadrilaterals, following the standard construction in [49] (Figure 23(b)).
- Quadrilaterals created in Step 1 are subdivided into four quads to ensure continuity and regularity in the final mesh (Figure 23(c)). This simple, structured subdivision is a special case of the broader Catmull–Clark framework and is often referred to by that name in the literature [66].

This two-stage approach can also be applied directly to a decimated triangular surface (skipping Step 1), but doing so inflates the quad count to roughly three times the number of input triangles. By first merging as many triangle pairs as possible (Step 1) and then subdividing (Step 2), the final quad count is typically limited to about 2.2 - 2.3 times the number of triangles in the decimated STL mesh, significantly more efficient.

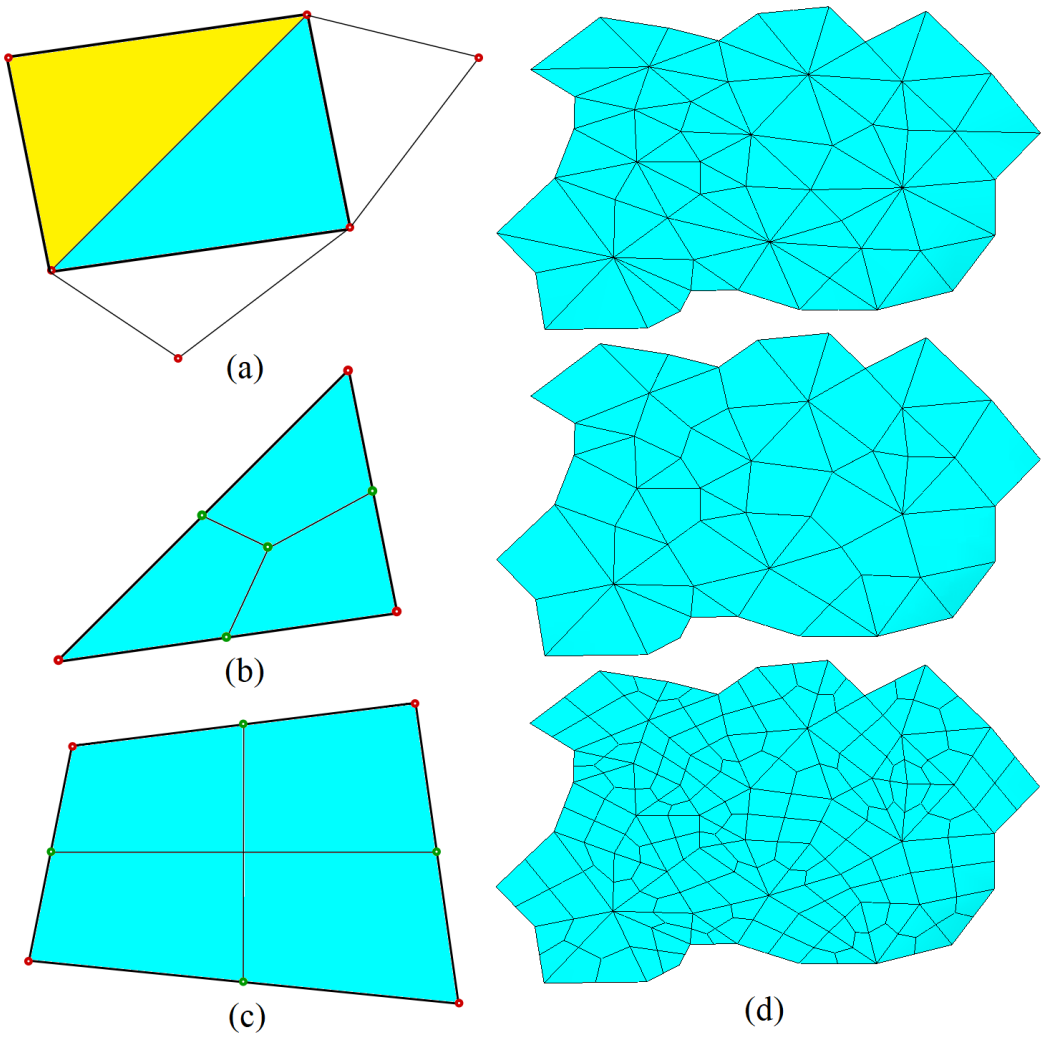


Figure 23. Triangle-to-quadrilateral mesh conversion procedure: (a) merging of adjacent triangles, (b) subdivision of a triangular element into three quadrilaterals, (c) subdivision of a quadrilateral into four quadrilaterals, and (d) illustration of the complete two-step conversion process.

In principle, orphan triangles on closed surfaces can be eliminated (at least topologically) by allowing them to "crawl" across the mesh and pair up for merging into quads [60], [67]. However, when the strict merging constraints above are enforced (material consistency, convexity, and quasi-planarity), such global reconfiguration becomes computationally complex and may jeopardize local feature preservation. For this reason, we adopt the proposed two-step method without triangle crawling. The overall workflow is summarized in Figure 23(d), and it yields quadrilateral meshes that (i) consider material interfaces, (ii) maintain bounded deviation from the STL model, and (iii) exhibit quality factors conducive to accurate and efficient MoM/SIE-based 3D EM simulation [49], [66] - [68].

4.6. Quadrilateral Mesh Refinement for Better Approximation of the STL Model

Following the two-step tri-to-quad conversion, we introduce a local refinement stage to improve the geometric fit of the quadrilateral mesh to the original STL surface while preserving element quality. In the second step of the conversion, new nodes are inserted at the midpoints of edges and at the centers of triangles and quadrilaterals. Each of these nodes are then incrementally displaced toward the nearest point on the original STL model (Figure 24(a)). After every incremental move, we recompute the shape quality factors for the affected quadrilaterals. If any newly evaluated quality factor drops below half of its initial value (prior to the move), the node is reverted to its previous position to prevent degradation of mesh accuracy. Otherwise, the iterative adjustment proceeds until the intersection (contact) with the initial STL surface is achieved (Figure 24(b)). This conservative, feedback-controlled process ensures that the refined quad mesh converges toward the STL geometry without producing ill-shaped or concave elements that could compromise 3D EM mesh quality.

We evaluate the effectiveness of the refinement step, together with the full three-stage meshing pipeline (decimation, tri-to-quad conversion, and refinement), using two representative examples. In the first example, the procedure is applied to the decimated skull and brain models from Figure 22, and the resulting quad meshes are shown in Figure 25 for multiple decimation levels. Across these settings, the overall shapes remain visually indistinguishable from the original STL geometries, indicating that the bounded-deviation strategy and subsequent refinement successfully preserve salient anatomical features while reducing the number of elements.

In the second example, we apply the same procedure to the five-tissue head phantom. Table III reports the RMS deviation and the number of quadrilateral plates as functions of the maximum allowed deviation, σ_{max}. Two practical trends are observed:

(a) the RMS deviation is approximately one sixth of the maximum deviation, i.e., $\delta_{RMS} \approx \sigma_{max}/6$; and

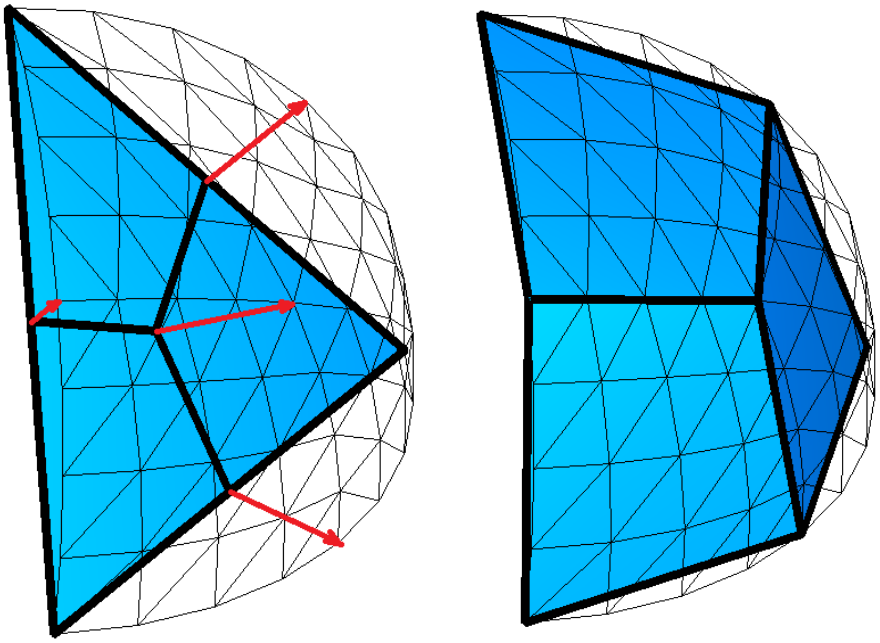
(b) the total number of quads can be reduced by a factor of 3–4 while maintaining high geometric fidelity.

To better understand the relationship between STL and quad-mesh representations, the data from Tables IV and V are presented in Figure 26. These results show that, for the same RMS deviation, the quad mesh contains a slightly higher number of elements than the triangular STL mesh. This is expected, as quads enforce additional connectivity constraints compared to triangles, but the increase remains modest and does not compromise the benefits of controlled decimation and refinement.

In the subsequent analyses, we adopt $\sigma_{\max} = 3$ mm as the default deviation value. This choice reflects a practical balance between computational efficiency and geometric fidelity, consistent with the sensitivity requirements of MMWI forward modeling. To quantify how decimation (and the associated deviation thresholds) impacts the accuracy of 3D EM data used for imaging, we introduce a well-defined self-convergence test in the next section.

Table V. NUMBER OF QUADS AND RELATIVE RMS DEVIATION

Maximum allowed deviation [mm]	RMS deviation [mm]	Number of plates after meshing
0.0	0.000	18664
0.5	0.061	16248
1.0	0.158	12852
1.5	0.251	10318
2.0	0.351	8654
2.5	0.430	7616
3.0	0.506	6848
3.5	0.584	6234
4.0	0.651	5836
4.5	0.735	5506
5.0	0.769	5276



(a) (b)

Figure 24 . Quadrilateral mesh refinement for improved agreement with the original STL geometry: (a) displacement of newly generated nodes toward the nearest locations on the STL surface (red arrows), and (b) refined quadrilateral mesh after node adjustment.

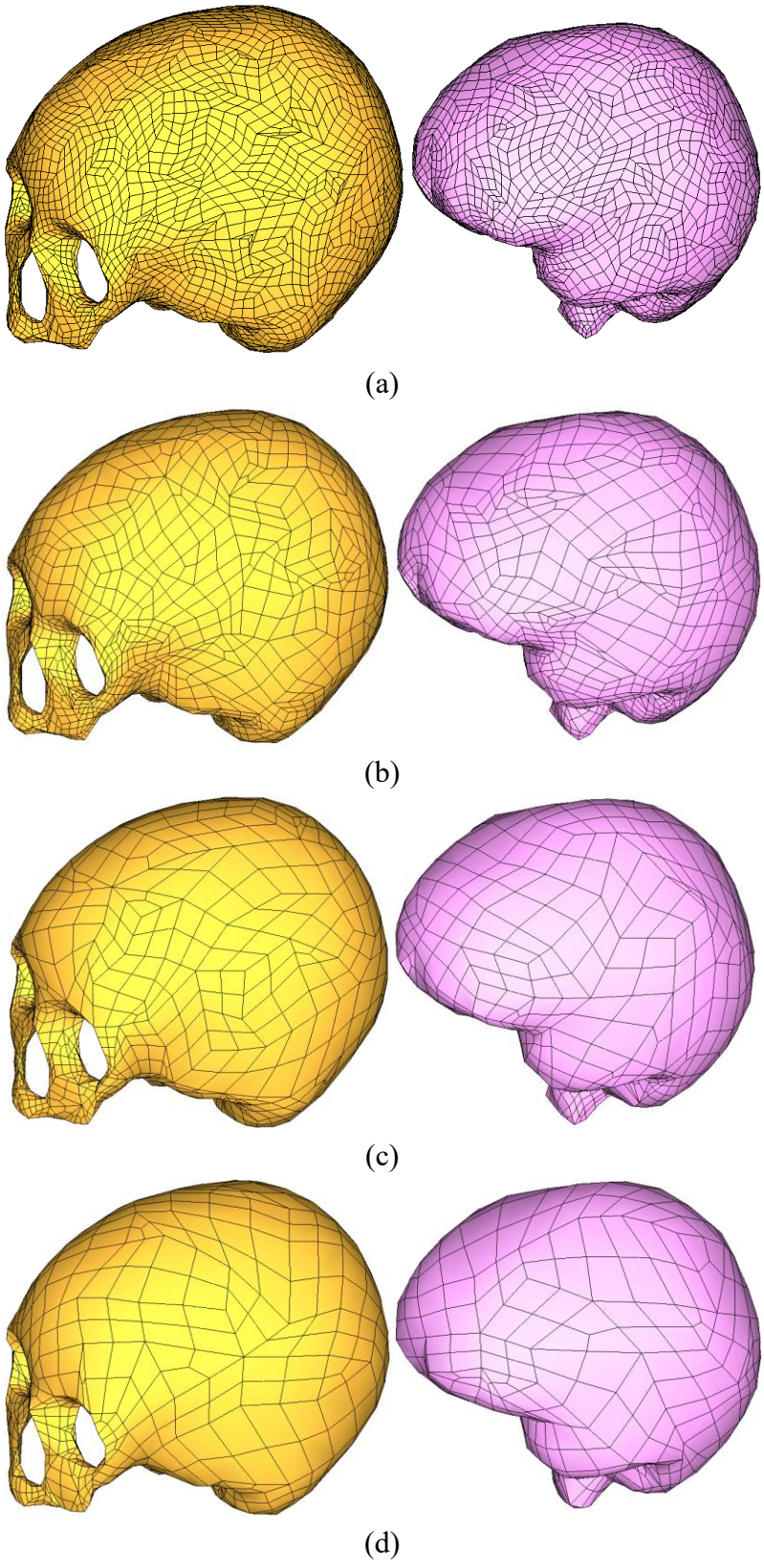


Figure 25. Quadrilateral meshes of the skull and brain obtained for different maximum allowed deviations: (a) no decimation, (b) σ_{max} = 1 mm, (c) σ_{max} = 2 mm, and (d) σ_{max} = 3 mm.

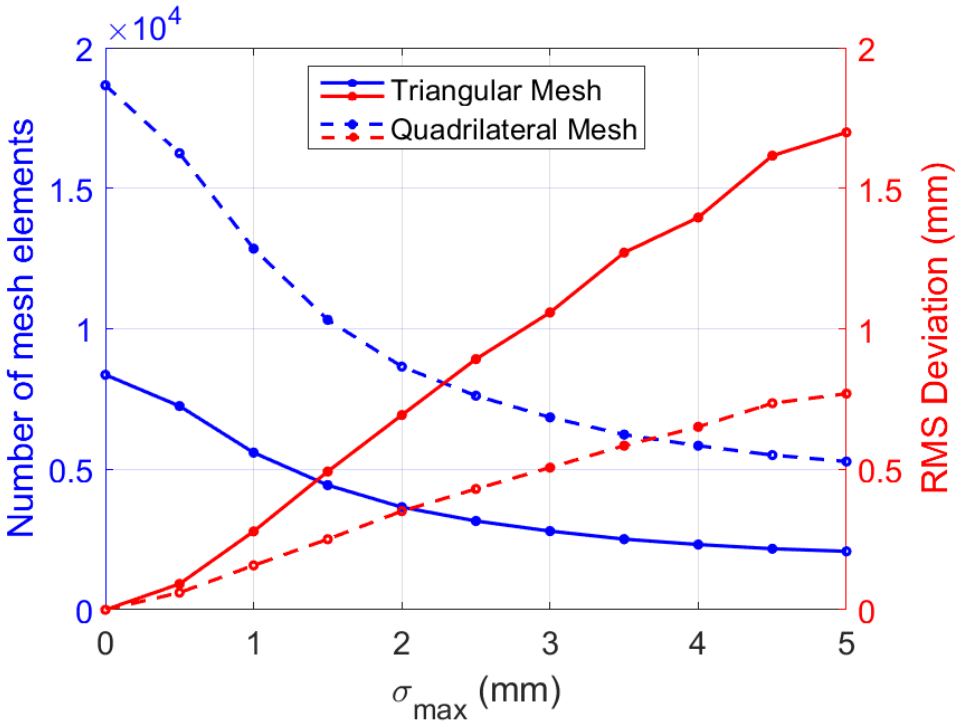


Figure 26. Number of mesh elements and RMS deviation for triangular and quadrilateral meshes.

Chapter 5:
Numerical Results and Validation of Accuracy-Controlled 3D EM Modeling

We first investigated the effect of replacing the complex seven-tissue head phantom with a homogeneous phantom on the electromagnetic modeling results. The equivalent dielectric properties of the homogeneous phantom were determined by different mixing techniques, as specified in Section 2.4. As an accuracy metric we used the relative mean absolute (RMA) error defined in equation (5) of Section 2.4. The results are reported in Table VI.

Table VI. AVERAGE DIELECTRIC VALUES WITH RELATIVE MEAN ABSOLUTE DEVIATION

Averaging Method	ε'	ε''	Relative Mean Absolute [%]
Standard Averaging	41.47	14.15	16.36
Looyenga (M = 2)	40.24	13.56	14.94
Looyenga (M = 3)	39.76	13.32	14.42
Lichtenecker	38.66	12.76	13.33

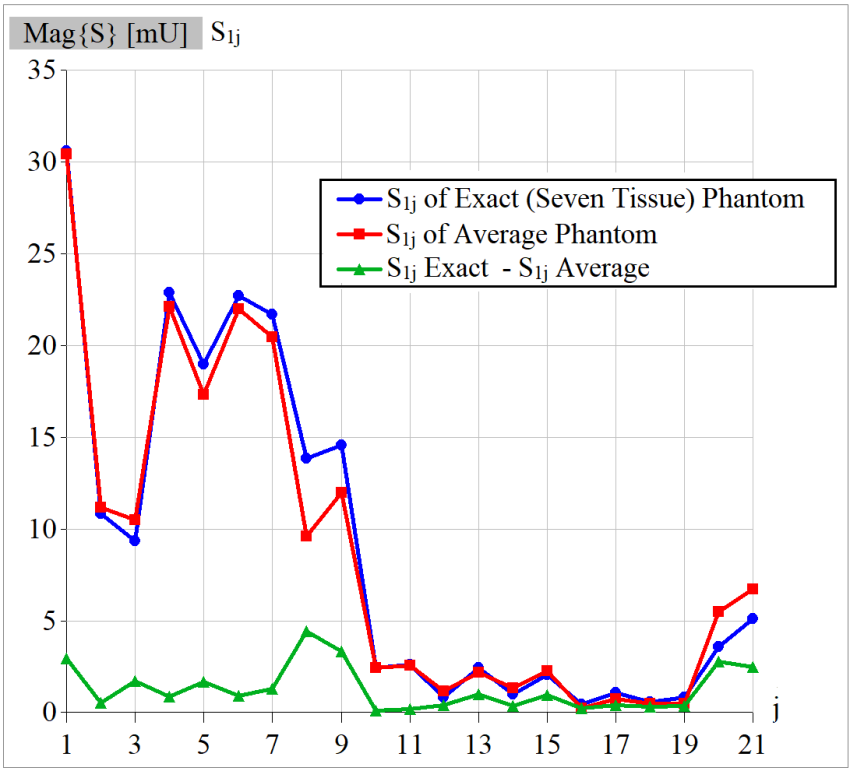
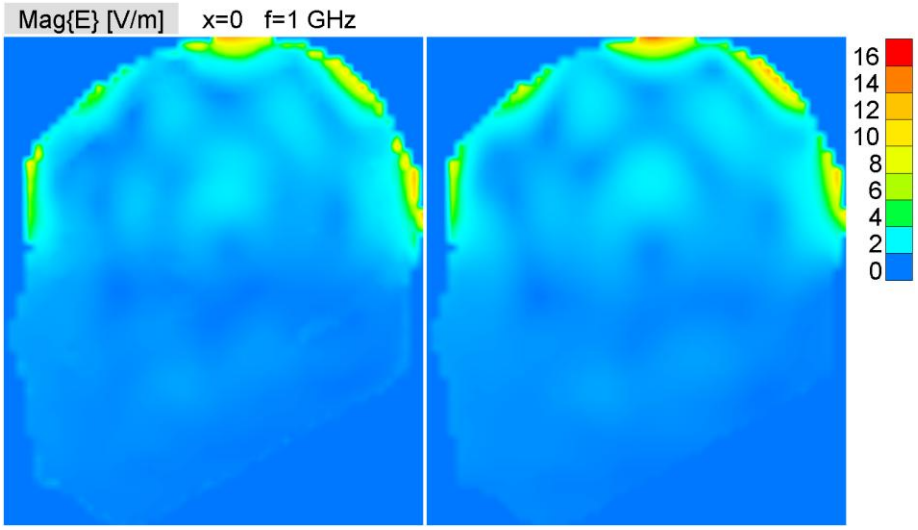


Figure 27. Scattering parameters (S_{ij}) of the seven-tissue reference head and the equivalent homogeneous head obtained using the optimized average dielectric properties.

As can be seen from Table VI, the permittivity computed using the Lichtenecker formula produced the smallest error. Therefore, this value was selected as the initial estimate for the gradient-based optimization procedure. The optimization converged after several iterations, yielding ε_r = 34.68 -j12.68 the final equivalent dielectric properties of the reference head model. Figure 27 compares the magnitudes of the scattering parameters, computed using MTPR antenna

configurations, obtained for the original heterogeneous phantom and the optimized homogeneous reference phantom, together with the magnitude of their difference. The close agreement between the two responses indicates that the optimized equivalent model successfully reproduces the dominant electromagnetic behavior of the anatomically realistic phantom.



(a) (b)

Figure 28. Electric Field inside (a) head with seven tissues, (b) homogeneous head.

To further assess the validity of the reference head approximation, the spatial distribution of the electric field inside the phantom was examined. Figure 28 presents the magnitude of the electric field vector for both the heterogeneous and equivalent homogeneous models. The results demonstrate a high level of agreement, confirming that the optimized dielectric properties preserve not only the scattering characteristics but also the internal field distribution of the original model.

Table VII. NUMBER OF UNKNOWNS AND EXECUTION TIME

Model	No. of Unknowns	Execution Time [s]
Exact Head	60778	627.05
Homogeneous Head	24592	140.19

The reduction in model complexity achieved by the homogeneous representation also results in a significant improvement in computational efficiency. Since the equivalent model contains only a single dielectric region, the execution time is substantially reduced while maintaining acceptable electromagnetic accuracy. As summarized in Table VII, the simulation time is reduced by approximately a factor of five compared with the original heterogeneous phantom. In addition to shorter execution times, the simplified model also lowers memory requirements and overall computational burden. All simulations were performed on a desktop machine with an Intel i7-920 processor (2.67 GHz) and 32 GB of RAM.

Despite the complexity of the original anatomical model, the equivalent homogeneous phantom produced scattering-parameter errors on the order of 10%, while significantly reducing the computational cost. These results confirm that the developed reference head is suitable for use as an initial estimate in iterative quantitative reconstruction algorithms.

5.1. Self-convergence strategy for Electric Field

This section presents a self-convergence testing strategy for assessing the numerical reliability of the 3-D EM simulations used in the MMWI framework [40]. The objective is to verify that the computed electromagnetic fields and scattering parameters using MHP antenna configuration remain stable as the mesh, basis functions, and solver settings are refined. This helps ensure that the simulation results are governed by the underlying electromagnetic behavior rather than numerical artifacts. The proposed approach provides practical guidelines for generating accurate and reproducible forward data for both qualitative and quantitative MMWI applications.

From the MMWI standpoint, the primary EM outputs are:

- the electric field within the head, $\mathbf{E}$, and
- the S-parameters of an N-antenna array, s_{ij}, $i,j = 1,\dots,N$.

Secondary (differential) electromagnetic quantities of interest are:

- the differential electric field, $\Delta\mathbf{E}$, and
- the differential S-parameters, Δs_{ij},

defined as differences between simulations with and without the modeled stroke:

$$\Delta\mathbf{E} = \mathbf{E}^{(\text{stroke})} - \mathbf{E}^{(\text{baseline})},$$
$$\Delta s_{ij} = s_{ij}^{(\text{stroke})} - s_{ij}^{(\text{baseline})}, i,j = 1,\dots,N. \quad (14a, b)$$

5.1.1. Relative Mean Absolute (RMA) Errors

To quantify the agreement between a refined solution and a reference, we employ the Relative Mean Absolute (RMA) error for both electric fields and S-parameters:

$$E_{\mathrm{RMA}} = \frac{\sum_{k=1}^{M} | E_k - E_k^{\mathrm{ref}} |}{\sum_{k=1}^{M} | E_k^{\mathrm{ref}} |}, S_{\mathrm{RMA}} = \frac{\sum_{i=1}^{N} \sum_{j=1}^{N} | s_{ij} - s_{ij}^{\mathrm{ref}} |}{\sum_{i=1}^{N} \sum_{j=1}^{N} | s_{ij}^{\mathrm{ref}} |}, \qquad (15a, b)$$

where "ref" denotes the chosen reference state and $E_k$is the field at the k-th of M sampling locations inside the head. For differential metrics, E and s_{ij} in (15) are replaced by ΔE and Δs_{ij}, respectively.

5.1.2. h, p, and hp Refinements

The self-convergence protocol is iterative procedure. At each step, we increase the number of unknowns, recompute the observables, and measure the change with respect to the previous step. Convergence is declared when these changes fall below a specified tolerance for at least two consecutive steps. We employ three canonical refinement pathways:

- h-refinement: increase the number of surface patches (finer mesh) while keeping the lowest expansion orders (e.g., rooftop-like) across patches.
- p-refinement: raise the basis expansion orders on a fixed mesh to capture higher spatial detail without altering topology.
- hp-refinement: combine mesh refinement with basis-order increases to benefit from both geometric and functional enrichment.

In the EM solver, these pathways are conveniently controlled via the reference frequency f_{ref} (which determines λ_{ref} and thus the expansion orders) and the maximum patch size (MPS):

- h-refinement: target MPS $\approx \lambda_{\mathrm{ref}}/6$(small patches, rooftop-like behavior).
- p-refinement: target MPS $\approx 10\ \lambda_{\mathrm{ref}}$(coarser mesh but higher orders).
- hp-refinement: target MPS $\approx 2\ \lambda_{\mathrm{ref}}$(moderate mesh with moderate–high orders).

Increasing $f_{\mathrm{ref}}$and/or decreasing MPS raises the unknown count, typically improving accuracy at the expense of runtime and memory. The choice among h, p, and hp refinements depends on the mesh quality (e.g., quadrilateral shape factors), geometry smoothness, and the sensitivity of the target observables to local field variation [52] – [56].

5.1.3. Practical Scales and Computational Considerations

For the complete MMWI scenario with five tissues shown in Figure 1(c), the default simulation settings ($\sigma_{\max} = 3$ mm, $f_{\mathrm{ref}} = f_0$, MPS $= 2\lambda$) result in approximately 5×10^4 unknowns. Small increases in the basis-function order p or reductions in the maximum patch size (MPS) can easily increase the problem

size beyond 10^6 unknowns. At this level, performing a full self-convergence analysis becomes computationally demanding. To reduce the computational burden, the following acceleration strategies are adopted:

1. Subsystem-based refinement: Only one subsystem is refined at a time, such as the phantom, stroke, or antenna, while all other parts remain at their default settings. This allows the convergence behavior of each subsystem to be evaluated independently and avoids unnecessary refinement of the entire model.

2. Phantom refinement using plane-wave excitation: To study the effect of phantom refinement on the electric field and scattering response, the antenna array is replaced by plane-wave excitation. This preserves the main electromagnetic behavior inside the head while eliminating the complexity introduced by the antenna system, resulting in faster and easier-to-interpret convergence studies.

3. Antenna refinement using a single element: To evaluate the influence of antenna refinement on the S-parameters, only a single antenna is analyzed in a representative environment, including the coupling medium and antenna standoff distance. This approach captures the matching characteristics and near-field interactions without requiring simulation of the full antenna array.

Using these strategies, it was found that, for a single antenna configuration (Figure 11), hp-refinement with $f_{\mathrm{ref}} = 2f_0$ produces stable S-parameters, while further increases in reference frequency result in negligible changes. Therefore, this antenna setting is used for all elements in the complete MMWI model. For applications requiring higher matching accuracy, p-refinement combined with multiple edging operations is recommended. Under these conditions, the relative mean absolute (RMA) error of the S-parameters can be reduced to approximately $s_{\mathrm{RMA}} \approx 0.03\%$.

By contrast, the stroke inclusion is small and localized, so we model it with a very refined sub-mesh at low cost in unknowns, this ensures stable ΔE and Δs_{ij} without inflating total runtime.

5.2. Self-Convergence Testing for Electric Field

To evaluate field-level accuracy, we estimate the convergence rates of the electric field **E** and the differential electric field $\Delta\mathbf{E}$ using five-tissue head phantoms (skin, fat, muscle, skull, and brain) with and without the stroke inclusion. Both phantoms are decimated with $\sigma_{\max} = 3$ mm and illuminated by a broadside, vertically polarized plane wave of unit electric-field amplitude. This configuration isolates the effect of phantom discretization and basis-order settings on field accuracy, without the additional complexity introduced by the antenna array.

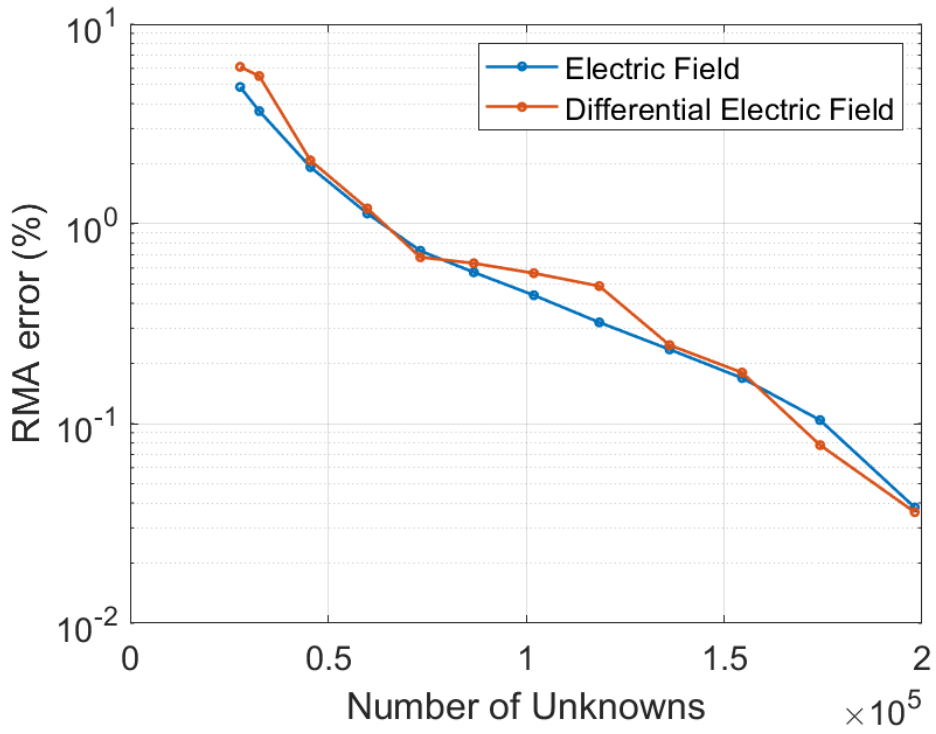


Figure 29. RMA error (%) vs. number of unknowns for electric field (blue) and differential electric field (orange).

Figure 29 reports the RMA errors, E_{RMA} and ΔE_{RMA}, versus the number of unknowns, under hp-refinement (combined mesh and basis enrichment). As the unknown count increases, both E_{RMA} and ΔE_{RMA} decrease monotonically. In particular, the errors can be reliably driven down to approximately $E_{\mathrm{RMA}} \approx \Delta E_{\mathrm{RMA}} \approx 0.03\%$, which indicates that the forward model has reached a numerically robust regime for MMWI use. These results are consistent with the expectation that mesh quality, basis richness, and solver conditioning, as controlled through the quadrilateral meshing and max-orthogonalized bases, promote smooth error decay towards a converged solution [48], [55] – [57], [69].

5.3. Self-Convergence Testing for Scattering Parameters

We next assess the convergence of scattering parameters for the full array configuration. The S-parameters $s_{ij}$and their differential counterparts $\Delta s_{ij}$are computed using five-tissue head phantoms, with and without the stroke, again decimated with $\sigma_{\max} = 3$ mm, and excited by a 21-antenna array. To isolate the phantom's contribution to numerical accuracy, refinement is applied only to the phantom (the antenna elements retain the previously validated settings; antenna optimization and edging guidelines in [69]). Thus, in Figure 30 the number of unknowns primarily reflects the phantom discretization and basis enrichment.

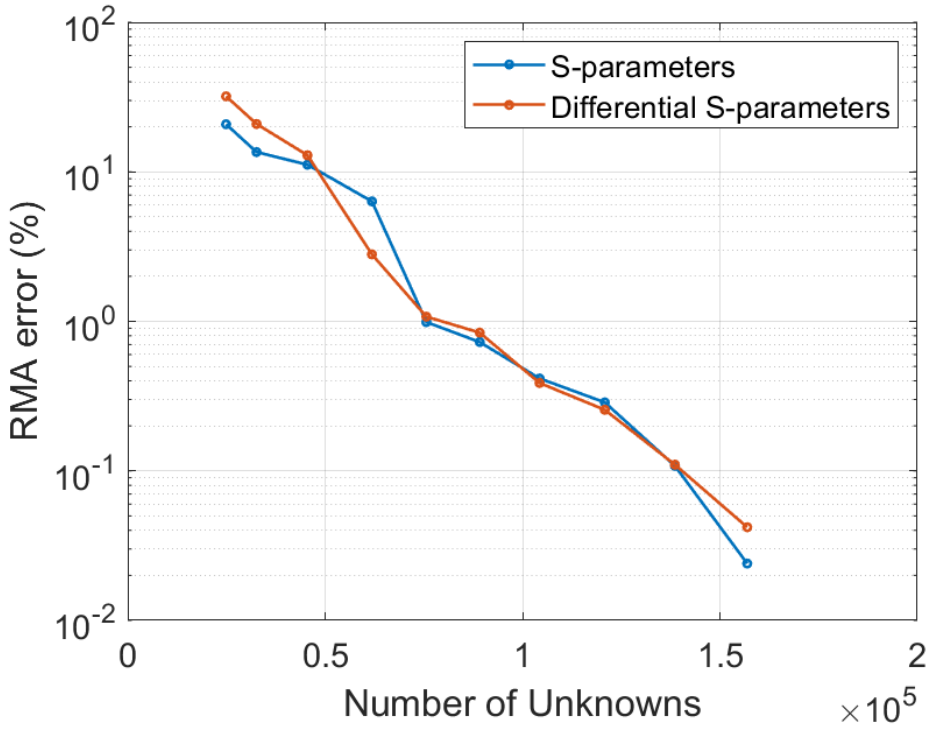
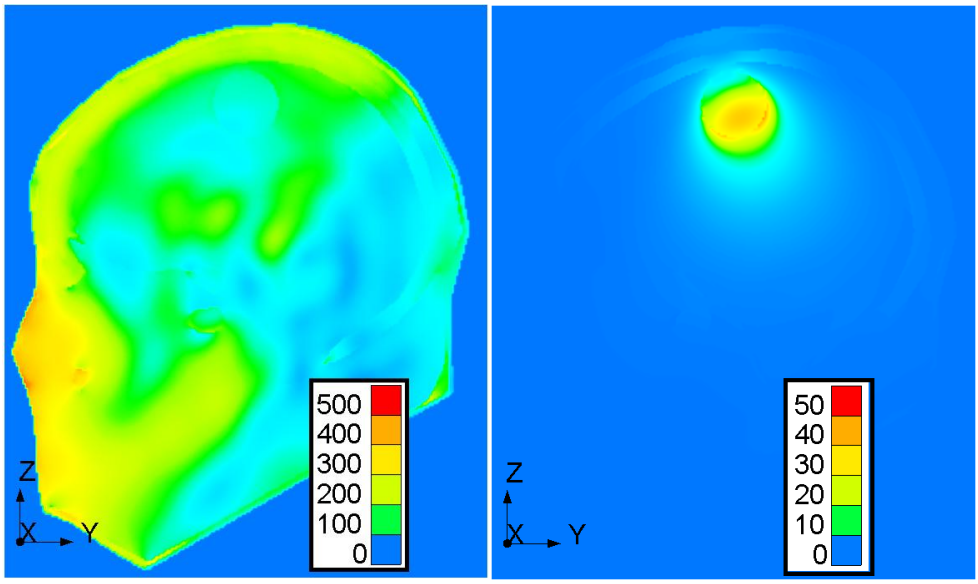


Figure 30. RMA error (%) vs. number of unknowns for S-parameters (blue) and differential S-parameters (orange).

The RMA errors for s_{ij} and Δs_{ij} decrease systematically with hp-refinement, reaching approximately $s_{\mathrm{RMA}} \approx \Delta s_{\mathrm{RMA}} \approx 0.03\%$. This confirms that (i) the phantom-only refinement is sufficient to drive scattering parameters into a self-converged regime, and (ii) the local antenna settings (hp with $f_{\mathrm{ref}} = 2f_0$, plus p-refinement and multiple edging where needed) are already stable and need not be globally tightened for every convergence run.

Taken together, Figures 29 and 30 show that the RMA errors of regular quantities $(\mathbf{E}, s_{ij})$ and differential quantities $(\Delta\mathbf{E}, \Delta s_{ij})$ are of similar magnitudes under the same refinement level. This is desirable as it indicates that the differential signals needed by MMWI are not dominated by numerical noise and converge at rates comparable to their absolute counterparts.



(a) (b)

Figure 31. (a) Magnitude of electric field and (b) differential electric field in the symmetrical plane of the head excited broadside by plane wave.

At the same time, Figure 31 highlights a key physical distinction: differential magnitudes are much smaller (roughly one order of magnitude lower) than the corresponding absolute fields. For example, Figure 31(a) shows that the electric-field magnitude in the stroke case, evaluated on the symmetry plane, ranges roughly from 0 to 500 mV/m, whereas Figure 31(b) shows the differential field magnitude in the same plane ranging approximately from 0 to 50 mV/m. This illustrates why monitoring both primary and differential quantities in the self-convergence test is essential: even small residual numerical errors in **E** can obscure the much smaller $\Delta\mathbf{E}$ if not properly controlled. The same rationale applies to s_{ij}versus Δs_{ij}.

5.4. Influence of Surface Decimation on 3D EM Simulation Accuracy

In this section, we evaluate how surface decimation influences the convergence rate of S-parameters in the full MMWI scenario. We consider a family of phantoms obtained with bounded-deviation decimation, varying the maximum allowed surface deviation from $\sigma_{\max} = 0$ mm (no decimation) to $\sigma_{\max} = 3$ mm in increments of $\Delta\sigma_{\max} = 0.5$ mm. For each $\sigma_{\max}$, we perform hp-refinement by increasing the reference frequency from $f_{\text{ref}} = f_0$ up to $f_{\text{ref}} = 9f_0$ in steps of $\Delta f = f_0$, thereby growing the number of unknowns through a combination of basis-order enrichment and controlled patch sizing. The solution obtained with $\sigma_{\max} = 0$ mm and $f_{\text{ref}} = 10f_0$ is adopted as the reference for error normalization. Figure 32 plots the corresponding RMA errors of the array S-parameters versus the number of unknowns associated with the phantom (antenna settings are kept fixed at the validated configuration).

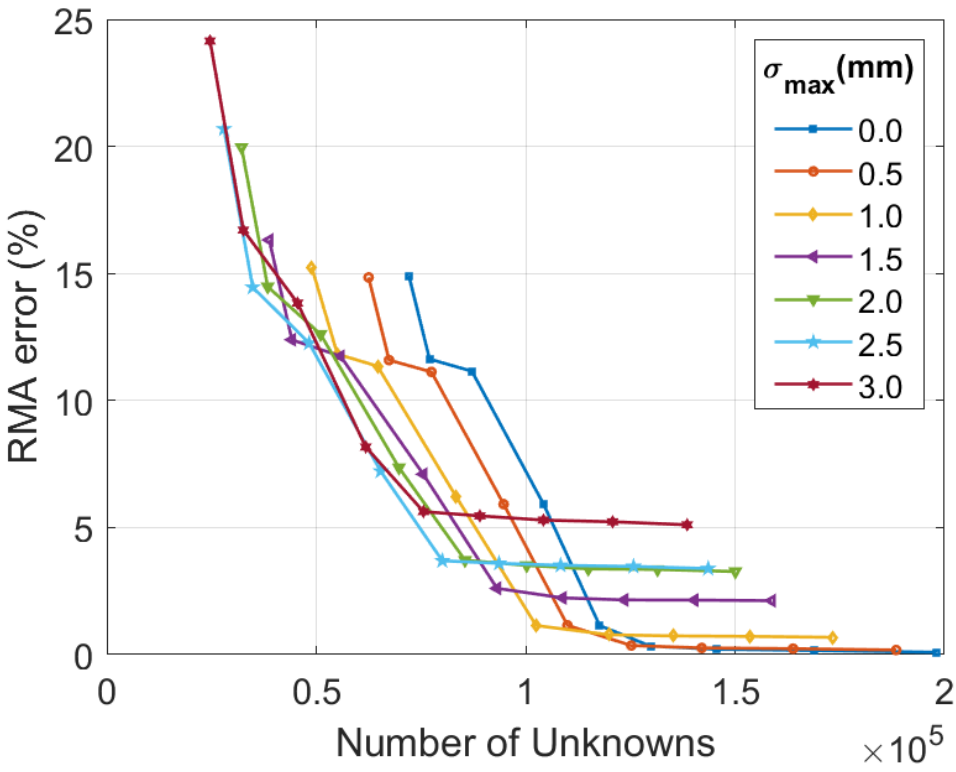


Figure 32. RMA Error of S-parameters as a function of the Number of Unknowns needed for head for different values of the Maximum Allowed Deviation, σ_{max} .

A similar trend can be observed in the RMA error curves. For each decimation level, the RMA error decreases as the number of unknowns increases. However, beyond a certain point, additional refinement produces little or no further improvement. This behavior occurs because the remaining error is dominated by the geometric changes introduced during the decimation process. Once the numerical discretization error becomes smaller than the geometric modeling error, further refinement of the mesh or basis functions no longer reduces the overall error, and the convergence reaches a limiting value. As expected, larger $\sigma_{\max}$ produces a higher threshold (i.e., a higher minimum attainable RMA error). Figure 33 summarizes these threshold values as a function of $\sigma_{\max}$ over $0 \leq \sigma_{\max}$(mm), showing a clear trend of increasing error floor with increasing decimation deviation. A similar trend is observed for the electric-field solutions inside the head. The RMA error of the primary electric field decreases with refinement until a limiting value is reached. Beyond this point, further mesh or basis refinement produces little improvement because the remaining error is mainly caused by the geometric changes introduced during the decimation process rather than by numerical discretization.

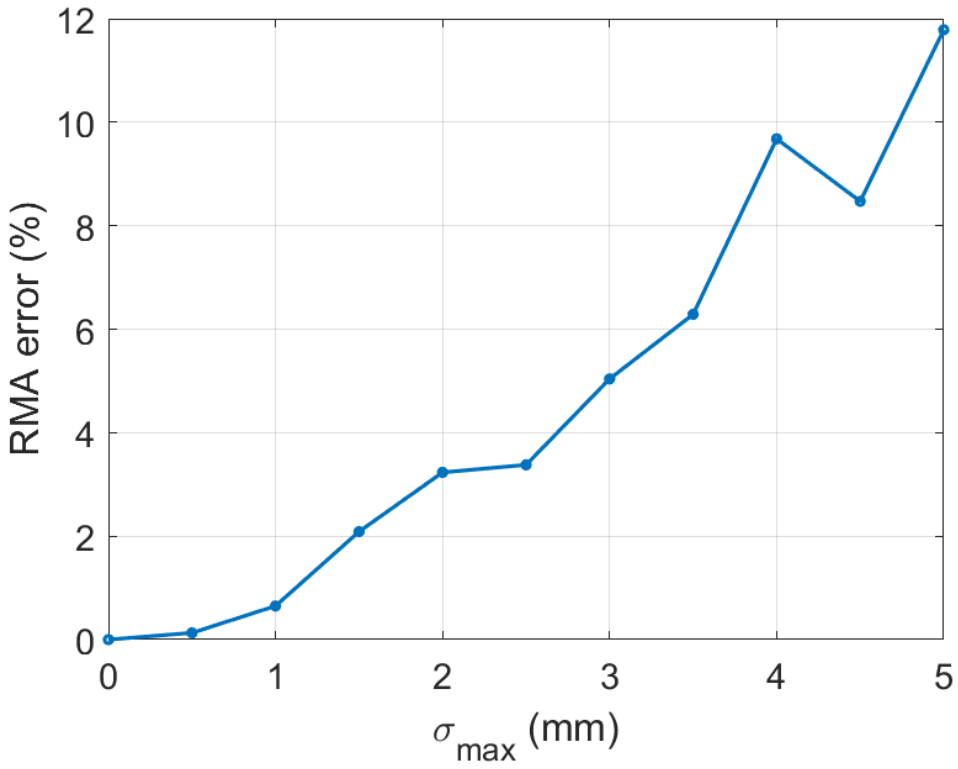


Figure 33. Minimal RMA error of S-parameters versus maximum allowed deviation.

The error floor is mainly caused by the geometric changes introduced during the decimation process. Small modifications of tissue boundaries affect the near electromagnetic fields and the coupling between antenna elements. However, because the same decimation level is applied to both the reference head and the stroke-containing head, these geometric effects are largely cancelled in the differential quantities, $\Delta\mathbf{E}$ and Δs_{ij}. As a result, the differential RMA errors continue to decrease smoothly with refinement, as shown in Figures 29 and 30, whereas the errors of the absolute quantities become limited by the selected decimation level once numerical convergence has been reached.

This result suggests that the choice of the maximum allowed deviation is more critical for absolute quantities, such as the primary electric field and S-parameters, than for differential quantities. Therefore, moderate decimation can be used in differential imaging studies without significantly affecting the diagnostic information or the stability of the imaging algorithms.

5.5. Validation of 3D EM Simulation Outputs for MMWI Applications

Validation of the 3D EM simulation data is essential to ensure that the forward results are sufficiently accurate for MMWI. The self-convergence strategy developed earlier can be directly integrated with an MMWI reconstruction workflow. In this combined approach, the iterative forward–inverse process is continued until two consecutive reconstructed images become nearly identical. When this condition is reached, the simulation is considered converged, and the numerical settings used in the final iteration can

be regarded as suitable defaults for similar scenarios. The associated RMS errors also provide practical upper limits for acceptable modeling errors in reliable MMWI applications.

Many qualitative and quantitative imaging algorithms in MMWI rely on the inverse scattering equation (ISE) [70] – [72]. For a given configuration, the residual terms that arise from numerical approximation or modeling inaccuracy can be written as

$$r_{ij} = \Delta s_{ij} - \frac{j\omega}{2}\int_v \Delta\varepsilon(\mathbf{r}')\, S_{ij}(\mathbf{r}')\, dv, i, j = 1, \ldots, N, \tag{16a}$$

where Δs_{ij} are the differential S-parameters, ω is the angular frequency, and $\Delta\varepsilon(\mathbf{r}')$ denotes the difference in complex relative permittivity between the stroke and the surrounding head tissue. The exact scattering operator appearing in (16a) is

$$S_{ij}(\mathbf{r}') = \mathbf{E}_{i1}(\mathbf{r}') \cdot \mathbf{E}_{j2}(\mathbf{r}'), i, j = 1, \ldots, N, \tag{16b}$$

with $\mathbf{E}_{i1}$ representing the internal field when port i is excited and all other ports are matched, and $\mathbf{E}_{j2}$ representing the corresponding field when the stroke is present. The volume $v$covers only the stroke region.

The total field $\mathbf{E}_{j2}$ inside the stroke is unknown, making the inverse problem nonlinear. A common simplification is to apply the Born approximation, in which the total field is replaced by the incident field $\mathbf{E}_{j1}$in (16b). Although the modeled stroke is not electrically small at 1 GHz, the Born approximation is considered here to obtain an approximate scattering operator. Under this approximation, the scattering operator is expressed as

$$S_{ij}(\mathbf{r}') \approx \mathbf{E}_{i1}(\mathbf{r}') \cdot \mathbf{E}_{j1}(\mathbf{r}'), i, j = 1, \ldots, N. \tag{17}$$

Both the exact and approximate residuals and scattering operators form higher-order EM data that can be used to assess the quality of the forward solution. A convenient metric for this purpose is the relative MMWI residual, defined as

$$R_{\mathrm{RMA}} = \frac{\sum_{i=1}^{N} \sum_{j=1}^{N} | r_{ij} |}{\sum_{i=1}^{N} \sum_{j=1}^{N} | \Delta s_{ij} |}. \tag{18}$$

This ratio expresses the magnitude of the modeling error relative to the differential scattering response used by MMWI algorithms.

In evaluating (16a), the integration is carried out numerically using the known permittivity contrast $\Delta\varepsilon(\mathrm{r}')$, which is nonzero only inside the stroke. This allows a direct and quantitative comparison between the EM solver's output and the expected physical scattering behavior. As a result, the R_{RMA} value provides a clear indication of whether the simulated 3D EM data are sufficiently accurate for reliable reconstruction, including the detection and localization of stroke-like inclusions.

Continuing the validation procedure, Figure 34 presents the RMA residuals of both the exact and approximate inverse scattering equations for the full-wave simulation scenario, plotted as a function of the total number of unknowns. These simulations were carried out using default modeling settings for the stroke and antenna configuration, while the head model was decimated using a maximum deviation of $\sigma_{\max} = 3\,\mathrm{mm}$. To strengthen the accuracy assessment, hp-refinement was applied by gradually increasing the reference frequency from

$$f_{\mathrm{ref}} = f_0 \mathrm{to} f_{\mathrm{ref}} = 9f_0, \tag{19}$$

in increments of

$$\Delta f = 0.5 f_0. \tag{20}$$

Analysis of RMA Residual Behavior: As shown in Figure 34, increasing the number of unknowns does not significantly change the behavior of the RMA residuals. The residual associated with the exact inverse scattering equation stays below 1%, indicating that the forward 3D EM model is already sufficiently accurate, and that additional mesh refinement or increased unknown count does not meaningfully improve the solution. This remaining 1% error reflects the residual limitations of EM modeling, such as discretization and numerical interpolation.

In contrast, the residual associated with the approximate inverse scattering equation remains slightly below 20%. The approximately 19% gap between the exact and approximate RMA residuals is directly

attributable to the Born approximation, which replaces the total field by the incident field in (16b). Given the physical size and permittivity contrast of the modeled stroke region, this approximation is only marginally valid, and the observed error confirms its limited suitability for this configuration.

MMWI Image Reconstruction Using TSVD and LSM: Using standard parameter settings for both reconstruction methods as described in [73], [74], microwave images were reconstructed from the full-wave 3D EM data at each refined reference frequency. The results, shown in Figure 35(a) for the TSVD method and Figure 35(b) for the LSM method, reveal that all reconstructions converge to the same pixelated image, independent of the chosen reference frequency.

This frequency-insensitive behavior is explained by the fact that

$$R_{\mathrm{RMA}}^{\mathrm{exact}} \ll R_{\mathrm{RMA}}^{\mathrm{approx}}, \tag{21}$$

which holds consistently across all examined hp-refinement steps. Because the exact RMA residual is significantly smaller than the approximate one, the exact ISE dominates the tertiary EM data quality. Consequently, when inequality (21) is satisfied, the tertiary EM data can be considered validated for use with approximate-ISE-based MMWI algorithms. In other words, the accuracy of the full-wave 3D EM simulation is sufficient to ensure that approximate inversion techniques (such as TSVD or LSM) operate in a stable and reliable manner.

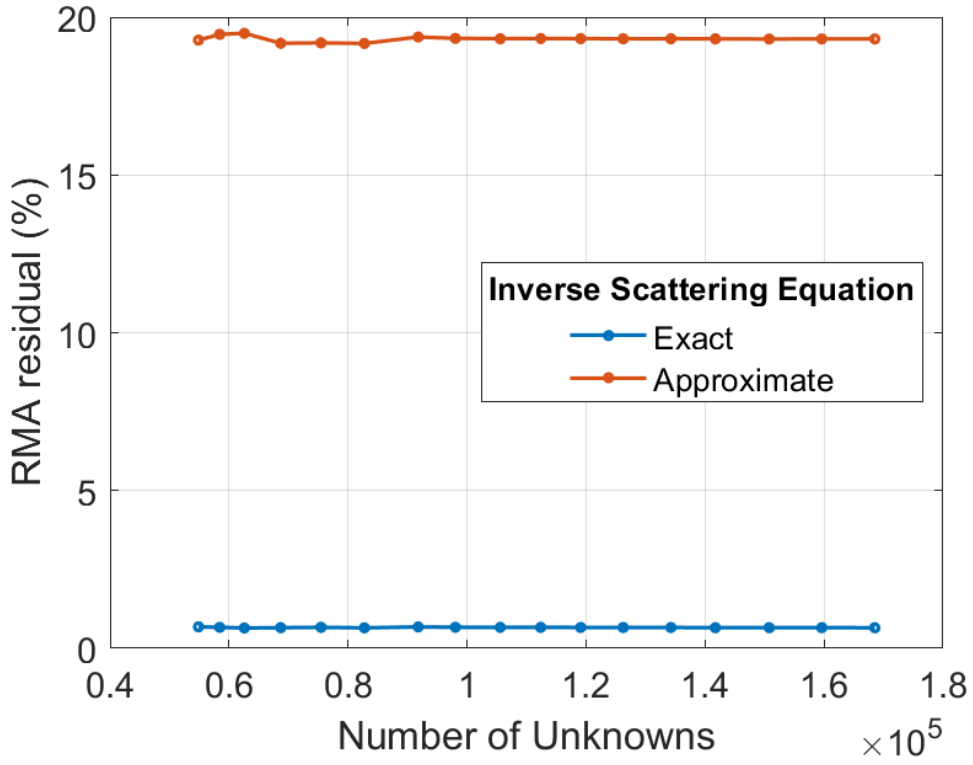


Figure 34. RMA residual as a function of the total number of unknowns

The combined results from Figure 34 and Figure 35 demonstrate that:

1. The 3D EM forward model reaches a numerically stable regime, with RMA residuals for the exact ISE well below 1%.
2. Born-approximation-based inversion is feasible only when the exact residual remains much smaller than the approximate one.
3. Image reconstruction is robust with respect to variations in the reference frequency, provided that the EM modeling accuracy meets the threshold described by inequality (21).

This validation step therefore confirms that the simulation pipeline, consisting of controlled decimation, EM solution refinement, and self-convergence, produces forward data of sufficient fidelity for stroke-oriented MMWI applications.

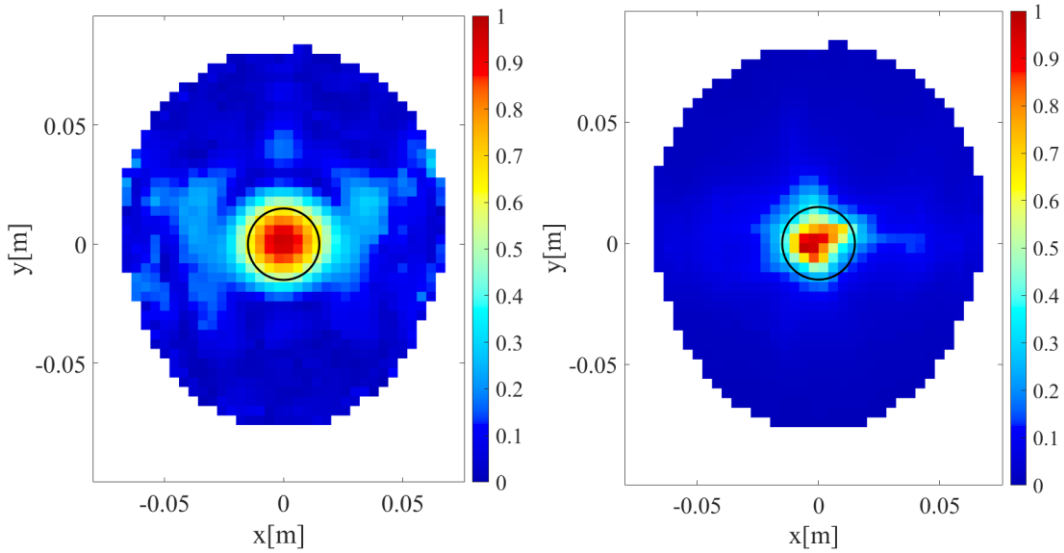


Figure 35. MW images reconstructed using (a) the TSVD method and (b) the LSM method applied to 3D EM full-wave data.

Chapter 6:
Conclusion

This thesis presents an accuracy-controlled framework for 3D EM modeling in MMWI, with a focus on brain stroke imaging and monitoring. The main objective of the work has been to develop simulation models that are both computationally efficient and sufficiently accurate for use in microwave imaging algorithms. Emphasis has been placed on understanding how geometric modeling, mesh quality, solver settings, and numerical convergence affect the reliability of the generated EM data. All investigations were carried out in a simulation environment, allowing complete control over the modeling parameters and validation process.

The work begins by developing a representative MMWI scenario consisting of a five-tissue head phantom, a stroke-like dielectric inclusion, and a 21-element multistatic antenna array operating around 1 GHz. This scenario serves as a realistic benchmark for evaluating the proposed modeling and validation techniques and reflects the main characteristics of practical microwave brain-imaging systems.

A key contribution of this thesis is the design of a controlled-deviation decimation and quadrilateral meshing framework for the most complex part, which has the most unknowns, i.e., anatomical STL head models. High-resolution anatomical phantoms contain a very large number of triangular elements, making EM simulations without any simplifications impossible. The proposed approach combines bounded-deviation decimation, triangle-to-quadrilateral conversion, and mesh refinement to generate high-quality quadrilateral meshes while maintaining close agreement with the original anatomy. The results show that the number of elements can be reduced by approximately three to four times while preserving geometric fidelity required for accurate electromagnetic simulations.

To ensure the reliability of the generated simulation data, a systematic self-convergence strategy was developed and applied to both electric fields and S-parameters. The method uses h-, p-, and hp-refinement techniques and monitors RMA errors as the number of unknowns increases. The results demonstrate that both primary quantities and differential quantities converge to stable solutions. For non-decimated models, the RMA errors were reduced to approximately 0.03%, indicating a numerically stable solution suitable for microwave imaging studies. The proposed convergence procedure provides practical guidelines for selecting mesh density, basis-function order, and solver settings while avoiding unnecessary computational cost.

The effect of surface decimation on electromagnetic accuracy was also investigated in detail. The results showed that absolute quantities, such as the electric field and S-parameters, exhibit an error floor that depends on the allowed geometric deviation. As the decimation level increases, geometric approximation errors eventually dominate and limit further improvement through numerical refinement. In contrast, differential quantities remain much less sensitive to decimation because identical geometric approximations are present in both the baseline and stroke cases and therefore cancel during subtraction. This finding is particularly important for differential microwave imaging, where moderate mesh simplification can significantly reduce computational cost without degrading the information used for stroke detection and localization.

A further contribution of the thesis is the validation framework based on the inverse scattering equation. Both the exact and Born-approximate forms of the ISE were analyzed using residual-based metrics. The residual associated with the exact ISE remained below 1% throughout the refinement studies,

demonstrating that the forward EM model provides highly reliable solutions. The residual of the Born-based approximation remained below 20%, highlighting the limitations of the approximation for the considered stroke scenario. Nevertheless, reconstructed images obtained using TSVD and LSM algorithms remained unchanged across different refinement levels, confirming that the generated forward EM data are sufficiently accurate for imaging purposes when the exact residual remains significantly smaller than the approximate residual. This provides a practical validation criterion for assessing the suitability of simulation data for microwave imaging algorithms.

Another important contribution is the introduction of a reference head model based on average dielectric properties. The reference head provides a simplified homogeneous representation of the anatomically realistic head while preserving its dominant electromagnetic behavior. Different averaging methods were investigated, and the final dielectric properties were obtained through gradient-based optimization. The resulting model reproduced the scattering response of the original multi-tissue head with an error of approximately 10%, while reducing the computational cost by about a factor of five. This reference head can be viewed as the electromagnetic equivalent of a healthy baseline condition and can be as an initial model for iterative reconstruction methods such as DBIM.

Overall, this thesis establishes a practical workflow for electromagnetic modeling of MMWI scenarios, integrating controlled mesh simplification, high-quality quadrilateral meshing, self-convergence testing, and ISE-based validation. The developed methodology enables anatomically realistic head models to be simplified while preserving their essential electromagnetic characteristics, providing accurate and computationally efficient forward EM data for microwave imaging and reconstruction algorithms. It also provides quantitative measures for assessing geometric accuracy, numerical convergence, and imaging reliability.

.

References

1. G. Zhu, A. Bialkowski, L. Guo, B. Mohammed and A. Abbosh, "Stroke Classification in Simulated Electromagnetic Imaging Using Graph Approaches," in IEEE Journal of Electromagnetics, RF and Microwaves in Medicine and Biology, vol. 5, no. 1, pp. 46-53, March 2021, doi: 10.1109/JERM.2020.2995329.

2. A. S. M. Alqadami, A. Trakic, A. E. Stancombe, B. Mohammed, K. Bialkowski and A. Abbosh, "Flexible Electromagnetic Cap for Head Imaging," in IEEE Transactions on Biomedical Circuits and Systems, vol. 14, no. 5, pp. 1097-1107, Oct. 2020, doi: 10.1109/TBCAS.2020.3025341.

3. R. Chandra, H. Zhou, I. Balasingham and R. M. Narayanan, "On the Opportunities and Challenges in Microwave Medical Sensing and Imaging," in IEEE Transactions on Biomedical Engineering, vol. 62, no. 7, pp. 1667-1682, July 2015, doi: 10.1109/TBME.2015.2432137.

4. M. Pastorino, A. Randazzo, Microwave Imaging Methods and Applications, in Artech House, 2018.

5. L. Crocco, I. Karanasiou, M. James, R. Conceição, "Emerging Electromagnetic Technologies for Brain Diseases Diagnostics, Monitoring and Therapy," Springer, Cham, Switzerland, 2018.

6. R. Conceição, J. Mohr, M. O'Halloran, "An Introduction to Microwave Imaging for Breast Cancer Detection", Switzerland, Springer, 2018

7. M. Persson, A. Fhager, H. D. Trefn`a, Y. Yu, T. McKelvey, G. Pegenius, J. E. Karlsson, and M. Elam, "Microwave-based stroke diagnosis making global prehospital thrombolytic treatment possible," IEEE Transactions on Biomedical Engineering, vol. 61, no. 11, pp. 2806–2817, Nov 2014.

8. S. Candefjord, J. Winges, A. Malik, Y., Yu, T. Rylander, T. McKelvey, A. Fhager, M. Elam, and M. Persson, "Microwave technology for detecting traumatic intracranial bleedings: tests on phantom of subdural hematoma and numerical simulations," Medical & Biological Engineering & Computing, vol. 55, no. 8, pp. 1177–1188, Aug 2017.

9. A. T. Mobashsher and A. M. Abbosh, "On-site rapid diagnosis of intracranial hematoma using portable multi-slice microwave imaging system," Scientific Reports, vol. 6, no. Article ID 37620, pp. 1–17, November 2016.

10. A. T. Mobashsher, K. S. Bialkowski, A. M. Abbosh, and S. Crozier, "Design and experimental evaluation of a non-invasive microwave head imaging system for intracranial haemorrhage detection," PLoS ONE, vol. 11, no. 4, pp. 1–29, April 2016.

11. M. Hopfer, R. Planas, A. Hamidipour, T. Henriksson, and S. Semenov, “Electromagnetic tomography for detection, differentiation, and monitoring of brain stroke: A virtual data and human head phantom study.” IEEE Antennas and Propagation Magazine, vol. 59, no. 5, pp. 86–97, Oct 2017.

12. R. Scapaticci, J. Tobon, G. Bellizzi, F. Vipiana and L. Crocco, "Design and Numerical Characterization of a Low-Complexity Microwave Device for Brain Stroke Monitoring," in IEEE Transactions on Antennas and Propagation, vol. 66, no. 12, pp. 7328-7338, Dec. 2018, doi: 10.1109/TAP.2018.2871266.

13. S. Ahsan, M. Koutsoupidou, E. Razzicchia, I. Sotiriou and P. Kosmas, "Advances towards the Development of a Brain Microwave Imaging Scanner," 2019 13th European Conference on Antennas and Propagation (EuCAP), 2019, pp. 1-4.

14. A. Fedeli, C. Estatico, M. Pastorino and A. Randazzo, "Microwave Detection of Brain Injuries by Means of a Hybrid Imaging Method," in IEEE Open Journal of Antennas and Propagation, vol. 1, pp. 513-523, Sept. 2020, doi: 10.1109/OJAP.2020.3024276.

15. J. A. Tobon Vasquez, R. Scapaticci, G. Turvani, G. Bellizzi, D. O. Rodriguez-Duarte, N. Joachimowicz, B. Duchêne, E. Tedeschi, M. R. Casu, L. Crocco, and F. Vipiana, “A Prototype Microwave System for 3D Brain Stroke Imaging,” in Sensors, vol. 20, no. 9, pp 2607, May 2020.

16. D. O. Rodriguez-Duarte, J. A. T. Vasquez, R. Scapaticci, L. Crocco and F. Vipiana, "Brick-Shaped Antenna Module for Microwave Brain Imaging Systems," in IEEE Antennas and Wireless Propagation Letters, vol. 19, no. 12, pp. 2057-2061, Dec. 2020, doi: 10.1109/LAWP.2020.3022161.

17. S. Y. Semenov and D. R. Corfield, “Microwave tomography for brain imaging: feasibility assessment for stroke detection,” Int. J. of Antenna and Propagat., vol. 2008, p. 8 pages, 2008.

18. S. Semenov, T. Huynh, T. Williams, B. Nicholson, and A. Vasilenko, “Dielectric properties of brain tissue in acute ischemic stroke: experimental study on swine,” Bioelectromagnetics, vol. 38, pp. 158–163, 2017.

19. B. Kolundzija, M. N. Stevanovic, M. Stevanetic, B. Ninkovic and T. Singh, "Advanced 3D EM Simulation Environment for Development, Testing, and Usage of Medical Microwave Imaging Devices," 2019 14th International Conference on Advanced Technologies, Systems and Services in Telecommunications (TELSIKS), Nis, Serbia, 2019, pp. 186-189, doi: 10.1109/TELSIKS46999.2019.9002224.

20. T. Singh, M. Nikolic Stevanovic, and B. Kolundzija, “Survey and Classification of Antennas for Medical Applications,” in Proc. 13th European Conf. on Antennas and Propagation (EuCAP), Krakow, Poland, 2019, doi: 10.5281/zenodo.2647495.

21. T. Singh, D. M. Ninkovic, B. M. Kolundzija, and M. Nikolic Stevanovic, “Smooth Polynomial Approach for Microwave Imaging in Sparse Processing Framework,” IEEE Access, vol. 10, pp. 120616–120629, 2022, doi: 10.1109/ACCESS.2022.3217221.

22. M. N. Stevanovic, T. Singh, B. Ninkovic and B. Kolundzija, "Microwave Sparse Imaging Applied to Stroke Monitoring," 2021 XXXIVth General Assembly and Scientific Symposium of the International Union of Radio Science (URSI GASS), Rome, Italy, 2021, pp. 1-4, doi: 10.23919/URSIGASS51995.2021.9560370.

23. M. Stevanetic, B. Kolundzija, T. Singh, and M. Nikolic Stevanovic, “Simulation Study of Voxel-Based Head Phantom for Medical Microwave Imaging,” in Proc. IX International Conference IcETRAN, Novi Pazar, Serbia, Jun. 2022, pp. AP1.4-1–AP1.4-5.

24. T. Singh, B. Ninkovic, M. Tasic, M. Nikolic Stevanovic, and B. Kolundzija, “Tools and Strategies for 3D EM Modeling and Design of Microwave Imaging Systems for Medical Applications,” in Computational Intelligence and Image Processing in Medical Applications, World Scientific, 2022, ch. 4.4, pp. 297–314, doi: 10.1142/9789811257452_0017.

25. T. Singh, B. Ninkovic, M. Stevanetic, M. Tasic, M. Nikolic Stevanovic, and B. Kolundzija, “Numerical Modeling of Complex 3D Electromagnetic Scenarios for Medical Microwave Imaging,” in Electromagnetic Imaging for a Novel Generation of Medical Devices, F. Vipiana and L. Crocco, Eds. Cham, Switzerland: Springer, 2023, doi: 10.1007/978-3-031-28666-7_4.

26. T. Singh, B. Ninkovic, M. S. Tasic, M. Nikolic Stevanovic, and B. Kolundzija, “New Method for Calculation of Average Electric Properties of Reference Head Phantom in Microwave Imaging,” in Proc. 16th European Conf. on Antennas and Propagation (EuCAP), Madrid, Spain, 2022, doi: 10.23919/EUCAP53622.2022.9769058.

27. T. Singh, M. Stevanetic, M. Stevanovic and B. Kolundzija, "Homogenization of Voxel Models using Material Mixing Formulas," in 14th European Conference on Antennas and Propagation, 2020, pp. 1-4, doi: 10.23919/EuCAP48036.2020.9135081.

28. J. A. T. Vasquez, R. Scapaticci, G. Turvani, M. Vacca, I. Sarwar, M. R. Casu, G. Dassano, N. Joachimowicz, B. Duchˆene, G. Bellizzi, E. Tedeschi, L. Crocco, and F. Vipiana, “A feasibility study for cerebrovascular diseases monitoring via microwave imaging,” in 2017 International Conference on Electromagnetics in Advanced Applications (ICEAA), Sept 2017, pp. 1280–1282.

29. T. Singh, S. Abedi, B. Ninkovic, M. N. Stevanovic, N. Joachimowz, H. Roussel and B. Kolundzija, "Smart Simplification of Anthropomorphic Head Phantom Aimed for Microwave Imaging," in 15th European Conference on Antennas and Propagation, Düsseldorf, Germany, 2021, pp. 1-4.

30. I. T. Rekanos, S. M. Panas and T. D. Tsiboukis, "Microwave imaging using the finite-element method and a sensitivity analysis approach," in IEEE Transactions on Medical Imaging, vol. 18, no. 11, pp. 1108-1114, Nov. 1999, doi: 10.1109/42.816074.

31. A. Fhager, S. K. Padhi and J. Howard, "3D Image Reconstruction in Microwave Tomography Using an Efficient FDTD Model," in IEEE Antennas and Wireless Propagation Letters, vol. 8, pp. 1353-1356, 2009, doi: 10.1109/LAWP.2009.2039032.

32. Z. Wang, E. G. Lim, Y. Tang, M. Leach, "Medical Applications of Microwave Imaging," in The Scientific World Journal, vol. 2014, Article ID 147016, 7 pages, 2014, doi.org/10.1155/2014/147016.

33. Jin-Lin Hu, Zhipeng Wu, McCann, H., Davis, L. E., & Cheng-Gang Xie, "Quasi-three-dimensional method of moments for analyzing electromagnetic wave scattering in microwave tomography systems," in IEEE Sensors Journal, vol. 5(2), 216–223. doi:10.1109/jsen.2004.842294.

34. B. Sohani, B. Khalesi, N. Ghavami, M. Ghavami, S.Dudley, A. Rahmani, G. Tiberi, "Detection of haemorrhagic stroke in simulation and realistic 3-D human head phantom using microwave imaging," in Biomedical Signal Processing and Control, vol. 61, 2020, 102001, ISSN 1746-8094, doi.org/10.1016/j.bspc.2020.102001.

35. B. Sohani, G. Tiberi, N. Ghavami, M. Ghavami, S. Dudley and A. Rahmani, "Microwave Imaging for Stroke Detection: Validation on Head-mimicking Phantom," in PhotonIcs & Electromagnetics Research Symposium - Spring (PIERS-Spring), 2019, pp. 940-948, doi: 10.1109/PIERS-Spring46901.2019.9017851.

36. E. A. Attardo, A. Borsic, G. Vecchi and P. M. Meaney, "Whole-System Electromagnetic Modeling for Microwave Tomography," in IEEE Antennas and Wireless Propagation Letters, vol. 11, pp. 1618-1621, 2012, doi: 10.1109/LAWP.2013.2237745.

37. S. Ahsan, Z. Guo, Z. Miao, I. Sotiriou, M. Koutsoupidou, E. Kallos, G. Palikaras, and P. Kosmas, "Design and Experimental Validation of a Multiple-Frequency Microwave Tomography System Employing the DBIM-TwIST Algorithm," in Sensors, vol. 18, no. 10, p. 3491, Oct. 2018.

38. I. El Kanfoud V. Dolean, C. Migliaccio, J. Lanteri, I. Aliferis, C. Pichot, P. H. Tournier, F. Nataf, F. Hecht, S. Semenov, M. Bonazzoli, F. Rapetti, R. Pasquetti, M. de Buhan, M. Kray, M. Darbas., "Whole-microwave system modeling for brain imaging," in IEEE Conference on Antenna Measurements & Applications, 2015, pp. 1-4, doi: 10.1109/CAMA.2015.7428123.

39. A. M. Qureshi, Z. Mustansar, S. Mustafa, "Finite-element analysis of microwave scattering from a three-dimensional human head model for brain stroke detection," in Royal Society open science, vol. 5(7) 180319. July 2018, doi:10.1098/rsos.180319.

40. T. Singh, B. M. Ninkovic, M. S. Tasic, M. N. Stevanovic, and B. M. Kolundzija, “3-D EM Modeling of Medical Microwave Imaging Scenarios With Controllable Accuracy,” IEEE Transactions on Antennas and Propagation, vol. 71, no. 2, pp. 1640–1653, Feb. 2023, doi: 10.1109/TAP.2022.3209244.

41. WIPL-D software suite (WIPL-D Pro v17 & Pro CAD 2020), WIPL-D d.o.o, Belgrade, 2020.

42. https://www.nevaelectromagnetics.com/

43. Charlick M, M Das J. Anatomy, Head and Neck, Internal Carotid Arteries. [Updated 2021 Jul 26]. In: StatPearls [Internet]. Treasure Island (FL): StatPearls Publishing; 2021 Jan-. Available from: https://www.ncbi.nlm.nih.gov/books/NBK556061/

44. A. T. Mobashsher and A. M. Abbosh, "Three-Dimensional Human Head Phantom With Realistic Electrical Properties and Anatomy," in IEEE Antennas and Wireless Propagation Letters, vol. 13, pp. 1401-1404, 2014.

45. B. Mohammed, A. Abbosh, B. Henin and P. Sharpe, "Head phantom for testing microwave systems for head imaging," 2012 Cairo International Biomedical Engineering Conference (CIBEC), 2012, pp. 191-193

46. M. Haridim, B. Levin, S. Revich, S. Chulski, R. Sauleau and R. Zemach, "Distribution of energy absorption in an inhomogeneous head model at 900 MHz," in IEEE Electromagnetic Compatibility Magazine, vol. 3, no. 4, pp. 43-48, 4th Quarter 2014.

47. Joachimowicz, N.; Duchêne, B.; Conessa, C.; Meyer, O. Anthropomorphic Breast and Head Phantoms for Microwave Imaging. Diagnostics 2018, 8(4) p85.

48. Scapaticci, R.; Donato, L.D.; Catapano, I.; Crocco, L. A feasibility study on Microwave Imaging for Brain Stroke Monitoring. Prog. Electromagn. Res. B 2012, 40, 305–324

49. B.M. Kolundžija, A.R. Djordjević, “Electromagnetic modeling of composite metallic and dielectric structures”, Boston: Artech House, 2002

50. M. N. Stevanovic, R. Scapaticci, and L. Crocco, "Three-dimensional sparse microwave imaging for brain stroke monitoring," 12th European Conference on Antennas and Propagation (EuCAP 2018), 2018.

51. W. C. Chew and Y. M. Wang, "Reconstruction of two-dimensional permittivity distribution using the distorted Born iterative method," in IEEE Transactions on Medical Imaging, vol. 9, no. 2, pp. 218-225, June 1990

52. Ray Simpkin, “Derivation of Lichtenecker’s Logarithmic Mixture Formula From Maxwell’s Equations,” IEEE Transactions on Microwave Theory and Techniques, Vol. 58, No. 3, March 2010.

53. S.O. Nelson, “Measurement and Computation of Powdered Mixture Permittivities,” Proceedings of the 17th IEEE Instrumentation and Measurement Technology Conference.

54. Kimmo Kalervo Kärkkäinen, Ari Henrik Sihvola, and Keijo I. Nikoskinen, “Effective Permittivity of Mixtures: Numerical Validation by the FDTD Method,” IEEE Transactions on Geoscience and Remote Sensing, Vol. 38, No. 3, May 2000 1303.

55. M. M. Kostić and B. M. Kolundžija, "Maximally Orthogonalized Higher Order Bases Over Generalized Wires, Quadrilaterals, and Hexahedra," in IEEE Transactions on Antennas and Propagation, vol. 61, no. 6, pp. 3135-3148, June 2013, doi: 10.1109/TAP.2013.2249036.

56. A. J. Krneta and B. M. Kolundzija, "Evaluation of Potential and Impedance Integrals in Analysis of Axially Symmetric Metallic Structures to Prescribed Accuracy up to Machine Precision," in IEEE Transactions on Antennas and Propagation, vol. 65, no. 5, pp. 2526-2539, May 2017, doi: 10.1109/TAP.2017.2673760.

57. B. M. Kolundzija and M. M. Kostic, "Matrix equilibration in method of moment solutions of surface integral equations," in Radio Science, vol. 49, no. 12, pp. 1265-1276, Dec. 2014, doi: 10.1002/2014RS005536.

58. William J. Schroeder, Jonathan A. Zarge, William E. Lorensen, “Decimation of triangle meshes”, in SIGGRAPH Computer Graphics. 26, vol. 2, July 1992, pp: 65–70, doi.org/10.1145/142920.134010.

59. R. Klein, G. Liebich and W. Strasser, "Mesh reduction with error control," in Proceedings of Seventh Annual IEEE Visualization, 1996, pp. 311-318, doi: 10.1109/VISUAL.1996.568124.

60. K. Hu, D. Yan, D. Bommes, P. Alliez and B. Benes, "Error-Bounded and Feature Preserving Surface Remeshing with Minimal Angle Improvement," in IEEE Transactions on Visualization and Computer Graphics, vol. 23, no. 12, pp. 2560-2573, 1 Dec. 2017, doi: 10.1109/TVCG.2016.2632720.

61. M. Garland, P. S. Heckbert, “Surface Simplification Using Quadric Error Metrics”, in SIGGRAPH: Proceedings of the 24th annual conference on Computer graphics and interactive techniques, August 1997. Pages 209–216, doi.org/10.1145/258734.258849.

62. B. Hamann, “A data reduction scheme for triangulated surfaces,” in Computer Aided Geometric Design, vol. 11, Issue 2, 1994, Pages 197-214, ISSN 0167-8396, doi.org/10.1016/0167-8396(94)90032-9.

63. J. Rossignac, p. Borrel, “Multi-resolution 3D approximations for rendering complex scenes,” in Modeling in Computer Graphics. IFIP Series on Computer Graphics Springer, Berlin, Heidelberg, 1993, doi.org/10.1007/978-3-642-78114-8_29

64. D. Bommes, M. Campen, H. C. Ebke, P. Alliez, L. Kobbelt, “Integer-Grid Maps For Reliable Quad Meshing”, in ACM Trans. Graph., vol. 32, Issue 4, Article 98, pp 1-12, doi.org/10.1145/2461912.2462014.

65. B. M. Kolundzija, "On the locally continuous formulation of surface doublets," in IEEE Transactions on Antennas and Propagation, vol. 46, no. 12, pp. 1879-1883, Dec. 1998, doi: 10.1109/8.743838.

66. Joel Daniels, Cláudio T. Silva, Jason Shepherd, Elaine Cohen, “Quadrilateral mesh simplification”, in ACM SIGGRAPH Asia '08. Association for Computing Machinery, New York, USA, Article 148, pp: 1–9, doi.org/10.1145/1457515.1409101.

67. B. M. Kolundzija, M. M. Kostic, B. L. Mrdakovic and D. S. Sumic, "Comparison of different strategies for conversion of triangular mesh into quadrilateral mesh," in Proceedings of the Fourth European Conference on Antennas and Propagation, 2010, pp. 1-5.

68. M. Tarini, N. Pietroni, P. Cignoni, D. Panozzo, E. Puppo, “Practical quad mesh simplification”, in Computer Graphics Forum Eurographics, 2010, Vol 29, 2, pp 407-418, 2010.

69. B. Kolundzija, V. Petrovic, A. Djordjevic and T. Sarkar, "Efficient method of moment analysis based on imaging and edging," in IEEE Antennas and Propagation Society International Symposium. Transmitting Waves of Progress to the Next Millennium. 2000 Digest. Held in conjunction with: USNC/URSI National Radio Science Meeting (C, 2000, pp. 2298-2301 vol.4, doi: 10.1109/APS.2000.874953.

70. M. Pastorino, A. Randazzo, Microwave Imaging Methods and Applications, in Artech House, 2018.

71. L. Crocco, I. Karanasiou, M. James, R. Conceição, “Emerging Electromagnetic Technologies for Brain Diseases Diagnostics, Monitoring and Therapy,” Springer, Cham, Switzerland, 2018.

72. R. Conceição, J. Mohr, M. O'Halloran, “An Introduction to Microwave Imaging for Breast Cancer Detection”, Switzerland, Springer, 2018.

73. J. D. Shea, B. D. Van Veen and S. C. Hagness, "A TSVD Analysis of Microwave Inverse Scattering for Breast Imaging," in IEEE Transactions on Biomedical Engineering, vol. 59, no. 4, pp. 936-945, April 2012, doi: 10.1109/TBME.2011.2176727.

74. L. Crocco, I. Catapano, L. Di Donato and T. Isernia, "The Linear Sampling Method as a Way to Quantitative Inverse Scattering," in IEEE Transactions on Antennas and Propagation, vol. 60, no. 4, pp. 1844-1853, April 2012, doi: 10.1109/TAP.2012.2186250.

Biography

Tushar Singh was born in Prayagraj, India. He received the B.Tech. degree in Electronics and Communication Engineering from Madan Mohan Malaviya University of Technology, India, in 2012, and the M.Tech. degree in Microwave Engineering from the Indian Institute of Technology (IIT-BHU), Varanasi, India, in 2014.

Following the completion of his master's studies, he joined the School of Electronics Engineering, KIIT University, India, as an Assistant Professor, where he taught courses in Electromagnetic Field Theory, Microwave Devices and Circuits, and Measurement and Instrumentation. During this period, he also served as an Associate Dean in the Training and Placement Department and actively contributed to industry–academia initiatives and engineering laboratory development.

In 2018, he enrolled in the Ph.D. program at the School of Electrical Engineering, University of Belgrade, Serbia. During the same year, he joined WIPL-D d.o.o. as an Early Stage Researcher (ESR) under the European Union Horizon 2020 Marie Skłodowska-Curie EMERALD project. His doctoral research focused on medical microwave imaging, computational electromagnetics, antenna design, anthropomorphic phantom modeling, and accuracy-controlled electromagnetic simulations.

During his doctoral studies, he authored and coauthored several journal articles, conference papers, and book chapters in the areas of microwave imaging and electromagnetic modeling. He was the lead author of the paper *"3-D EM Modeling of Medical Microwave Imaging Scenarios With Controllable Accuracy"* published in IEEE Transactions on Antennas and Propagation, and a co-author of the Springer book chapter *"Numerical Modeling of Complex 3D Electromagnetic Scenarios for Medical Microwave Imaging."*

After completing the EMERALD project, he worked as an Expert Associate for Research and Development at WIPL-D d.o.o., Belgrade, Serbia, where he contributed to the development of advanced electromagnetic simulation software and antenna systems. He subsequently joined Danfoss, where he held positions including Specialist Electronic Simulation and Senior Electronic Simulation Engineer. He is currently employed as a Senior EMC Engineer at Danfoss LLC, Loves Park, Illinois, United States, where his work focuses on electromagnetic compatibility simulation and measurement of high power devices.

List of Publications

Journal Papers

1. T. Singh, B. M. Ninkovic, M. S. Tasic, M. N. Stevanovic and B. M. Kolundzija, "3-D EM Modeling of Medical Microwave Imaging Scenarios With Controllable Accuracy," in IEEE Transactions on Antennas and Propagation, vol. 71, no. 2, pp. 1640-1653, Feb. 2023, doi: 10.1109/TAP.2022.3209244.
2. T. Singh, D. M. Ninkovic, B. M. Kolundzija and M. N. Stevanovic, "Smooth Polynomial Approach for Microwave Imaging in Sparse Processing Framework," in IEEE Access, vol. 10, pp. 120616-120629, 2022, doi: 10.1109/ACCESS.2022.3217221.

Conference Papers

1. T. Singh, M. N. Stevanovic and B. Kolundzija, "Survey and Classification of Antennas for Medical Applications," 2019 13th European Conference on Antennas and Propagation (EuCAP), Krakow, Poland, 2019, pp. 1-5.
2. M. Stevanetic, B. Kolundzija, T. Singh, and M. N. Stevanovic, “Simulation Study of Voxel-Based Head Phantom for Medical Microwave Imaging,” in Proc. 9th International Conference on Electrical, Electronic and Computing Engineering (IcETRAN), Novi Pazar, Serbia, Jun. 2022, pp. AP1.4-1–AP1.4-5.
3. B. Kolundzija, M. N. Stevanovic, M. Stevanetic, B. Ninkovic and T. Singh, "Advanced 3D EM Simulation Environment for Development, Testing, and Usage of Medical Microwave Imaging Devices," 2019 14th International Conference on Advanced Technologies, Systems and Services in Telecommunications (TELSIKS), Nis, Serbia, 2019, pp. 186-189, doi: 10.1109/TELSIKS46999.2019.9002224.
4. T. Singh, M. Stevanetic, M. Stevanovic and B. Kolundzija, "Homogenization of Voxel Models using Material Mixing Formulas," 2020 14th European Conference on Antennas and Propagation (EuCAP), Copenhagen, Denmark, 2020, pp. 1-4, doi: 10.23919/EuCAP48036.2020.9135081.
5. T. Singh et al., "Smart Simplification of Anthropomorphic Head Phantom Aimed for Microwave Imaging," 2021 15th European Conference on Antennas and Propagation (EuCAP), Dusseldorf, Germany, 2021, pp. 1-4, doi: 10.23919/EuCAP51087.2021.9411262.
6. M. N. Stevanovic, T. Singh, B. Ninkovic and B. Kolundzija, "Microwave Sparse Imaging Applied to Stroke Monitoring," 2021 XXXIVth General Assembly and Scientific Symposium of the International Union of Radio Science (URSI GASS), Rome, Italy, 2021, pp. 1-4, doi: 10.23919/URSIGASS51995.2021.9560370.
7. T. Singh, B. Ninkovic, M. Tasic, M. N. Stevanovic and B. Kolundzija, "New Method for Calculation of Average Electric Properties of Reference Head Phantom in Microwave Imaging," 2022 16th European Conference on Antennas and Propagation (EuCAP), Madrid, Spain, 2022, pp. 1-5, doi: 10.23919/EuCAP53622.2022.9769058.
8. M. N. Stevanovic, D. Ninkovic, T. Singh, B. Ninkovic, M. S. Tasic, and B. Kolundzija, “Application of Microwave Imaging for Brain Diagnostics,” in Proc. 9th International Conference on Electrical, Electronic and Computing Engineering (IcETRAN), Novi Pazar, Serbia, Jun. 2022, pp. AP1.1-1–AP1.1-5.

Book Chapters

1. T. Singh, B. Ninkovic, M. Stevanetic, M. Tasic, M. Nikolic Stevanovic, and B. Kolundzija, “Numerical Modeling of Complex 3D Electromagnetic Scenarios for Medical Microwave Imaging,” in Electromagnetic Imaging for a Novel Generation of Medical Devices, F. Vipiana and L. Crocco, Eds. Cham, Switzerland: Springer, 2023, pp. 101–130. doi: 10.1007/978-3-031-28666-7_4.
2. T. Singh, B. Ninkovic, M. Tasic, M. Nikolic Stevanovic, and B. Kolundzija, “Tools and Strategies for 3D EM Modeling and Design of Microwave Imaging Systems for Medical Applications,”in Computational Intelligence and Image Processing in Medical Applications, S. Chen, Ed. Singapore: World Scientific, 2022, ch. 4.4, pp. 297–314, doi: 10.1142/9789811257452_0017.

Изјава о ауторству

Име и презиме аутора Тушар Синг

Број индекса 2018/5033

Изјављујем

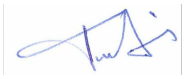
да је докторска дисертација под насловом

КОНТРОЛИСАНО ТРОДИМЕНЗИОНАЛНО ЕЛЕКТРОМАГНЕТСКО МОДЕЛОВАЊЕ СИСТЕМА ЗА ДОБИЈАЊЕ МИКРОТАЛАСНИХ СЛИКА У МЕДИЦИНИ

- резултат сопственог истраживачког рада;
- да дисертација у целини ни у деловима није била предложена за стицање друге дипломе према студијским програмима других високошколских установа;
- да су резултати коректно наведени и
- да нисам кршио/ла ауторска права и користио/ла интелектуалну својину других лица.

Потпис аутора

У Београду, 06/08/2026



Изјава о истоветности штампане и електронске верзије докторског рада

Име и презиме аутора Тушар Синг

Број индекса 5033/2018

Студијски програм Електротехника и електромагнетика

Наслов рада КОНТРОЛИСАНО ТРОДИМЕНЗИОНАЛНО ЕЛЕКТРОМАГНЕТСКО МОДЕЛОВАЊЕ СИСТЕМА ЗА ДОБИЈАЊЕ МИКРОТАЛАСНИХ СЛИКА У МЕДИЦИНИ

Ментор проф. др Марија Николић Стевановић

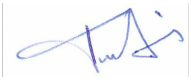
Изјављујем да је штампана верзија мог докторског рада истоветна електронској верзији коју сам предао/ла ради похрањивања у **Дигиталном репозиторијуму Универзитета у Београду.**

Дозвољавам да се објаве моји лични подаци везани за добијање академског назива доктора наука, као што су име и презиме, година и место рођења и датум одбране рада.

Ови лични подаци могу се објавити на мрежним страницама дигиталне библиотеке, у електронском каталогу и у публикацијама Универзитета у Београду.

Потпис аутора

У Београду, 06/08/2026



_____

образац изјаве о коришћењу

Изјава о коришћењу

Овлашћујем Универзитетску библиотеку „Светозар Марковић“ да у Дигитални репозиторијум Универзитета у Београду унесе моју докторску дисертацију под насловом:

КОНТРОЛИСАНО ТРОДИМЕНЗИОНАЛНО ЕЛЕКТРОМАГНЕТСКО МОДЕЛОВАЊЕ СИСТЕМА ЗА ДОБИЈАЊЕ МИКРОТАЛАСНИХ СЛИКА У МЕДИЦИНИ

која је моје ауторско дело.

Дисертацију са свим прилозима предао/ла сам у електронском формату погодном за трајно архивирање.

Моју докторску дисертацију похрањену у Дигиталном репозиторијуму Универзитета у Београду и доступну у отвореном приступу могу да користе сви који поштују одредбе садржане у одабраном типу лиценце Креативне заједнице (Creative Commons) за коју сам се одлучио/ла.

1. Ауторство (CC BY)

2. Ауторство – некомерцијално (CC BY-NC)

3. Ауторство – некомерцијално – без прерада (CC BY-NC-ND)

4. Ауторство – некомерцијално – делити под истим условима (CC BY-NC-SA)

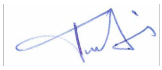
5. Ауторство – без прерада (CC BY-ND)

6. Ауторство – делити под истим условима (CC BY-SA)

(Молимо да заокружите само једну од шест понуђених лиценци.
Кратак опис лиценци је саставни део ове изјаве).

Потпис аутора

У Београду, 06/08/2026



_____